CHALMERS
UNIVERSITY OF TECHNOLOGY

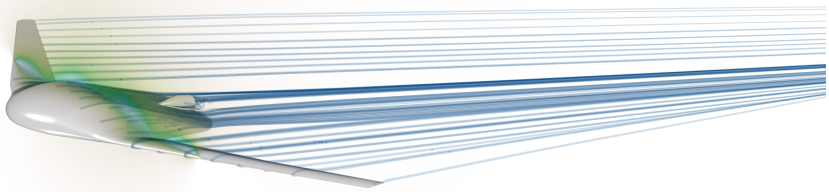

Design and Evaluation of UAV System to Support Naval Search and Rescue

Full design cycle of Blended Wing Body Unmanned Aerial Vehicle, ranging from initial sizing to windtunnel evaluation

Master's thesis in Applied Mechanics

PETTER MILTÉN & CHRISTIAN SVENSSON

DEPARTMENT OF MECHANICS and MARITIME SCIENCES

CHALMERS UNIVERSITY OF TECHNOLOGY
Gothenburg, Sweden 2022
www.chalmers.se

Master's thesis 2022

Design and Evaluation of UAV System to Support Naval Search and Rescue

Full design cycle of Blended Wing Body Unmanned Aerial Vehicle, ranging from initial sizing to windtunnel evaluation

PETTER MILTÉN & CHRISTIAN SVENSSON

CHALMERS
UNIVERSITY OF TECHNOLOGY

Department of Mechanics and Maritime Sciences
Division of Fluid Dynamics
Chalmers University of Technology
Gothenburg, Sweden 2022

Design and Evaluation of UAV System to Support Naval Search and Rescue
Full design cycle of Blended Wing Body Unmanned Aerial Vehicle, ranging from initial sizing to windtunnel evaluation
PETTER MILTÉN & CHRISTIAN SVENSSON

Supervisor: Isak Jonsson & Xin Zhao, M2
Examiner: Carlos Xisto, M2

Master's Thesis 2022
Department of Mechanics and Maritime Sciences
Division of Fluid Dynamics
Chalmers University of Technology
SE-412 96 Gothenburg
Telephone +46 31 772 1000

Cover: Airflow visualization around simplified aircraft.

Typeset in LaTeX
Printed by Chalmers Reproservice
Gothenburg, Sweden 2022

Design and Evaluation of UAV System to Support Naval Search and Rescue
Full design cycle of Blended Wing Body Unmanned Aerial Vehicle, ranging from initial sizing to wind tunnel evaluation
PETTER MILTÉN & CHRISTIAN SVENSSON
Department of Mechanics and Maritime Sciences
Chalmers University of Technology

Abstract

Unmanned Aerial Vehicles (UAVs) have an extensive history of use in the military domain, and its prevalence has surged in recent decades due to further advancements in technology and lowered costs. Presently, UAVs are a widely available technology, and is used by both governments and civilians for various purposes. One application is search and rescue in a naval environment.

Compared to a quadcopter UAV, a fixed-wing UAV will offer greater speed and endurance, which is needed for the given mission. A Blended Wing Body (BWB) is a fixed-wing aircraft type that blends the wing sections and central body into one unified lifting body. The design offers potential increases in lifting capacity and energy efficiency over the conventional tube-and-wing type aircraft designs.

The central aim of this thesis is to investigate the feasibility of a tailless BWB UAV for search and rescue missions at sea, where the Swedish Sea Rescue Society is a potential end-user. If implemented, the BWB concept would offer excellent lifting capability in a neat package, and a tailless design would present the user with an aircraft with minimal parasitic drag.

This work consists of both numerical and experimental methods. Initially, a classical study of initial sizing was performed to set performance requirements. With design targets set, a low-fidelity CFD method was deployed to rapidly iterate aircraft designs and converge on a concept. Next, the design was carried over to a high-fidelity CFD method, where the aircraft was further refined and its performance predicted and evaluated. To guarantee accurate predictions of real life performance, a CFD validation study was conducted in the Chalmers L2 wind tunnel using a full scale model. Finally, a prototype was built and flight-tested.

The final design is a BWB with an operational weight of 2 kg, width of 1.4 m able to carry 1 kg of payload for a mission consisting of 20 min of sprint at 35 m/s followed by 40 min of loiter at 23 m/s. The performance predicted through the high-fidelity CFD method agrees well with experimental data.

Keywords: UAV, BWB, SSRS, CFD, wind tunnel, flow visualization, aerodynamics, validation, STAR-CCM+, XFLR5.

Acknowledgements

This full-year thesis undertaken by the authors would not have been possible without the support and guidance from faculty, project colleagues, friends and family.

The authors would foremost like to thank our examiner Carlos Xisto, as well as our supervisors Isak Jonsson and Xin Zhao for assisting in setting up and securing resources for the project. Without their technical knowledge and endless support the thesis would not be as comprehensive as it ended up being.

We would also like to thank Fredrik Falkman at the Swedish Sea Rescue Society for sharing his knowledge and experience in UAVs for search and rescue applications.
Niclas Robertsson at North Sea Drones for his expertise in model aircraft and for helping us test-fly the prototype.
Martin Larson for excellent opposition of our project and presentation, as well as professional milling of composite tooling.
Edward Hadziavdic for his general knowledge of where everything is stored and how most logistical issues can be solved.

Finally, the prototype manufacturing was made possible with the help of material given by the Chalmers Formula Student project. Our years in the project have shaped us into the engineers we are today, and many of the lessons learned while building race cars were definitely of help during our thesis.

Petter Miltén & Christian Svensson, Gothenburg, June 2022

List of Acronyms

Below is the list of acronyms that have been used throughout this thesis listed in alphabetical order:

UAV	Unmanned Aerial Vehicle
BWB	Blended Wing Body
SSRS	Swedish Sea Rescue Society
HWB	Hybrid Wing Body
CoP	Center of Pressure
CoG	Center of Gravity
CoP	Center of Pressure
SSRS	Swedish Sea Rescue Society
VLM	Vortex Lattice Method
LLT	Lifting Line Theory
CFD	Computational Fluid Dynamics
N-S	Navier-Stokes
AoA	Angle-of-Attack
RANS	Reynolds Averaged Navier-Stokes
FVM	Finite Volume Method
SIMPLE	Semi-Implicit Method for Pressure Linked Equations
SST	Shear-stress Transport
CAD	Computer Aided Design
LE	Leading Edge
TE	Trailing Edge
STEP	Standard for the Exchange of Product Data
CFRP	Carbon-fiber-reinforced Polymer
GSM	Grams per Square Meter
DNS	Direct Numerical Simulation

Nomenclature

Below is the nomenclature of parameters, variables and coefficients that have been used throughout this thesis.

Parameters, variables & coefficients

A	Area
AR	Wing aspect ratio
b	Wing span
c	Chord length
CoM	Center of Mass
CoP	Center of Pressure
C_d	Airfoil drag coefficient
C_D	Wing/aircraft drag coefficient
C_f	Skin friction coefficient
C_l	Airfoil lift coefficient
C_L	Wing/aircraft lift coefficient
C_P	Static pressure coefficient
F_D	Wing/aircraft drag force
F_g	Gravitational force/Weight
F_L	Wing/aircraft lift force
F_s	Wing/aircraft side force
k	Turbulent kinetic energy
m	Mass
Ma	Mach number
M_p	Wing/aircraft pitch moment
M_r	Wing/aircraft roll moment
M_y	Wing/aircraft yaw moment

p	Static pressure
p_0	Total pressure
P_k	Production of turbulent kinetic energy
D_k	Dissipation of turbulent kinetic energy
q	Dynamic pressure
Re	Reynolds number
S	Wing reference area
T	Thrust
T_h	Horizontal thrust component
T_v	Vertical thrust component
v	Velocity
∞	Freestream conditions
α	Angle-of-Attack
ϵ	Turbulent dissipation
Γ	Circulation
γ	Turbulent intermittency
λ	Wing taper ratio
ν	Kinematic viscosity
ω	Specific turbulent dissipation rate
Φ	Velocity potential
ρ	Density
θ	Roll angle

Contents

List of Figures

List of Tables

1

Introduction

The introduction chapter presents the background to why the thesis subject is investigated and concludes in the aim and limitations of the project.

1.1 Background

Today's airspace is occupied by a multitude of aircraft transporting goods and people all over the planet. *Unmanned Aerial Vehicles* (UAV) is a result of research in control systems and autonomous driving. The usage has been restricted to aerobatics and photography but have developed into other areas such as surveillance and delivery, providing great opportunities but also challenges and needs for legislation.

1.1.1 Unmanned Aerial Vehicles

UAVs, often referred to as *drones*, are in general radio controlled, airborne, devices used in a multitude of areas. The availability for both companies and private persons has increased drastically the last couple of years. Most common are quadcopters using four or more propellers to stay airborne and stable.

1.1.2 Blended wing body

A *Blended Wing Body* (BWB), also known as blended body or *Hybrid Wing Body* (HWB), is an aircraft that has no clear dividing line between the wings and fuselage. In contrast to conventional tube-and-wing aircraft that features a cylindrical body with mounted wings onto it. The aim of BWB designs are to utilise the entire structure for lift and payload. The reason so far that no commercial BWB aircrafts are found at airports is that the design complexity is higher, it is harder to scale for different needs and would require compromises to performance in order to offer comfort for passengers [1].

NASA and industry studies suggest that a large commercial BWB aircraft would consume 20 percent less fuel than a comparable conventional aircraft. The BWB would also weigh less, generate less noise and emissions, and cost less to operate than an equally advanced conventional transport aircraft [2].

1.1.3 Similar markets and concepts

Amazon announced that they would launch *Prime Air*, a drone based courier service, in selected cities in 2019. This is yet to be implemented but has met both encouragement and resistance. Zipline is a company who focuses on medicine delivery using a drone aircraft and has so far flown more then 23 million miles [3]. Everdrone is a Swedish company that built a drone for defibrillator delivery, in the 30th of December they successfully delivered the first defibrillator to an accident site [4].

1.2 Aim

The aim of the present project is to fill a gap in the current market and develop a wind tunnel validated BWB UAV with design requirements established in collaboration with the *Swedish Sea Rescue Society* (SSRS) [5]. The work should result in a modular platform for wind tunnel testing that could be used in future projects together with a full validation of the design concept.

1.2.1 Emergency surveillance drone for SSRS

The Swedish Sea Rescue Society is a non-profit organization relying on volunteer work and funded by membership fees and donations. They conduct search and rescue missions at sea in Sweden in both life-threatening and otherwise crucial situations.

Today's normal procedure is to head out towards an emergency with limited information on what the rescue team will face at the accident site. Most alarms provide an approximate location and information of the current status, having more information before leaving port and live updates before arriving to the accident site would be very valuable for the rescue vessel and will help the rescue crew in aiding the ones in need.

This opens for the need to develop a system that can be rapidly deployed to the emergency and provide exact position and visual live feed the accident site. A surveillance drone is developed in the present project to satisfy that need.

1.2.2 SSRS Mission requirements

The UAVs will be stored and launched from a catapult like device positioned along the coast. It will then be aimed at the area around the accident and fly there autonomously. When approaching the accident site, a remote operator will use onboard cameras to mark the accident site, around which the UAV will then loiter and broadcast footage of to the rescue team and/or operator. After the mission is considered complete, either by the rescue crew arrival or depletion of battery, the remote operator will appoint a safe body of water for the UAV to land into and send a beacon signal until picked up by the rescue crew.

The mission from SSRS sets the initial requirements on velocity, endurance, payload,

cargo and stability. The target is to assist in 95% of all search and rescue missions at sea by providing early footage of the accident site and surveying the area for as long as possible, or until rescue personnel reaches the site. Table 1.1 provides the statistics of SSRS missions used to derive the UAV design requirements.

Table 1.1: Statistics of SSRS missions that displays wind speed and distance to accident sites for percentiles of SOS-Alarms. Green mark highlights the 95th percentile where goal to assist is set.

Percentage of SOS-Alarms	Wind speed	Distance
50 %	6 m/s	8 NM
75 %	10 m/s	13 NM
90 %	12 m/s	19 NM
95 %	15 m/s	24 NM
98 %	17 m/s	26 NM
99 %	19 m/s	28 NM

As listed in table 1.1, the surrounding wind speed and flight distance for which the UAV will be designed, that covers 95% of the emergencies, will be 15 m/s and 24 NM. The rescue crew has a departure time on average of 15 minutes and a goal to reach all accidents along the Swedish coastline within 1 hour [6].

The mission requirements for the UAV under development were then set to be able to sprint at 35 m/s for 20 minutes and loiter around the accident site for 40 minutes, and to be stable enough to loiter in harsh wind conditions of about 15 m/s. Table 1.2 shows the estimated times for the UAV to reach the accident site and the estimated loitering time remaining for a mission endurance of 60 minutes.

Table 1.2: *Estimated Time of Arrival* (ETA) for UAV flying at 35 m/s and remaining loitering time until one hour has passed. Yellow marks the percentiles outside of mission requirement due to sprint times over 15 minutes.

Percentage of SOS-Alarms	Distance	UAV ETA @ 35 m/s	Loitering time
50 %	8 NM	7 min	53 min
75 %	13 NM	12 min	48 min
90 %	19 NM	17 min	43 min
95 %	24 NM	21 min	<39 min
98 %	26 NM	23 min	<37 min
99 %	28 NM	25 min	<35 min

About 95% of the SOS-Alarms will be reached withing 20 minutes of sprint and then surveyed, until 1 hour has passed from the time of receiving the alarm. Accidents further away will be reached after the rescue crew has departed from shore, but it is still of great interest to get footage and exact positions of the accident in order to adequately prepare.

1.2.3 Limitations

The main limitations of the present project are due to time constraints. The task is mainly to create a platform for further development, and therefore manufacturing a product that can be equipped and tested is of high value. Resulting in a design process that sometimes compromise optimized results for progress and leaves a functional product with potential for improvement.

2

Theory

The theory chapter is divided into four sections. The first section presents aerodynamic basics and fluid phenomenons. Second comes a section describing basic aircraft design, followed by a section on aircraft flight mechanics and stability. The fourth section presents theory behind numerical simulation models.

2.1 Aerodynamics

A body moving through a fluid medium will experience force acting upon it through a multitude of mechanisms. Some flows are dominated by buoyancy and heat-induced flows, but for vehicles operating in air the dominating forces arise from the vehicle's shape and the fluid's internal resistance to deformation – i.e. the surrounding pressure field and the fluid viscosity.

2.1.1 Subsonic flow

The aircraft will be operating at an airspeed of about $Ma = 0.1$, and will therefore experience subsonic flow over its surface. In this flow regime, density changes are negligible and the air can for this reason be considered incompressible [7]. Contrary to transonic or supersonic flow, where shockwaves occur, the velocity, pressure and temperature fields are continuous. Furthermore, it can occur that the flow behaves the same regardless of flow velocity – so called Reynolds independence, which occurs when the Reynolds number is sufficiently high that the boundary layer becomes fully turbulent. This is famously seen in Moody pipe flow, where for a certain wall roughness the skin friction factor stays constant regardless of flow velocity through the pipe [8].

2.1.2 Pressure field

The pressure field around the aircraft can be split up into a static pressure, a dynamic pressure, and a gravitational head due to elevation. The latter is negligible due to the very small relative change in potential energy along the streamline around the aircraft.

The sum of the static and dynamic pressure is the so called total pressure, p_0,

which in Bernoulli's theorem (neglecting the very small variation in potential energy) remains constant along a streamline in inviscid flow (i.e. no frictional losses):

$$p_0 = p + q = p + \frac{1}{2}\rho v^2 = const. \tag{2.1}$$

where p is the static pressure and q the dynamic pressure.

It is clear from the total pressure relation in Equation 2.1 that the two terms have to exchange energy content in order to conserve the total pressure in e.g. a velocity increase. When the velocity relative to the body is zero, the dynamic pressure term vanishes and the static pressure is equal to the total pressure. This is what is known as stagnation pressure, which is another term for total pressure.

Bernoulli's theorem is as previously mentioned only valid for inviscid flow. In reality the flow around the aircraft body will experience resistance due to viscosity resulting in a total pressure loss. This will happen when air is shearing against any surface and is especially strong in adverse pressure gradients, i.e. a surface curving away from the flow or the suction side of an airfoil. Production of vortices is also a common source of total pressure loss, although their presence in a system can aid in momentum mixing. Being able to reduce total pressure losses is key to an efficient aerodynamic system, as an acceleration of the flow will yield a greater drop in static pressure in the suction side and therefore generate more lift.

2.1.3 Viscous stresses

Due to the fluid viscosity the aircraft will experience stresses tangential to the aircraft surface. If considering the same fluid medium, the main parameters deciding the magnitude of this shearing action will be the body's surface roughness and whether or not the boundary layer is laminar or fully turbulent. Usually the viscous stress is significantly smaller in magnitude than the normal stresses (static pressure) acting on the body, but significant enough to make minimization of this stress a worthwhile endeavour for some applications.

2.1.4 Resultant forces

The normal stresses, from the static pressure field, together with tangential stresses, from the viscous shearing action, will produce a resultant stress vector at every point of the aircraft's surface. The surface integral of this stress vector with respect to the aircraft wetted area will result in a resultant force acting upon the *Center of Pressure* (CoP), which is the point in the three-dimensional space around which the resultant moment is zero.

From this resultant force it is then possible to project the vector onto a vertical and horizontal plane, where this then becomes the total lift and the total drag force vectors respectively. The shear stress contribution to the drag force is known skin friction drag, which together with the shape's stagnation and wake static pressure, also known as form drag, makes up the parasitic drag. The other part of the total

drag force is the induced drag, which is due to the longitudinal component of the force vector created when the body starts producing lift.

2.1.5 Upwash and downwash

A body that is asymmetric with respect to the freestream flow direction will displace the fluid and redirect momentum. An aircraft generating lift does this by redirecting air downwards, which is called downwash. Conversely, some parts of the aircraft might locally generate upwash, and the amount downwash will vary across the aircraft's lift generating elements. But for the airplane to lift its own weight, the net deflection of the air must be directed downward.

2.1.6 Vortex formation

A vortex will form off the airplane body when the presence of a large static pressure gradient, and therefore a velocity gradient, exists around sharp geometry. This happens most notably at the wingtips, where the difference in static pressure due to lift generation causes air to migrate from the pressure side to the suction side of the airfoil. This causes a shearing action in the flow where it will separate off the wingtip edge and cause rotational motion of the air locally.

Due to conservation of angular momentum, the core of the vortex will exhibit a low static pressure which gradually transitions to the ambient static pressure with increasing radius. Conversely the angular velocity will reduce with increasing radius. The low static pressure at the core is exploited in delta-wing aircraft designs, as the wing shape causes an additional vortex to form off the wing leading edge at high angles of attack, and which aids in generating lift in a phenomenon known as vortex lift [9].

When the aircraft is viewed facing the observer, the left-hand wingtip vortex is spinning counter-clockwise, and the right-hand spins clockwise. This will cause a net downwashing of the air trapped between the wingtip vortices. This decreases the lifting performance, as the effective angle of incidence for the incoming air is reduced. It is therefore common to see devices incorporated to wing design to reduce the strength of the vortices and/or move them further away from the wing, which then improves lifting efficiency.

2.1.7 Flow detachment

For viscous flows, when flow detachment occurs on the aircraft body, previous momentum and direction of the airflow is lost. When the flow detachment is large enough, the lifting capability of the geometry can be severely affected, and the phenomenon known as stall is experienced. This primarily occurs when a airfoil is at such an extreme *Angle of Attack* (AoA) that the suction side flow lacks the momentum to overcome the adverse static pressure gradient that exists in the positive chordwise direction. This is then followed by a flow reversal in the boundary layer, and a separation bubble of recirculating air. This kind of separation can also occur

if the incoming air is a low total pressure turbulent wake (for instance a large vortex generated by an aircraft upstream), where both the momentum is low and the incidence of the airflow is not aligned.

To regain lift generation of a stalled airfoil, the primary method is to reduce the AoA of the wing. Due to aerodynamic hysteresis, it is sometimes required to reduce way beyond the stall angle [10].

The primary mechanism in flow detachment is as previously mentioned the lack of momentum in the boundary layer. To delay the onset of stall, it is possible to increase the boundary layer momentum by increasing the momentum diffusion near the surface. This is done by "mixing" in air from the freestream into the boundary layer, usually through vortex generators, which are devices shaped to generate vortices.

2.1.8 Laminar to turbulent transition

The boundary layer along a body's surface moving through the air can either be laminar or turbulent, which is usually identified by what the local Reynold's number is (this will be specific to geometry and freestream properties). Initially, the boundary layer will be laminar, usually all the way up to the point along the chord on the suction side where the suction is at its peak. When the momentum of the air in the boundary layer is no longer able to overcome the positive streamwise pressure gradient (i.e. pressure recovery from suction peak to ambient), the flow can locally detach and induce turbulent fluctations in the boundary layer [11]. With the boundary layer now turbulent, the random velocity flucations cause momentum to be mixed in from the freestream, causing a much "flatter" velocity gradient in the wall-normal direction. The boundary layer close to the wall is now of higher momentum and can overcome the pressure gradient, which will cause the flow to reattach. Between the separation and re-attachment point there will exist a pocket of recirculating air, which reduces lift and generates drag.

There are benefits with both laminar and turbulent boundary layers. The former will be of slower velocity near the wall and therefore cause less skin friction, but is on the other hand not as resilient to adverse pressure gradients. The turbulent boundary layer will exert more skin friction drag due to its higher velocity near the wall, but it is also more resistant to boundary layer separation [12]. It is therefore a design decision whether or not to try to maximize the length of the laminar boundary layer before transition, or to trigger transition immediately (at the leading edge of the wing) to maximise the effect of the turbulent boundary layer.

2.2 Aircraft design

The performance of an aircraft is mainly made up of how efficient the propulsive system is, together with how the aerodynamic surfaces, interact with the surrounding air. Engineering any vehicle for an application is always a game of compromises,

and with the aircraft's ability to freely move in all spatial directions, the number of trade-offs can quickly induce a headache.

2.2.1 Airfoils

The most important component of a fixed-wing aircraft is the wing, and more precisely its shape. The airfoil is the cross-sectional shape of the wing, and is responsible for producing a static pressure variation, which is seen as a high-speed flow (low static pressure) on top of the airfoil, and a slower speed flow (high static pressure) on its underside. This pressure difference in turn creates a lifting force acting on the body.

The airfoil consists of a leading-edge (LE), upper (suction side) and lower (pressure side) surfaces, which then merge the trailing-edge (TE). Furthermore, the airfoil can be described by its chord, which is the distance from LE to TE, its thickness and finally its camber, which is the asymmetry in curvature of the upper and lower surfaces. A symmetrical airfoil will only have a varying thickness from LE to TE and no camber.

From reading textbooks and research papers on the subject of tail-less aircraft, it is clear that a self-stable airfoil geometry is needed [13]. The stability is usually accomplished by implementing a concave aft-section (also known as reflex), which will induce a high-pressure zone. This moves the airfoil's CoP downstream, and has the same effect as a sweptback wing with negative twist at the wing tip. When the airfoil is pitched up, more lift will be generated towards the rear, due to lowering the effective angle of incidence for the "downforce"-producing element, which has the effect of producing a counter moment to the pitch up rotation. The cost of having a reflexed section on an airfoil will be the reduced aft camber, which will create less local aerodynamic load and therefore reduced lift.

2.2.2 Wing geometry

The airfoil profiles plays a major role in the lift and drag generation in an aircraft, as does the shape and size of the wings. A perfectly rectangular wing, seen from above, can be characterized by its chord length, c and span length, b, as well as its projected or wetted area (area of the surface in contact with the air). Many times a virtual reference wing area, S, is used for calculations. This is the horizontal plane projection of a wing extending up to the fuselage center line. To compare different wing layouts, an aspect ratio is introduced, as seen in Equation 2.2.

$$AR = \begin{cases} b/c, \text{ for a rectangular wing} \\ b^2/S, \text{ for a tapered wing} \end{cases} \tag{2.2}$$

A high aspect ratio wing will in general generate lift more efficiently due to smaller wingtip vortex formation, and is why glider aircraft have long wings in the spanwise direction [9]. In other words each portion of the wing generates less lift than a low

aspect ratio wing, but a high aspect ratio wing compensates with having a larger span, and therefore has a smaller pressure difference at the wing tip.

The spanwise lift distribution can also be manipulated to minimize wing tip losses by tapering the wing from root to tip [9]. It is defined by the taper ratio, λ, as seen in Equation 2.3.

$$\lambda = \frac{c_{wingtip}}{c_{wingroot}} \tag{2.3}$$

It is common to see military and commercial aircraft have their wings pointing rearward, i.e. the wing tip is located downstream of the root. This is known as sweep, and is defined as the angle between the wing's mean chord line and the lateral axis. The main effect of a swept wing is the decreased flow speed across the wing perpendicular to the LE, which is due to splitting the incoming velocity vector into a spanwise and a chordwise component. This enables an aircraft traveling at transonic or supersonic speeds to delay the formation of shock waves on the wing (a cause of significant drag), which would form on an unswept wing aircraft traveling at the same speed [9]. The downside to a swept wing is the loss of lifting performance due to the decreased flow speed, but for many applications the overall efficiency is improved by the lack of shock formation.

Swept wings have a tendency to stall early at the wing tips which decreases lift and loss of control if the control surfaces are located far outboard. To prevent this, it is common to locally reduce the angle of attack of the outboard portion of the wing. This is known as wing twist, and can vary linearly across a outboard portion of the wing. It is common for the twist to generate negative lift in cruising conditions, and start generating positive lift when pitching the aircraft up. The result of reducing the AoA is delayed stall at the wing tip, which is worth the decreased outboard lift generation.

Dihedral is the angle formed between the wing and the horizontal plane when the wing is pointing upward. It is used to counter roll, which can occur in strong crosswinds. When flying at a roll angle, the aircraft will experience a side-slip in the direction of the lower wing (the aircraft can be thought of sliding downhill, sideways). This movement increases the flow speed across the lower wing, which in turn generates greater lift and produces a counter roll moment [9].

2.3 Aircraft flight mechanics and stability

Most modern aircraft are traditional tube and wing crafts, they have the advantage of having a large wingspan and a long tail with wings at the rear. The total wing area affect the lift capabilities whereas the spreading of the lifting leads to improved stability. The downside is that the tube is very inefficient at providing lift, making the aircraft less efficient in total. That is where the idea of the Blended Wing Body aircraft was born, trying to make the body produce lift by shaping it like a wing,

or skipping the body and trying to fit all the cargo inside the wings, whatever view you prefer. Either way there has to be downsides or difficulties in designing a BWB compared to a more traditional tube and wing airplane, otherwise others would have done it earlier provided that you could have higher efficiency. In the following subsections will introduce the requirements that have to be fulfilled in order for the aircraft to produce a sustained and stable flight.

2.3.1 Producing lift and thrust: Force equilibrium

The first requirement is to ensure that the aircraft can operate in a neutral state of force equilibrium, this is done by producing enough force to counter the gravitational pull, aerodynamic drag and eventual side wind.

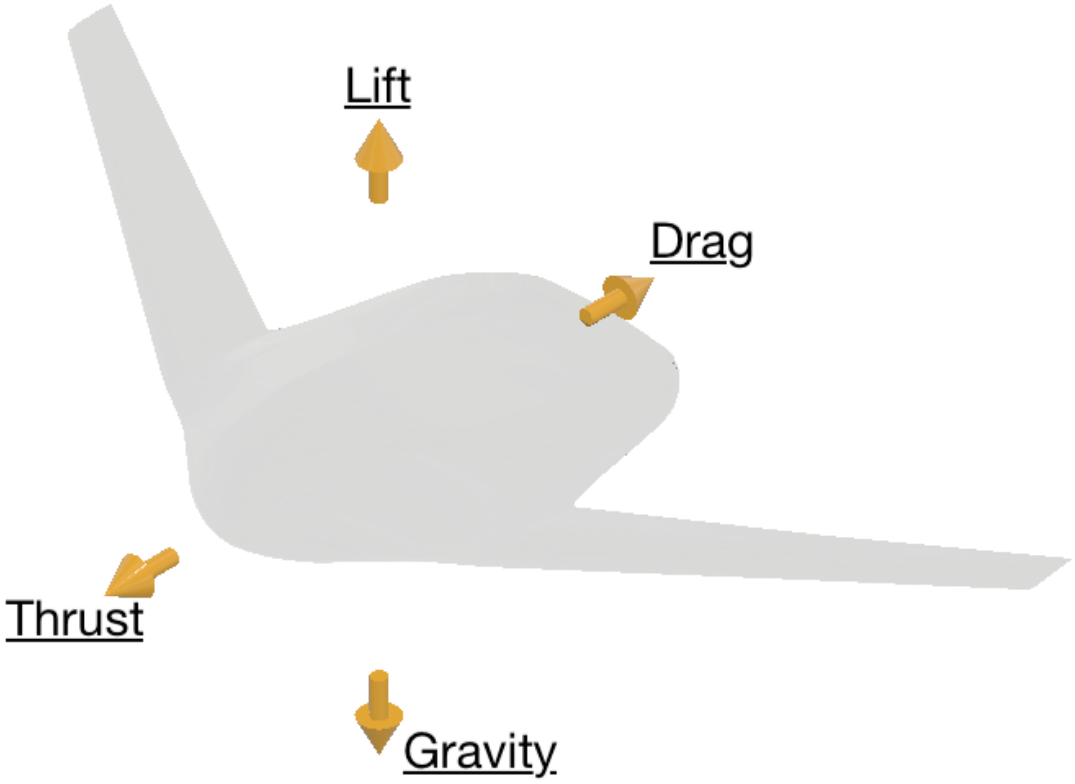

Figure 2.1: Aircraft in force equilibrium

The gravitational pull is constant and only depends on the structural weight, payload weight and eventual fuel or battery weight, resulting in a total aircraft weight,

$$F_g = m \cdot g. \tag{2.4}$$

The lifting force is a function of the aircraft design, velocity through the air, and the aircrafts state of flight determined by the angle of attack (α_a) and angle of control surfaces ($\alpha_{el/er}$). This is summarised into the lifting equation

$$F_L(v) = C_L \cdot S \cdot \rho \cdot v^2, \tag{2.5}$$

where the lift coefficient C_L and reference area S are the only design parameters once velocities are determined. When the flow patterns around the aircraft are similar in a velocity range, the aircraft is Reynolds independent, meaning that the lift and drag coefficients are constant with varying aircraft velocity. Since the mass and thereby gravitational pull is constant and always has to be countered there are different requirements of C_L for different velocities where the lower velocity during take-off requires a higher C_L.

$$\begin{aligned} & F_{L_{Cruise}} = F_{L_{Take-off}} \\ \Rightarrow & C_{L_{Cruise}} \cdot S \cdot \rho \cdot v_{Cruise}^2 = C_{L_{Take-off}} \cdot S \cdot \rho \cdot v_{Take-off}^2 \\ \Rightarrow & \frac{C_{L_{Cruise}}}{C_{L_{Take-off}}} = \frac{v_{Take-off}^2}{v_{Cruise}^2} \end{aligned}$$

Increasing the lift coefficient is primarily done by changing the state of flight and more specifically the angle of attack by pitching the aircraft nose up, to a cap where the aircraft instead transitions into a new state of detached flow and C_L decreases.

The drag force is depending on the same parameters; design, velocity through the air, and state of flight, where increased velocity will lead to higher drag force resisting the aircrafts forwards movement. The drag force is calculated as

$$F_D = C_D \cdot S \cdot \rho \cdot v^2, \tag{2.6}$$

where the drag coefficient C_D and reference area S are the design parameters.

In order to counter the drag force there is need for something producing a force in the direction of flight, in this case a propeller producing forward thrust by accelerating air in the opposite direction of flight.

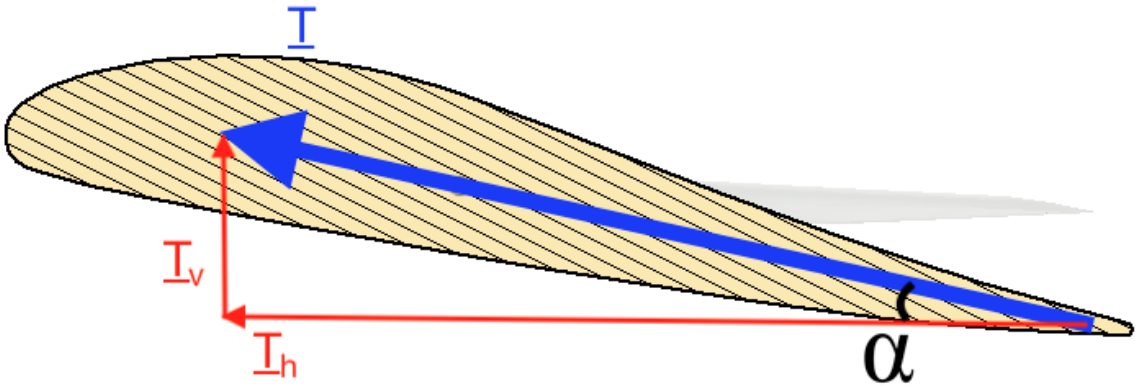

Figure 2.2: Propeller thrust components while at a greater angle of attack

The propeller will also provide a contribution to the vertical force T_v while the aircraft flies at greater attack angles, while also having a slightly lowered horizontal

contribution T_h. This can be disregarded for low angles of attack but might be included as well using the relations in eq. 2.7-2.8.

$$T_h = T \cdot \cos \alpha_a, \tag{2.7}$$
$$T_v = T \cdot \sin \alpha_a. \tag{2.8}$$

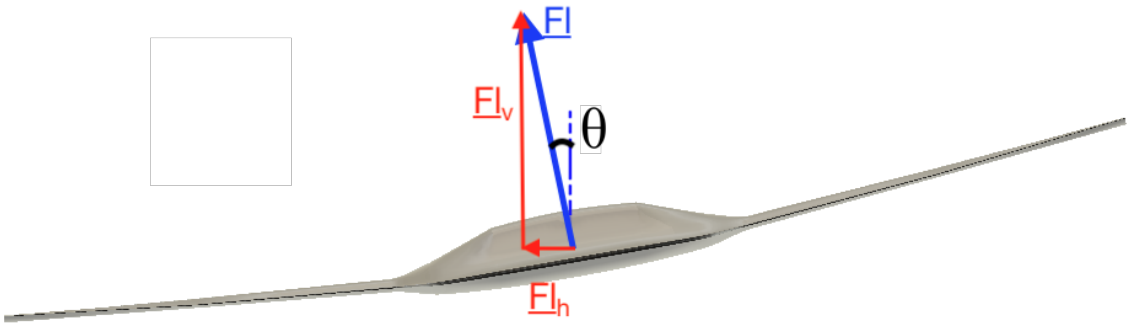

Figure 2.3: Lift components while rolling

Forces produced by side wind F_s can either be countered by yawing or rolling the aircraft, since most small BWBs lack a rudder most choose to roll into the wind and thereby utilize a portion of the lift force as a sideway contribution. Side wind can occur do to weather conditions or while loitering. Either way the total lift produced by the aircraft needs to be increased since the vertical component decreases with roll angle θ.

$$F_{L_h} = F_L \cdot \sin \theta, \tag{2.9}$$
$$F_{L_v} = F_L \cdot \cos \theta. \tag{2.10}$$

Force equilibrium in the vertical-, flight- and side-directions from body and propeller contributions are summarised and result in a number of equations that has to be fulfilled at all static flight modes

$$F_L = \frac{C_L \cdot S \cdot \rho \cdot v^2 + T \cdot \sin \alpha_a}{\cos \theta} \tag{2.11}$$
$$F_D = C_D \cdot S \cdot \rho \cdot v^2 + T \cdot \cos \alpha_a \tag{2.12}$$
$$F_s = F_L \cdot \sin(\theta) \tag{2.13}$$

2.3.2 Trimmed conditions: Moment equilibrium

After ensuring that the aircraft is in force equilibrium the focus shifts to ensuring that it is able to produce sustained flight.

Sustained flight is achieved by having the aircraft in moment equilibrium, one usually denotes movement around the three different axes as pitch, roll and yaw. The moments are a product of the force acting on the aircraft times the distance from

the *Center of Pressure* (CoP) to the *Center of Mass* (CoM) since the assumption is made that the yaw-, roll- and pitch-axes cross the CoM. Yaw equilibrium in straight forwards flying is achieved by having a symmetric aircraft since both the CoP and CoM would end up on the aircraft's symmetry plane. Roll is influenced by propeller torque and has to be countered by either asymmetric design, control surfaces or dual propeller setups.

Trimmed condition is achieved when all net moments acting on the aircraft are zero, which is required in order to fly the aircraft without pitching, rolling or yawing motion. This has to be achieved for every flight mode and is done by moving the center of pressure to coincide with the center of mass. A subgoal is set as having elevons at 0 angle of attack, $\alpha_{el/er} = 0$, for sprint. Since that setup should minimize drag and thereby energy consumption. For other flight modes, such as take-off and loiter, elevon influence are required to achieve a moment equilibrium.

The pitch- (M_p), roll- (M_r) and yaw-moments (M_y) are calculated by knowing the total force and vector from CoP to CoM ($\bar{r}$) as

$$M_p = \bar{x} \cdot p(F \times \bar{r}) \tag{2.14}$$
$$M_r = \bar{y} \cdot p(F \times \bar{r}) \tag{2.15}$$
$$M_y = \bar{z} \cdot p(F \times \bar{r}). \tag{2.16}$$

To simplify, the force vector F is split into components F_L, F_D, F_s and get simplified moment equations

$$M_p = F_L \cdot (CoM_x - CoP_x) + F_D \cdot (CoP_z - CoM_z) \tag{2.17}$$
$$M_r = F_L \cdot (CoP_y - CoM_y) + F_s \cdot (CoM_z - CoP_z) \tag{2.18}$$
$$M_y = F_D \cdot (CoM_y - CoP_y) + F_s \cdot (CoP_x - CoM_x). \tag{2.19}$$

2.3.3 Static stability: Moment derivatives

An aircraft with positive static stability is designed in a way that produces negative feedback on moments without the need of using control surfaces, resulting in a aircraft that wants to return itself to moment equilibrium. The opposite is used by acrobatic or fighter aircraft that wants to be able to do fast maneuvers but has to be forced back to moment equilibrium by control surfaces. Whichever is desired, the most important target is to decide what direction CoP should move in when the flight mode changes.

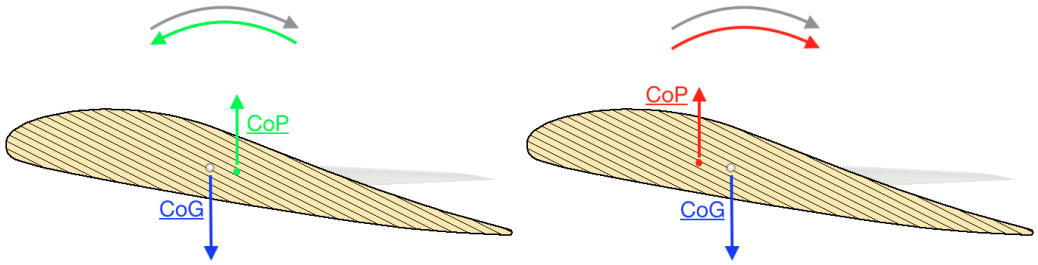

(a) Negative feedback **(b)** Positive feedback

Figure 2.4: Moment as a result on movement of CoP with angle of attack, without influence of elevons

Figure 2.4 above visualises positive and negative pitch feedback. Negative feedback allows for a naturally stable aircraft that in case of a disturbance causing pitch-up, naturally moves CoP backwards to create a pitch-down moment and return the aircraft to its intended flight mode, see Figure 2.5. Since the design in question will have very constant flight conditions a stable aircraft with negative feedback is preferred. Although high negative feedback with more movement of CoP requires larger control surfaces in order to control CoP position to enable flight at other angles of attack.

(a) Aircraft that is either pitch stable, neutral or unstable

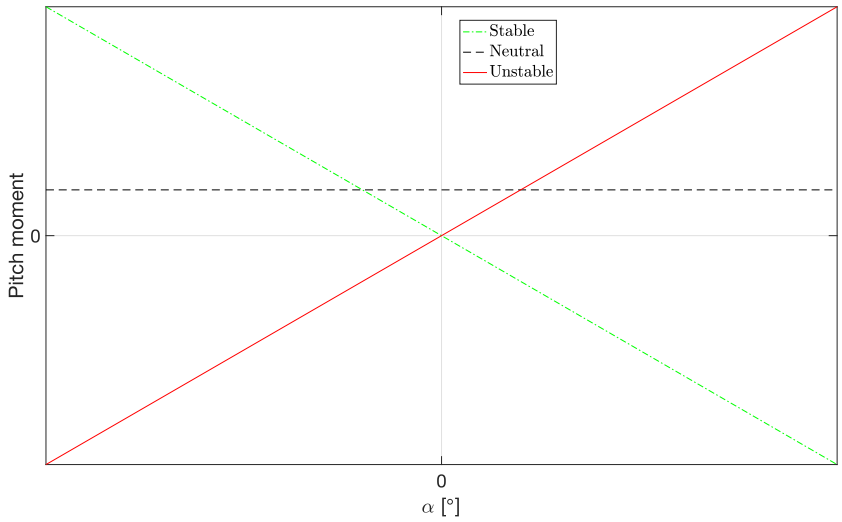

(b) Variation of pitch moment with angle of attack for either stable, neutral or unstable stability

Figure 2.5: Visualisation and graph showing impact of pitch moment derivative on static stability

Similar feedback has to be evaluated in roll and yaw to ensure preferred stability around these axes as well. One common method to ensure roll stability is to add dihedral to the wings of the aircraft, resulting in the wings total force to be angled in towards the body.

(a) Effect from dihedral **(b)** Negative feedback during roll

Figure 2.6: Effect on wing lifting force from implementing dihedral and how it changes roll stability.

Figure 2.6 shows the above mentioned dihedral and how it moves CoP to affects roll

feedback and achieve stability. Yaw stability can be created using winglets or fins to influence the moment around z axis created by drag forces.

When simulating stability one looks at resulting moments at specific aircraft setups and velocity, the result is often simplified to a moment coefficient C_m that depends on aircraft geometry and angle of attack, not on velocity. Either way a negative derivative relates to a negative feedback (naturally stable) and a zero value equals moment equilibrium. The magnitude of the derivative is denoted as *static margin* (SM) and is a measurement of stability.

2.3.4 Creating stability: Control surfaces

Control surfaces are moving surfaces on the aircraft that can be actively controlled to change the aircraft geometry during flight. These are necessary whenever changing from one flight mode to another by moving the CoP to achieved trimmed conditions at the required angle of attack. The aircraft always has to operate in trimmed conditions, meaning that it is in force and moment equilibrium, for all static flight modes. As concluded above, the aircraft has to pitch up to a higher angle of attack in order to fly at a lower velocity. This moves the CoP rearwards in case of a statically stable design, and requires influence from control surfaces to move the CoP back to the CoG in order to reach moment equilibrium at this new operating angle of attack. Similar is true for reaching moment equilibrium at other roll angles where the CoP instead has to be moved sideways by non-symmetric influence from the control surfaces.

Control surfaces will also affect lift and drag whether it is preferred or not. In the case of flying at increased angle of attack and providing pitch moment equilibrium by tilting elevons upwards, a portion of the wing will produce less lift but increased drag. The goal when creating stability is therefore to provide moment with minimized influence on force resultants, which is achieved by having longer leverage arm from the control surface to the center of rotation. This is why tube and wing aircraft utilize small elevons and rudders at the tail to control pitch and yaw, an option tailless BWBs does not have.

2.3.5 Summary of equations for flight and stability

The 9 equations that have to be fulfilled for an aircraft to fly in trimmed conditions and with positive static stability are summarized as follows:

$$F_L = \frac{C_L \cdot S \cdot \rho \cdot v^2 + T \cdot \sin \alpha_a}{\cos \theta} \tag{2.20}$$

$$F_D = C_D \cdot S \cdot \rho \cdot v^2 + T \cdot \cos \alpha_a \tag{2.21}$$

$$F_s = F_L \cdot \sin(\theta) \tag{2.22}$$

$$--- \tag{2.23}$$

$$M_p = F_L \cdot (CoM_x - CoP_x) + F_D \cdot (CoP_z - CoM_z) \tag{2.24}$$

$$M_r = F_L \cdot (CoP_y - CoM_y) + F_s \cdot (CoM_z - CoP_z) \tag{2.25}$$

$$M_y = F_D \cdot (CoM_y - CoP_y) + F_s \cdot (CoP_x - CoM_x) \tag{2.26}$$

$$--- \tag{2.27}$$

$$M'_p < 0 \tag{2.28}$$

$$M'_r < 0 \tag{2.29}$$

$$M'_y < 0 \tag{2.30}$$

$$\tag{2.31}$$

These have to be fulfilled for all flight modes with constant velocity and altitude. The derivatives M'_p, M'_r and M'_y should be negative if static stability is preferred, and their magnitude is normally referred to as *Static Margin* (SM), providing a measure of stability.

2.4 Numerical methods for aerodynamics

There are numerous methods available to predict the performance of an aircraft's aerodynamics with varying levels of complexity and accuracy. When developing a design, it is many times suitable to match the prediction method's complexity and fidelity with the required accuracy needed for a given phase in the development process.

Most methods available, ranging from linear textbook methods to commercial finite-volume codes, have their roots in the *Navier-Stokes* (N-S) equations that are able to fully describe a fluid flow.

2.4.1 Low-fidelity models

The low-fidelity methods described below are derived from potential flow theory, which is a simplification of the Euler equations (inviscid N-S) where the flow is irrotational. In two dimensions, the famous Kutta-Joukowski theorem models an airfoil's lift by:

$$F_L = \rho_\infty v_\infty \times \Gamma \tag{2.32}$$

where Γ is the circulation (vortex strength), which is the line integral of the velocity around the airfoil in the negative direction.

The fundamental idea when using a potential flow model to resolve forces on a geometry for a given flow condition is to model the circulation by an elementary object (e.g. line source, point sink/source, line vortex). The elementary objects can be placed at locations and superimposed to form a velocity potential Φ, which is a scalar field. A simple velocity potential might be a line source to form the freestream velocity, and then a line vortex across the wing to create circulation. Taking the gradient of the velocity potential gives the velocity:

$$\nabla\Phi = V \tag{2.33}$$

Taking the line integral of this velocity in a closed loop around the geometry will then give the circulation Γ.

Continuity is defined as:

$$\nabla^2\Phi = 0 \tag{2.34}$$

which is Laplace's equation. Boundary conditions are then set to prevent the velocity field from penetrating the geometry (solid boundary) and to enforce tangential flow along the geometry (velocity normal to the surface has to be zero).

It is now possible via numerical methods to solve for an unknown velocity potential that satisfies the above conditions. This results in a solution for the circulation, which can be transformed into a force through Equation 2.32. It should be noted that the solution is not unique, and unphysical solution fields have to be disregarded. This is done by enforcing the Kutta-condition, which states that a streamline near the trailing edge cannot cross an imaginary boundary formed from the trailing edge extending downstream.

A more extensive numerical explanation of the low-fidelity models will not be covered here, more detailed information can be found in [14] and [15]. Instead the sections below will focus on the methods' applicability and drawbacks.

2.4.1.1 Lifting Line Thoery (LLT)

An extension of the simple two-dimensional case into three dimensions is the *Lifting Line Theory* (LLT), which models the spanwise lift distribution by considering local circulation. The circulation over the wing is modeled as velocity potential in the form of multiple horseshoe vortices (spanwise vortex line with a trailing vortex line on each end). The trailing vortices creates downwash, which effectively reduces the circulation of the spanwise vortex at the tips. Each loss in circulation in the spanwise direction is modeled as another shed trailing vortex. The circulation has

to be conserved over the wing, and thus the LLT gives a non-uniform spanwise lift distribution, which is one step closer to reality.

2.4.1.2 Vortex Lattice Method (VLM)

VLM is a widely used numerical method and it is an extension of the LLT. The method can be found in aircraft design softwares such as OpenVSP and XFLR5. In VLM the wing geometry is discretized as quadratic panels across the airfoil's mean camber line. Each panel houses a horseshoe vortex and can therefore capture a wing's camber, sweep and dihedral – in contrast to LLT where the wing is seen as a straight line of lift.

Due to VLM's discretization of placing two-dimensional panels on the mean camber line, it is mostly suitable for very thin airfoils where the static pressure distribution on the suction and pressure side is not of interest.

2.4.1.3 3D Panel Method

The 3D Panel method, as implemented in XFLR5, is a further development of the VLM. One of the biggest differences between the methods is the fact that the entire wing geometry is captured by the placement of panels on the top and bottom surfaces, as well as on the wing tips. It is therefore more suitable for thicker airfoils, where the variation in thickness across the chord, in combination with the camber, can have significant effects on the surface static pressure distribution. Another added benefit is the ability to model the fuselage of the aircraft and its effect on the lift generation of the wings. But it should be mentioned that the panels have to connect at the edges and form a surface, and cannot intersect. For a BWB or a flying wing this is usually not a problem as the fuselage is generally made up of airfoils but more importantly is continuous with the wing geometry.

2.4.1.4 Summary of low-fidelity models

The VLM and the 3D panel method are proven methods that can be of great benefit in early design work to rapidly prototype and predict different airfoils and wing geometries. It is numerically cheap and a simulation sweep of many different flying scenarios can be performed in a matter of minutes on a workstation of consumer specifications.

The main drawback, in addition to those mentioned in the section above, is the lack of viscosity modeling. This limits the method's ability to predict flow situations where boundary layer effects play a major role. The methods can therefore not predict wing stall. It is possible to extend VLM and 3D panel codes to include viscous effects, such as viscous drag, by including flat plate skin friction correlations and form factors. Another alternative is to interpolate viscous drag data from two-dimensional codes such as XFOIL. Without the addition of the viscous modeling, the methods described above are only able to predict lift induced drag.

2.4.2 High-fidelity models

The high-fidelity model described below is a method to numerically solve a continuum flow using the discretized form of the Navier-Stokes equations on a computational mesh. Commercial CFD softwares such as Star-CCM+ by Siemens and Fluent by ANSYS are popular all-in-one solutions used in academia and industry, which offers the user a plethora of options in regards to numerical schemes, turbulence models, discretization methods and post-processing.

2.4.2.1 Governing equations

The incompressible fluid flow is predicted by solving the Navier-Stokes equations for a velocity and a pressure field. Equation 2.35 is the continuity equation, which governs the conservation of mass, and Equation 2.36 is the momentum equation, For an incompressible Newtonian fluid with constant viscosity, Navier-Stokes reads,

$$\frac{\partial v_i}{\partial x_i} = 0 \tag{2.35}$$

$$\frac{\partial v_i}{\partial t} + \frac{\partial v_i v_j}{\partial x_j} = -\frac{1}{\rho}\frac{\partial p}{\partial x_i} + \nu \frac{\partial^2 v_i}{\partial x_j \partial x_j} \tag{2.36}$$

where x_i is the spatial position in the i direction, v_i the velocity in the i direction, ρ the density, p the static pressure and ν the kinematic viscosity [16].

The equations are discretized using the *Finite-Volume Method* (FVM) and differencing scheme is then used to compute the convective and diffusive contributions for a given cell from its neighbours. A linear equation system is now formed and is finally solved with an iterative method. Because velocity is found in both the continuity and momentum equation, but the pressure term is only found in the momentum equation, a method for pressure-velocity coupling is needed. This is generally implemented by an algorithm such as SIMPLE, where the velocity field is initially guessed, a mass flux error is calculated, and a pressure correction scheme that is run until the pressure field produces a velocity field which satisfies continuity.

The Navier-Stokes equations in this state can be solved directly through *Direct Numerical Simulation* (DNS), but is astronomically expensive to compute and is currently only of interest within academia for very fundamental flows for many years to come. For engineering applications, simplifications have to be made in order to be able to solve flow fields at acceptable cost-accuracy levels.

2.4.2.2 Turbulence modeling

For most applications when external aerodynamics is of interest, a *Reynolds-Averaged Navier-Stokes* (RANS) solution is an advantageous compromise between solution accuracy and computational cost. This is implemented by introducing a Reynolds decomposition, which splits the velocity into a mean and fluctuating quantity [16]:

$$v_i = \overline{v_i} + v_i' \tag{2.37}$$

By inserting Equation 2.37 into 2.35 and 2.36, the steady-state RANS equations reads,

$$\frac{\partial \overline{v}_i}{\partial x_i} = 0 \tag{2.38}$$

$$\frac{\partial \overline{v}_i \overline{v}_j}{\partial x_j} = -\frac{1}{\rho}\frac{\partial \overline{P}}{\partial x_j} + \frac{\partial}{\partial x_j}\left(\nu \frac{\partial \overline{v}_i}{\partial x_j} - \overline{v_i' v_j'}\right) \tag{2.39}$$

where $-\overline{v_i' v_j'}$ is the unknown Reynolds stress tensor.

The Boussinesq assumption, which introduces an turbulent eddy-viscosity ν_t, assumes that the Reynolds stresses can be modeled as the product of the strain rate tensor and the turbulent viscosity [16]. Equation 2.39 is now written as,

$$\frac{\partial \overline{v}_i \overline{v}_j}{\partial x_j} = -\frac{1}{\rho}\frac{\partial \overline{p}}{\partial x_j} + \frac{\partial}{\partial x_j}\left((\nu + \nu_t)\left(\frac{\partial \overline{v}_i}{x_j} + \frac{\partial \overline{v}_i}{x_i}\right)\right) \tag{2.40}$$

There are various eddy-viscosity models available, but $k-\omega$ SST is regarded as the most robust in accurate prediction of wall-shear stress in flows with highly adverse pressure gradients [17]. The model uses the $k-\omega$ model near walls which makes it possible to resolve the entire boundary layer, and switches to $k-\epsilon$ in the upper portion of the boundary layer as well as in the bulk flow where it is less sensitive to inlet turbulence and is good at predicting free-shear flows. In addition to this, a wall-shear stress limiter is implemented in order to not overpredict flow attachment, which is a problem in the $k-\epsilon$ model. The model calculates the turbulent viscosity as $\nu_t = k/\omega$, where k is the turbulent kinetic energy and ω the specific dissipation rate. These two turbulent quantities are calculated by solving their respective transport equations. The model contains various coefficients and therefore requires calibration against experimental data. Commercial CFD codes usually have their coefficients tuned to fit a wide range of flow phenomena.

If boundary layer transition is of interest in the simulation, as it is in many cases for wings, and if the Reynolds regime is expected to be in the transitional range – a turbulent transition model is needed. The $k-\omega$ SST model can be extended to include a model for predicting where transition will occur and subsequently suppress production of turbulence where necessary. In the γ-family of transition models, a concept of turbulent intermittency, γ is introduced. γ is the percentage of time a turbulent velocity fluctuation is present in the boundary layer. $\gamma = 0$ is a laminar boundary layer, $0 < \gamma < 1$ is a transitional zone and $\gamma = 1$ is a fully turbulent boundary layer.

The turbulent suppression is implemented by changing the turbulent production (P_k) and dissipation (D_k) terms, in the transport equation for the turbulent kinetic energy, k. P_k is multiplied with γ, which results in zero production when the boundary layer is laminar [18]. The dissipation term is modified with a limiter function to guarantee that dissipation is still present in the case when no turbulence is produced, which ensures damping of turbulent fluctuations outside of the boundary layer. In the transport equation for the specific dissipation rate (ω), the function blending between $k-\omega$ and $k-\epsilon$ is modified to prevent the latter from being enabled in a laminar boundary layer.

The $\gamma - Re_{\theta t}$ model solves transport equations for the intermittency and the momentum thickness Reynolds number, $Re_{\theta t}$, where the latter is used to compare the local flow against experimental correlations of transition onset. In comparison, the γ transition model is a one-equation model where intermittency is the only transport equation solved, and instead computes the momentum thickness Reynolds number using algebraic relations with local flow variables [19]. The more simple γ model is cheaper computationally, and requires minimum user input. The $Re_{\theta t}$ model requires the user to provide a function for identifying the boundary layer, but is on the other hand able to predict flow phenomena such as cross-flow instabilities in the boundary layer.

2.4.2.3 Summary of high-fidelity models

The use of RANS CFD models in external aerodynamics is a widely accepted practice in industry, and offers low computational costs and accurate flow prediction in many cases. It is always recommended to validate the CFD setup with experiments if possible, and many papers on best-practices are available to save the user time in setting up the CFD study.

3

Method

The method chapter will present the different steps of the design, validation and manufacturing process.

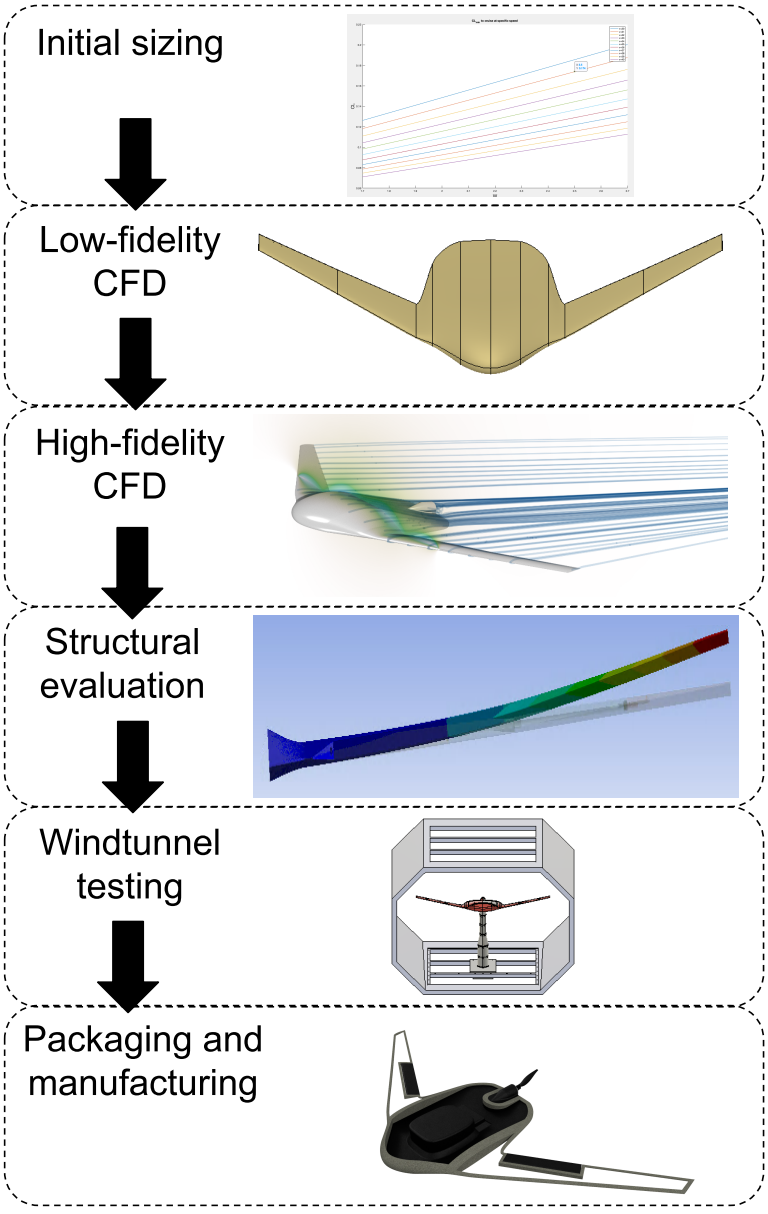

3.1 Initial sizing

First step of design is to define mission requirements and set design parameters. Table 3.1 lists the provided missions requirements and design targets.

Table 3.1: List of mission requirements and design targets governing the design process

Mission requirements		Design targets	
Sprint velocity	35 m/s	Wingspan	<1.5 m
Sprint duration	20 min	BWB	
Loiter duration	40 min	Tailless	
Take-off velocity	15 m/s	Stable after cargo drop	
Cargo weight	1 kg	Land in water	
Electric system weight	1 kg	Static stability	

3.1.1 Mission requirements and design targets

The main mission requirements given by SSRS, section 1.2.2, states that the aircraft should be launched from a catapult at 10 m/s, sprint for 20 minutes at 35 m/s and then loiter for 40 minutes while providing live feed of the accident to a rescue crew.

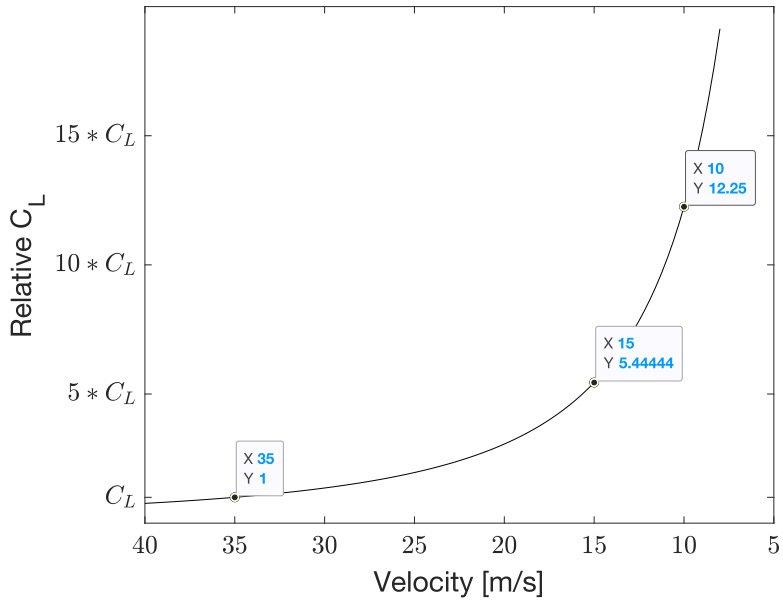

Figure 3.1: C_L over velocity for constant lifting force, relative to $C_L = 1$ at sprint velocity of 35 m/s

Figure 3.1 shows demand on C_L with varying velocity to result in a constant lifting force, relative to $C_L = 1$ at sprint conditions of 35 m/s. No active high-lifting devices will be installed and the only way of increasing C_L during flight is to increase the

angle of attack. The conclusion was that a launch velocity of 10 m/s would require a C_L that is more then 12 times higher at take-off then at sprint.

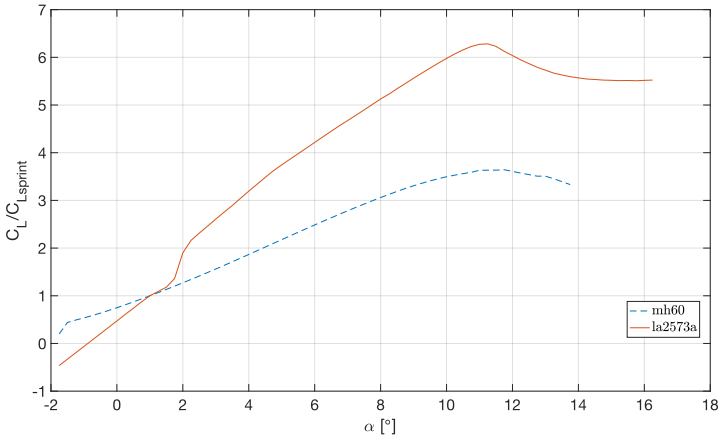

Figure 3.2: C_L variation, normalized against C_L at sprint, over velocity. Displayed for two airfoils used to construct the aircraft.

An angle of attack around 1 deg is estimated for sprinting conditions and figure 3.2 shows the variation of $C_L/C_{L_{sprint}}$ with angle of attack for two airfoils used to construct the aircraft [20]-[21]. The maximum C_L occurs around an angle of attack of 11 deg and is far below 12 times C_L at sprint. Therefore the demand for take-off velocity was reconsidered and 15 m/s was estimated to be a more tolerable launch velocity, requiring a C_L of 5.4 times higher then C_L at sprint according to figure 3.1. Angle of attack for take-off was estimated at 10 deg to have some margin before stalling.

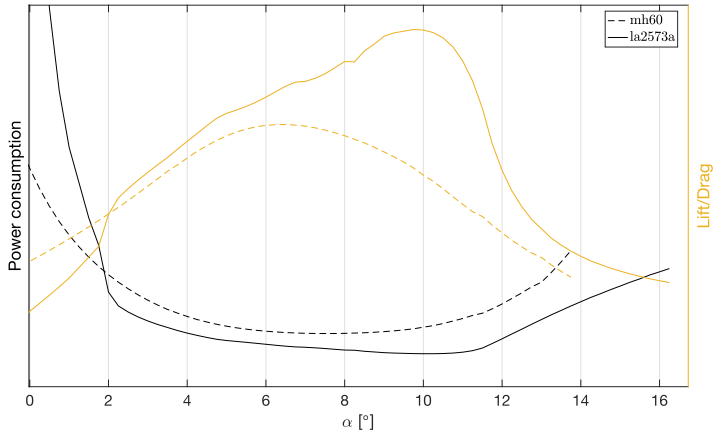

Figure 3.3: Power consumption and Lift/Drag variation with angle of attack. Displayed for two airfoils used to construct the aircraft.

Figure 3.3 shows the variation of power consumption and lift/drag with angle of attack. The power consumption is calculated by using varying velocity that would

ensure 30 N of lifting force at all angles of attack. The end goal is to minimize the total energy required to complete the mission, which should be done by compromising proportionally for sprint and loiter since they are done for different periods of time and at different velocities. The goal is then to minimize

$$F_{D_sprint} \cdot v_sprint \cdot t_sprint + F_{D_loiter} \cdot v_loiter \cdot t_loiter, \tag{3.1}$$

$$or \tag{3.2}$$

$$C_{D_sprint} \cdot v_sprint^3 \cdot t_sprint + C_{D_loiter} \cdot v_loiter^3 \cdot t_loiter. \tag{3.3}$$

According to figure 3.3 this should be done by operating around an angle of attack of 11 deg, where C_L is high and therefore allows for a low velocity. But the restriction of sprinting at 35 m/s and launching at 15 m/s requires a greater range of operating angles of attack, due to the previously presented range in C_L from sprint to take-off.

The conclusion is then that the aircraft has to operate at high energy consumption during sprint, and the solutions would be to either increase the launch velocity to allow for downsizing the aircraft and sprinting at a higher angle of attack, allowing a higher lift/drag. Or to reduce sprinting velocity, which is unacceptable for the main mission of reaching the accident site early to provide camera footage to the rescue crew.

3.1.2 Payload and packaging

The payload mass is estimated to be 3±.5 kg including cargo of 1 kg. The cargo bay should be big enough to fit a package containing a heart defibrillator including necessities. Which sets a limitation in high and width of the main body. In order to maintain CoG position and thereby stability after eventual delivery of the cargo sets a requirement of the CoG of the cargo and rest of the aircraft to coincide to the same position.

3.1.3 Design parameters

A design target to design a tailless, BWB that achieves static stability is considered a challenge which should have the highest potential for efficiency but is notoriously hard to accomplish. The target is set to encourage evaluation of the concept and determine if it is a feasible design for accomplishing the mission.

Table 3.2: List of design parameters for the aircraft's different flight modes
** Parameters for loiter are estimated and will be revised to minimize consumption*

Flight modes	Velocity [m/s]	Angle of attack [°]	Relative $C_L \cdot A$
Sprint	35	1	1
Loiter *	24	4	2.5
Take-off	15	10	5.4

Table 3.2 lists the design parameters for the aircraft different flight modes. Sprint

and take-off are set while loiter is estimated and will be revised once more data is available and a decision can be made to minimize loitering energy consumption.

3.2 Low-fidelity CFD

Through the use of the low-fidelity method, a number of design concepts were evaluated. The results presented below are the final specifications of the aircraft before the design work was carried over to the High-fidelity method.

XFLR5 was chosen as the potential flow software, as it includes 2D airfoil analysis tools from XFOIL, 3D panel method simulation capability as well as a parametric aircraft design environment. A drawback compared to OpenVSP is the lack of blending capability between wing sections in the parametric design environment, but it was decided that the potential decrease in aircraft performance would be minimal. The primary reason for choosing XFLR5 over OpenVSP was the relative ease of getting the panel method to converge to a result for a given aircraft design.

The sections below will briefly describe the result of the iterative design process in XFLR5.

3.2.1 CAD generation

The work in XFLR5 for this aircraft was straight forward, as the whole airplane can be treated as a wing. The geometry was first created by importing the selected airfoils into the airfoil designer module, where the coordinates of the splines can be modified if desired. Modifications to maximum thickness and camber are also changes that can be easily implemented.

With the airfoils now available, it is possible to generate wing sections in the parametric CAD module. The aircraft is created by entering the following parameters for a given wing section, as presented in Table 3.3.

Table 3.3: Example of how a wing is parametrically modeled in XFLR5.

Wing section (n)	y pos.	Chord length	x pos.	Dihedral	Twist	Airfoil
n						
n+1						

Each wing section will also require a panel discretization, as described in Section 2.4.1.3. The number of panels in the span wise and chord wise directions can be changed, as well as their distribution function (sine or cosine) in both directions. The distribution helps with acquiring good mesh resolution in transitions between wing sections, where large numerical gradients might occur.

3.2.2 Solver settings

With a aircraft geometry defined, it is then possible to perform CFD simulations using the methods described in Section 2.4.1.

For a typical sweep of different AoA at a constant speed, the following settings were used:

- Polar type: Type 1 (fixed speed, $v = 35m/s$)
- Analysis type: 3D panels, viscous drag option enabled
- Miscellaneous settings: Plane inertia (for custom CoG), Wing planform (for reference values), Ground effect disabled (for freestream conditions)

The time for the simulation sweep will vary depending on analysis method and discretization, but is on the order of 3-10 minutes, and therefore has a very short turnaround.

3.2.3 Selected airfoils

Two airfoils were selected for this project, and was a decision inspired by other BWB research projects such as [22].

The selected airfoils were:

- MH60, by Martin Hepperle [23]
- LA2573A, by Roberth H. Liebeck [21]

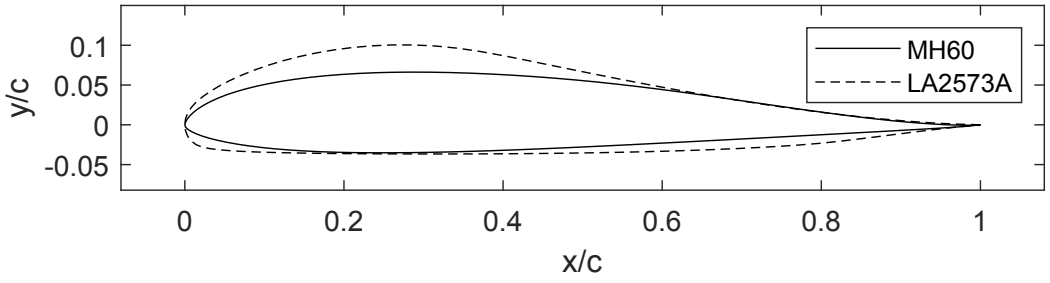

Figure 3.4: A comparison of the selected airfoils.

The MH60 (see figure 3.5) is a low pitch moment coefficient airfoil and is suitable for flying wings and other tail-less aircraft, which is achieved with a slight reflexed aft section. It has a relatively high lift coefficient for its moderate camber. The maximum thickness is around 10%, which makes it hard to use as the airfoil for the body due to packaging, but is suitable as the profile for the wing sections.

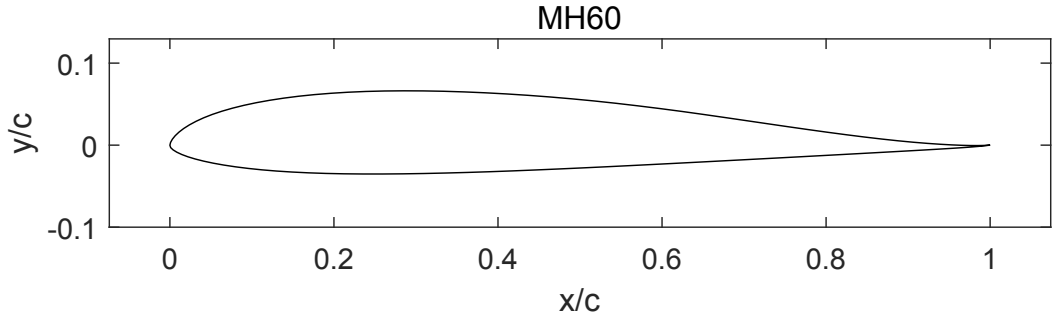

Figure 3.5: The MH60 airfoil.

The LA2573A airfoil (see figure 3.6) is a reflexed airfoil also with a moderately high lift coefficient. Compared to the MH60 airfoil, the lift is slightly higher but with an almost zero pitch moment coefficient. Additionally, the blunt leading edge makes it more resilient to leading edge separation at higher angles of incidence. Most importantly, the maximum thickness is roughly 14%, which makes it suitable as the airfoil for the aircraft body.

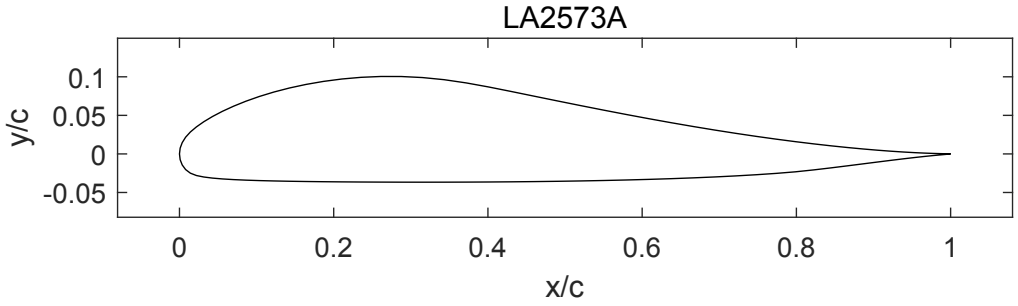

Figure 3.6: The LA2573A airfoil.

3.2.4 Preliminary aircraft design

As presented in 3.1, the objective was to get a design that could achieve a zero pitch moment at a very low AoA. This is due to the requirement of minimizing drag in the sprint condition, where speed is at its max and the use of control surfaces to produce a counter pitch moment would also add to the drag.

The wing specifications are listed below in Table 3.4.

Span	1.400 m
Body Airfoil	LA2573A
Body Mean Chord	0.562 m
Wing Airfoil	MH60
Wing Mean Chord	0.127 m
Projected Planform Area	0.322 m^2
Average Wing Sweep	30 °
Maximum twist	-2 °
Wing dihedral	5 °

Table 3.4: Aircraft specifications for preliminary design.

The wings are responsible for roughly half of the total lift generated, with the rest generated in the much thicker body. The thickness is due to the body having to contain the onboard systems and the payload, with the latter having its CoG right at the airfoil's maximum thickness location. The swept wing is used to position the wing twist rearwards, where downforce is needed for pitch stability. Figure 3.7 shows the aircraft's wing planform.

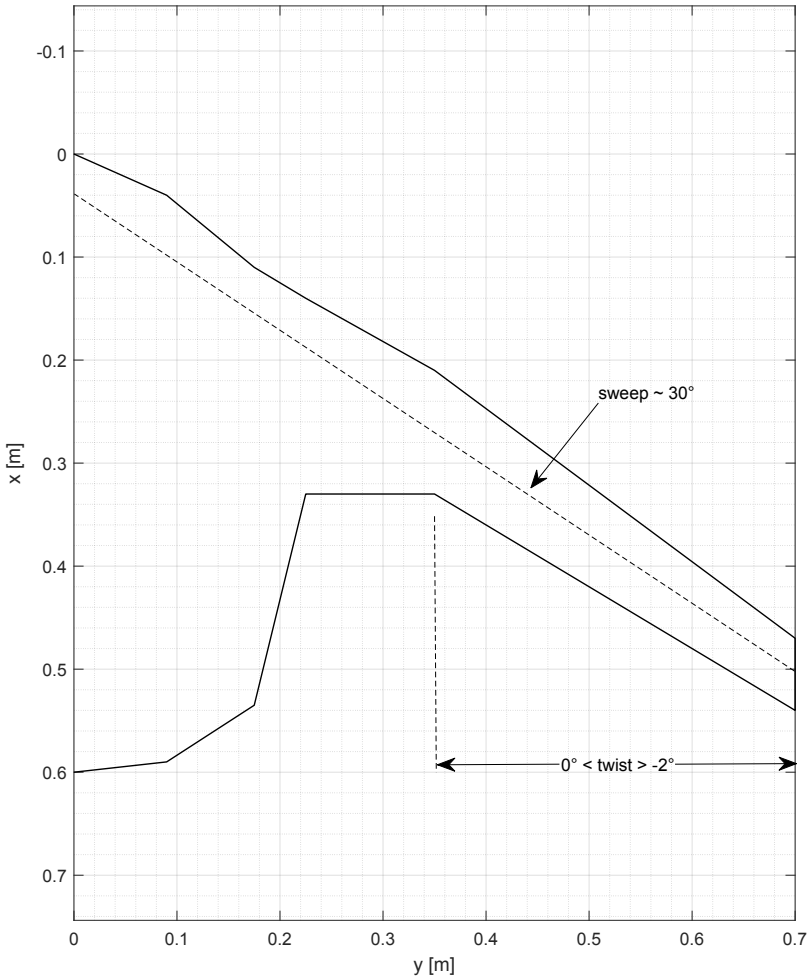

Figure 3.7: Planform of the aircraft. Wing twist (washout) varies linearly in the marked area.

The aircraft geometry as seen in XFLR5 is provided in Figure 3.8. It should be noted that it is currently not possible to blend the wing sections smoothly to have a leading and trailing edge with a continuous curvature. While in reality sharp transitions might induce small local flow separations or trigger transition, it was determined not to affect the low-fidelity design work as the real effects would be small in comparison with e.g. total lift of the planform. As XFLR5 is a potential flow code, none of these flow phenomena will be captured, and blending the wing sections was therefore left as an exercise for the high-fidelity design work.

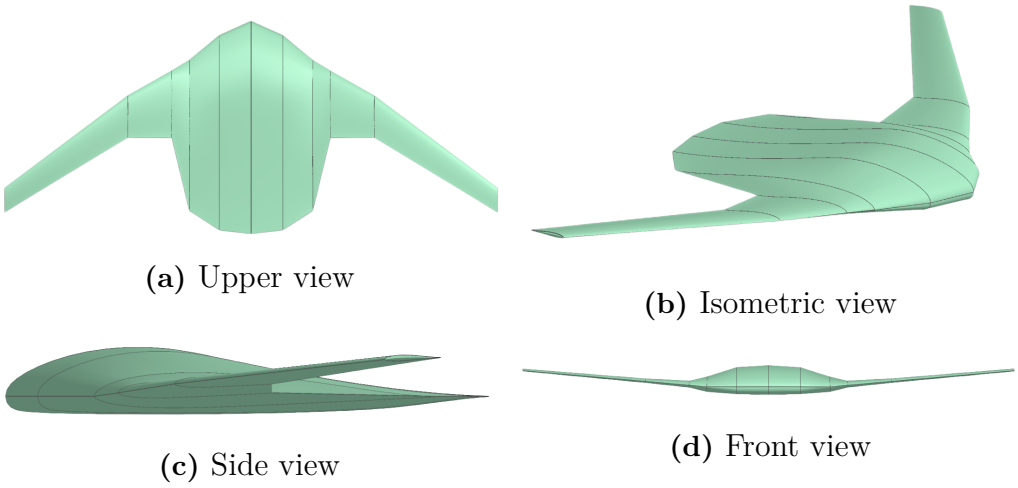

(a) Upper view

(b) Isometric view

(c) Side view

(d) Front view

Figure 3.8: Aircraft geometry viewed in XFLR5.

3.2.5 Preliminary aircraft performance

The design finds its trimmed condition in pitch at around $\alpha = 2.6°$, see Figure 3.9.It is also seen that the pitch moment coefficient has a negative slope, which gives the aircraft a negative feedback when subjected to a rotation in pitch.

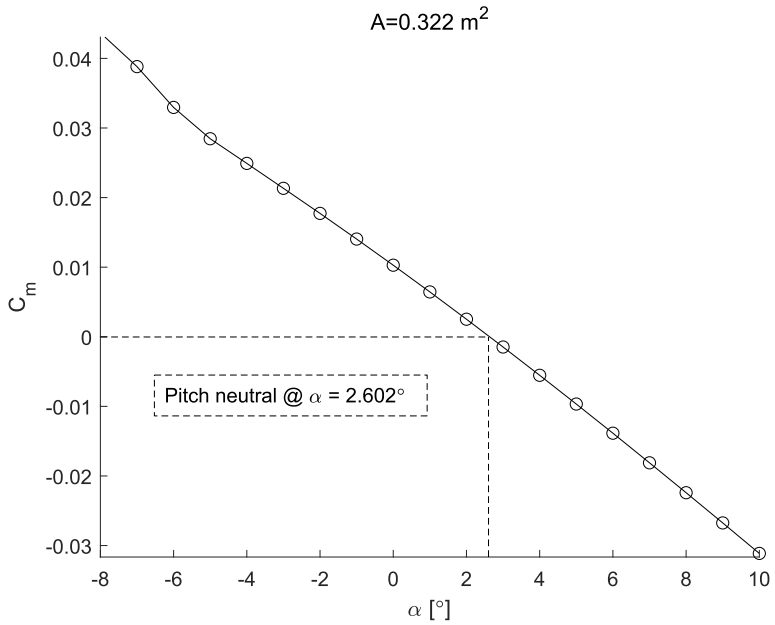

Figure 3.9: Pitch moment curve

At this AoA the lift produced equals a $C_L A = 0.063$, which is more than the target of 0.04, see Figure 3.10. The drag performance of the aircraft is seen in Figure 3.11.

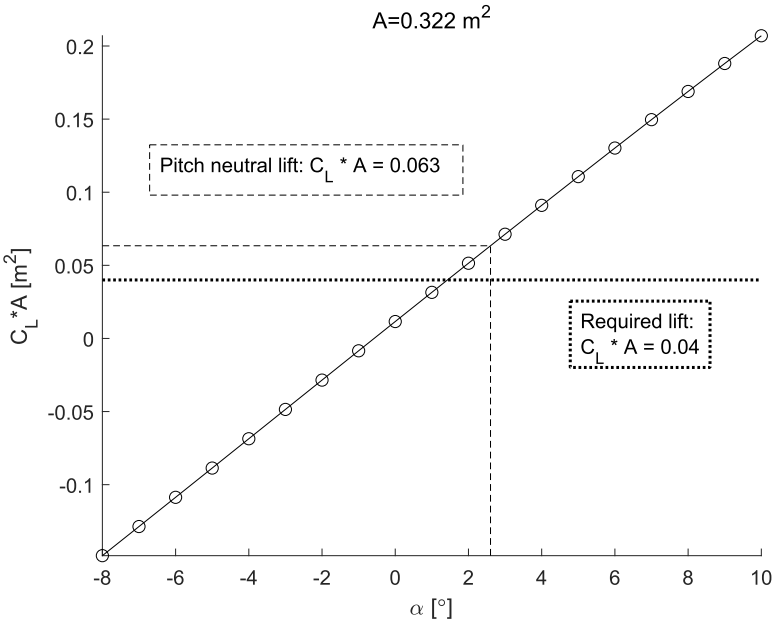

Figure 3.10: Lift curve

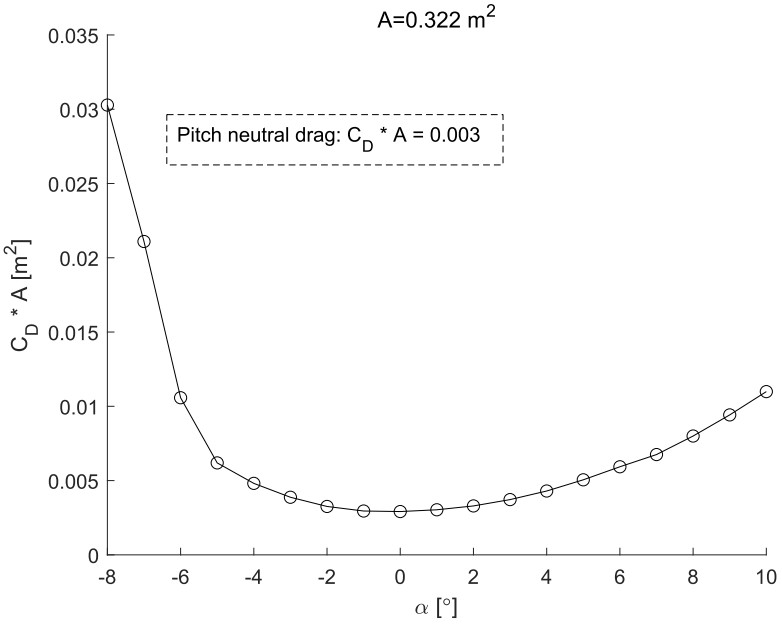

Figure 3.11: Drag curve

3.2.6 Summary of Low-fidelity CFD work

The iteration process performed in XFLR5 using the 3D panel method yielded an aircraft design capable of performing according to the set requirements. It was decided at this point that the the overall planform design was satisfactory, both in terms of aerodynamic performance and packaging requirements.

At this stage of the project, a handful of simulations have already been performed using the high-fidelity CFD method in Star-CCM+. While the simulation setup was still under development in terms of solver and mesh settings, the results showed an under-prediction of lift by XFLR5 at lower AoA, while a over-prediction was seen above 8°, see Figure 3.12

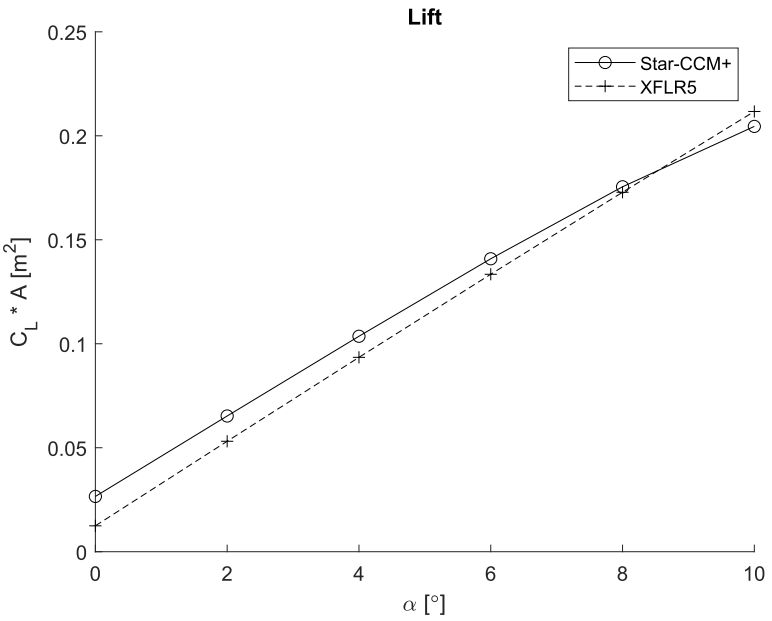

Figure 3.12: Lift curve comparison between low and high-fidelity CFD

A large, more pressing discrepancy was found in the CoP_x location, see Figure 3.13. This is more of a problem than the difference in lift curves, as most of the design changes are done to get the pitch moment behaviour correct. It was therefore decided to from this point onward to solely use the high-fidelity CFD to evaluate coming design iterations, as it is a more accurate model.

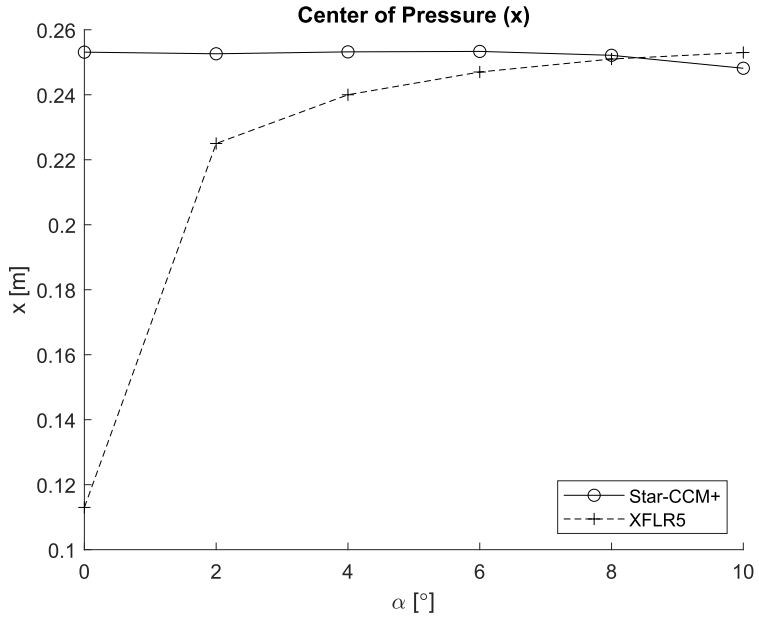

Figure 3.13: Center of Pressure curve comparison between low and high-fidelity CFD

3.3 High-fidelity CFD

The method described here covers the work performed in the CFD software Star-CCM+, which was used for carrying out the final design iterations as well as the mapping of the expected flight performance. In addition to this, a setup mimicking the conditions in Chalmers L2 wind tunnel was created for the CFD validation study.

The aircraft design was already at a mature stage in terms of wing design and overall planform specifications, but required minor changes to the wing section to get the aircraft trimmed in pitch at the desired AoA of 1°.

3.3.1 CAD generation

The aircraft geometry was parametrically generated in OpenVSP [24] in similar fashion to what was described in the low-fidelity method. Extra steps were taken to enforce continuity in the LE and TE curvature using the software's blending functionality. In addition, the wing sections' trailing edge was modified to ensure low skewness of cells in close proximity to the TE in the volume mesh in Star-CCM+, which if not done is bound to cause numerical instabilities or unacceptable computational costs by having to use extremely small cells relative to the rest of the near-wall mesh. This was achieved by cutting off a small portion of the trailing edge with a semi-circle.

OpenVSP is able to export the geometry in the STEP file format, which is read by most CFD pre-processors. It was noticed that sub-surfaces of the wing sections

often ended up being stitched together, which in itself is not a problem for most CFD packages, but meant that many dozen surfaces instead of a single one for e.g. the outer wing portion's suction side would appear. This adds extra work when applying force reports or custom mesh settings in the pre-processing stage. To combat this, the geometry was brought into CATIA V5 for stitching. The end result was an upper and a lower side for the body, elevons and wing sections, respectively.

An aerodynamic cover for the electrical motor was modeled separately in CAD and was then imported into Star-CCM+ with the rest of the aircraft.

3.3.2 CFD setup

The high-fidelity simulations performed had to be efficient in their use due to the nature of the project being a complete development and prototyping cycle with little time for in-depth numerical studies. This implied a robust, relatively computationally inexpensive model with good aerodynamic force prediction. The following sections will describe the CFD setup in more detail, and is based on industry best practices [25].

3.3.2.1 Numerical models

The physics chosen for the simulations was a steady-state, incompressible RANS model with a segregated pressure-velocity solver. The turbulence model chosen was the $k - \omega$ SST, which is the industry favorite out of the eddy-viscosity models due to its superior performance in predicting shear-stress in external flows with highly adverse pressure gradients. This enables more accurate prediction of much load the boundary layer is under i.e. its thickening and separation behaviour, which in turn will give a more precise picture of the surface pressure-recovery and viscous drag.

As the aircraft is to operate at a great range of speeds, the flow cannot be assumed to be independent of Reynolds number regime. Therefore a transition model is needed to predict and suppress the production of turbulence where laminar, or transitional flow is to be expected. The model chosen was the one-equation γ model as it is designed to fit a a great range of flow conditions, which also made implementation simple. Being able to predict laminar separation bubbles and not assuming fully turbulent boundary layer along its full length will help in more accurate lift and drag predictions.

Finally, Star-CCM+'s adaptive mesh refinement model was enabled. More on this in Section 3.3.2.4.

A summary of the models enabled in Star-CCM+ is seen below in Table 3.5.

Table 3.5: Enabled physics models in Star-CCM+

Reynolds-Averaged Navier-Stokes
Steady
Constant Density
Segregated Flow
Gas
Three Dimensional
Turbulent
$k-\omega$ SST Turbulence
Gamma Transition
Adaptive Mesh

3.3.2.2 Computational domain

Two different computational domains were needed for this project – one simulating real-life freestream conditions and one for comparing the CFD model's predictive performance with experimental results.

The real-life freestream domain, reffered as *"No blockage"* in this text, is a rectangular cuboid with a significantly larger cross-sectional area compared to the aircraft's frontal area to interfere minimally with pressure gradients, and that is long enough for flow total pressure losses to diffuse. The domain sizes are found below in Table 3.6, and are described in the distance from the aircraft to each face of the domain. The distances in the xy-plane are written in maximum body chord length, while the vertical distances are provided in maximum body thickness. A picture of the domain can be seen in Figure 3.14.

Table 3.6: Distances from the aircraft to the domain faces.

Inlet	Outlet	Upper/lower	Left/right
5 c_{max}	20 c_{max}	25 t_{max}	5 c_{max}

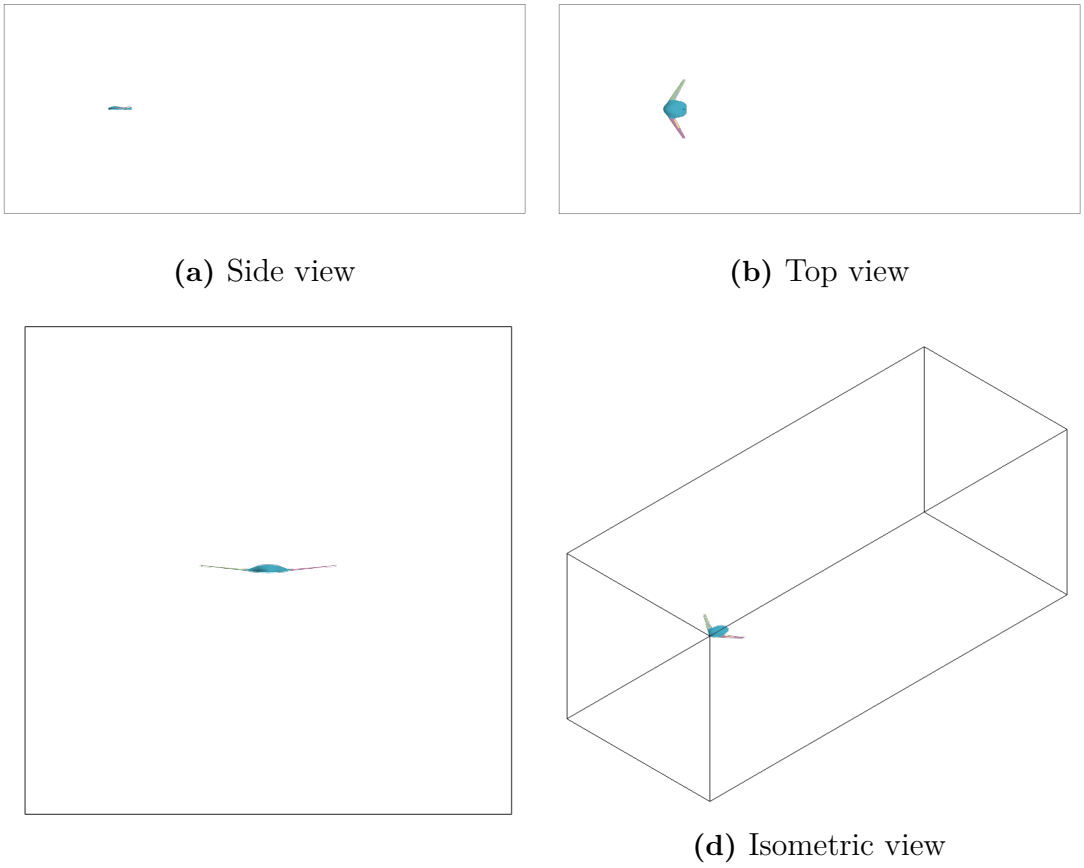

(a) Side view

(b) Top view

(c) Front view

(d) Isometric view

Figure 3.14: Freestream domain used in Star-CCM+.

The second domain used is the *"Blockage"* type, which was used to compare the results of the CFD model with the experimental data obtained in the Chalmers L2 tunnel. As the simulations only purpose was to check the validity of the CFD method, the domain had to be a digital replica of the real-life wind tunnel facility.

The Chalmers L2 wind tunnel has a test section with a octagonal cross-section that measures 3 meters in length, 1.8 meters in width and 1.25 meters in height [26]. The test section's cross-sectional slightly expands along its length to prevent growing boundary layers from interfering with the wind tunnel bulk flow. The outlet is located approximately 2.5 meters downstream of the test section. The aircraft along with its mounting in the wind tunnel is seen in Figure 3.15.

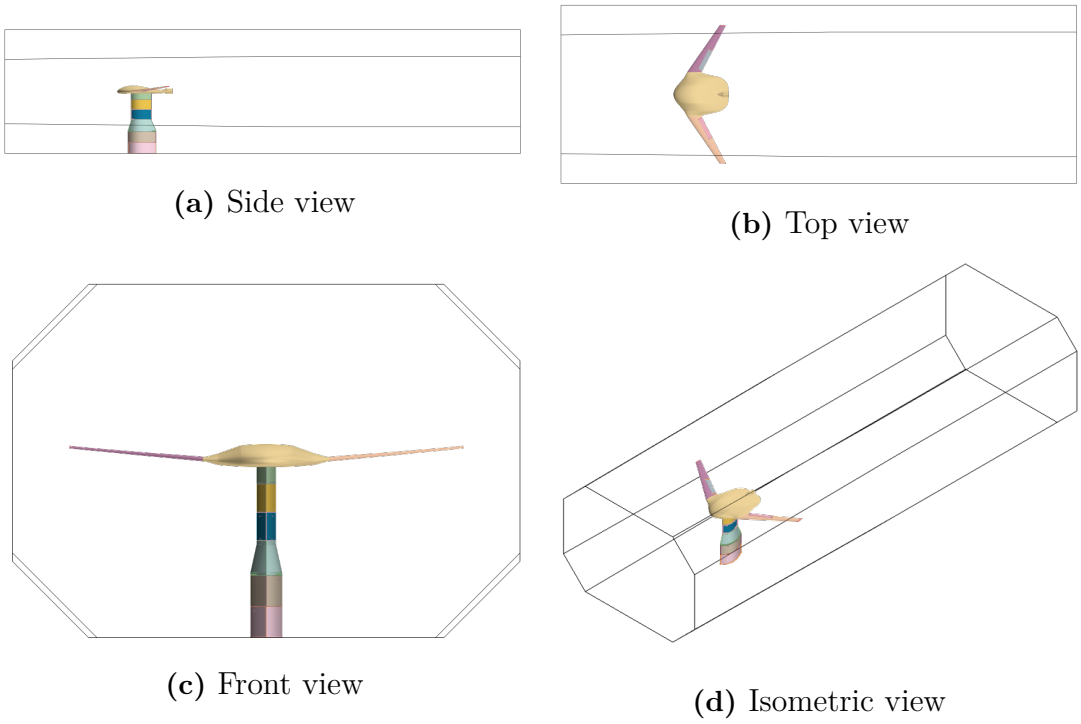

(a) Side view

(b) Top view

(c) Front view

(d) Isometric view

Figure 3.15: Chalmers L2 wind tunnel domain used in Star-CCM+.

3.3.2.3 Boundary conditions

The boundary conditions used for both domains are outlined in Table 3.7. The freestream domain uses a inlet with a specified velocity that corresponds to the freestream velocity, symmetry (zero wall-normal velocity gradient) along the upper, lower, left-hand and right-hand faces, and finally an outlet with a specified static pressure condition corresponding to a 0 Pa gauge pressure. The goal is to minimize any interaction that might affect the pressure distribution on the aircraft, as well as let any total pressure losses in the wake diffuse enough so that the outlet condition can be considered true.

For the wind tunnel domain the strategy is the opposite to that of the freestream case. In this case the goal is to capture the blockage effect given by the wind tunnel walls, which makes it possible to compare a CFD result with reality. The wind tunnel is equipped with a pitot tube upstream of the test section, which makes it possible for the inlet in CFD to be set as a specific velocity inlet. In addition, the turbulence intensity was set to value experimentally obtained in [27].The test section walls are modeled as normal no-slip boundaries, with the aim of reproducing the effect that the boundary layer has on the test section flow. Finally, the outlet of the tunnel is modeled as a boundary with unknown pressure and velocity condition in the flow exiting, and instead the conditions are determined by solving the upstream conditions. This will be computationally more heavy compared to a prescribed outlet condition, but is the safe solution when the outlet conditions are unknown.

Table 3.7: Boundary conditions chosen in Star-CCM+ for the two domains.

	Inlet	Outlet	Upper & lower	Left & right
Freestream	Velocity inlet	Pressure outlet	Symmetry	Symmetry
Blockage	Velocity inlet	"Outlet"	No-slip wall	No-slip wall

3.3.2.4 Mesh generation

It was decided early on to utilize the adaptive mesh functionality in Star-CCM+ as it would save on time and resources, well before the first proper simulation was run. While the mesh strategy still requires high-quality CAD geometry and high resolution in the surface mesh, it enables the user to have a much coarser bulk volume mesh. This cut down on memory usage and time spent during mesh generation, which made local pre-processing on a PC a possibility.

The first step in the meshing pipeline was to import the "watertight" CAD geometry using Star-CCM+'s built-in STEP importer. Care was taken in the import settings to fully capture intricate details such as the small radii wing leading and trailing edges.

After the aircraft had been transformed to the desired AoA and elevon settings, the geometry was subjected to a surface wrapping operation to ensure that the hinged elevons and motor housing, which were separate CAD entities, would be connected to the rest of the aircraft geometry. This operation is useful when the imported geometry is of low quality, which could be due to a tessellated surface with low polygon count, non-closed surfaces, non-manifold surfaces or self-intersections in the surface. In this case the aforementioned reasons were not a concern for the aircraft geometry, and surface wrapping was instead used to ensure a unified, fully closed surface.

To be able to generate a volume mesh, a void that represents the aircraft has to created within the domain. This is done using a subtract boolean operation, that removes the volume of object to be simulated from the wind tunnel domain. The result is a volume with two sets of boundaries: an outer boundary that is the inlet, outlet and walls of the domain, and an inner boundary that is the surface of the aircraft.

Next the automated meshing operation in Star-CCM+ was performed on the subtract volume. A mesh of *Trimmer*-type was used, which is an unstructured hexahedral-dominant method [19]. It works by generating a bulk mesh consisting of hexahedral elements, that is then "cut" by the surface mesh (or in this case a near-wall mesh). This leaves a transitional region where the so called trimmed cells reside, which are polyhedral cells that conform to the surface. Mesh refinements and growth rates are then implemented by splitting the hexahedral cells' faces by a multiple of two. It can be tricky to generate good-looking trimmer meshes, but its relatively cheap computationally and ensures that a majority of the cells are aligned with the flow direction, which ensures low numerical diffusion.

The aircraft requires so called prism cells (inflation layer cells) on its surface to be able to accurately capture the boundary layer. It was tuned to cover the entire boundary layer thickness, and to have enough resolution in all directions to capture the velocity gradient. It also merges into the bulk mesh in a smooth fashion. The settings used here were initially guessed by using flat-plate boundary layer theory. All of this ensures a low y^+ value mesh, which is required by the $k-\omega$ SST turbulence model. For the domain boundaries, prism layers were only required on the "blockage" domain's walls, as these produce a boundary layer.

The mesh settings used are summarized below in Table 3.8. These settings are based on recommendations from [25], which ensures at least 100 cells on the surface in the chordwise direction. The prism layer settings are tuned to smoothly merge with the bulk mesh, achieve a target y^+ equal to one for to be able to resolve the entire boundary layer, and finally to fully encompass the surface without retracting. An example of how the prism layers look like can be seen in Figure 3.16, where a cross-section of the mesh near the aircraft body is be seen.

Table 3.8: Mesh settings used in Star-CCM+ for both the freestream and wind tunnel case.

	Body	Wings
Base size	0.4 m	0.4 m
Target Surface Size	0.8% of base	0.2% of base
Minumum Surface Size	0.2% of base	0.04% of base
Surface Mesh Growth Rate	1.1	1.1
Number of Prism Layers	32	20
Prism Layer Near Wall Thickness	9.9E-6 m	8.7E-6 m
Prism Layer Total Thickness	0.02 m	0.0036 m
Trimmer Volume Growth Rate	Medium	Medium
Trimmer Surface Growth Rate	Medium	Slow
Maximum Cell Size	25% of base	25% of base

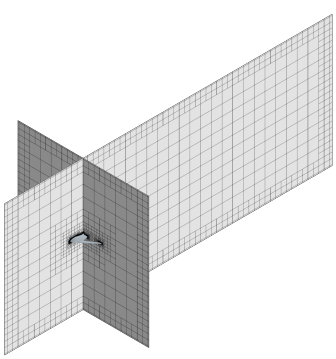

(a) Entire domain

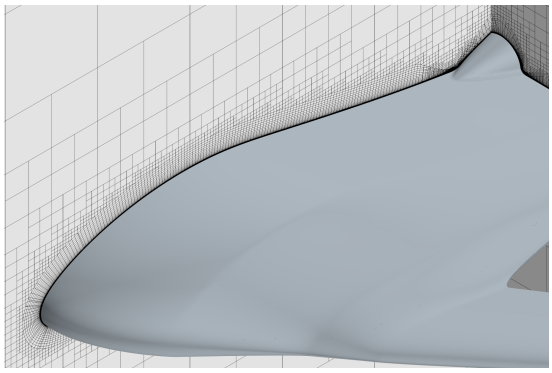

(b) View near aircraft surface

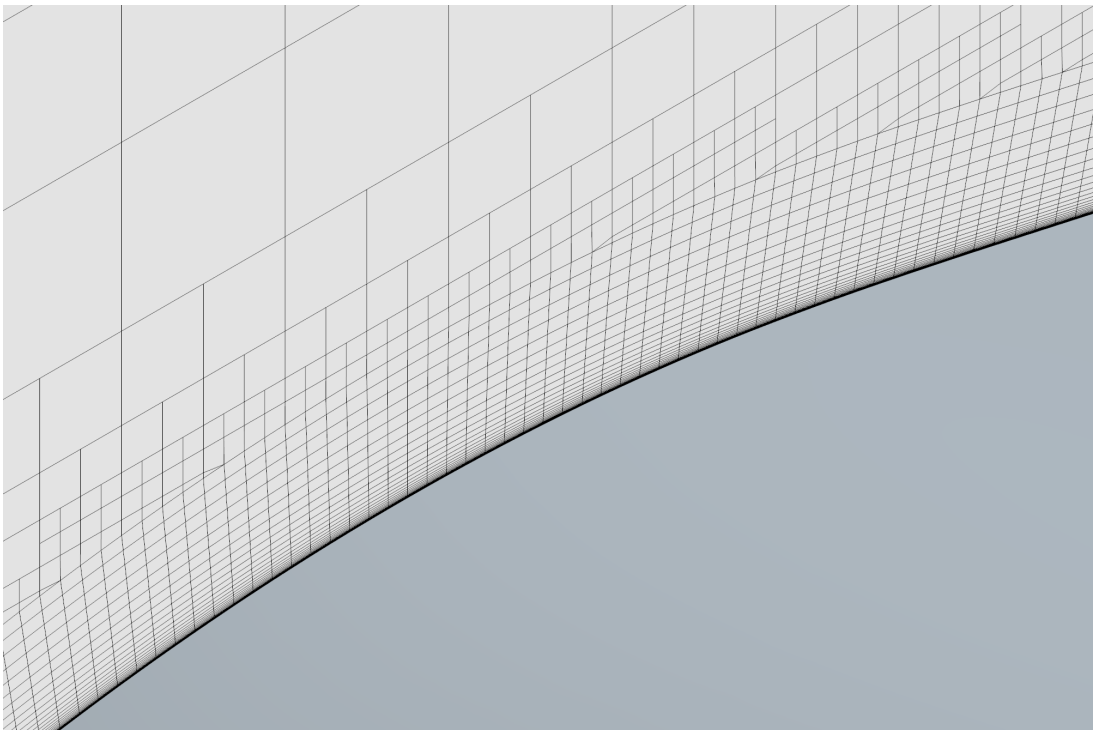

(c) Close up of prism layer cells merging into bulk mesh

Figure 3.16: Visualization of the volume mesh in the freestream case, pre-adaption.

The built-in mesh adaptation was triggered during solving to perform local refinements where flow gradients were large. Following recommendations by Siemens for external aerodynamics [19], the adaptation field function was chosen as the Laplacian of the total pressure. The adaptation routine was triggered every 25 iterations during the initial 250 iterations. The value of adaptation function is calculated for each cell in the mesh, and will either coarsen (initial mesh is the limit for coarseness) a cell if below a minimum scalar threshold, or refine by splitting a cell into four if above the maximum scalar threshold. The result is a mesh that is refined in areas with high vorticity or large wake losses. Figure 3.17 shows the inital mesh before solving, and Figure 3.18 shows the mesh after the final adaptation was triggered.

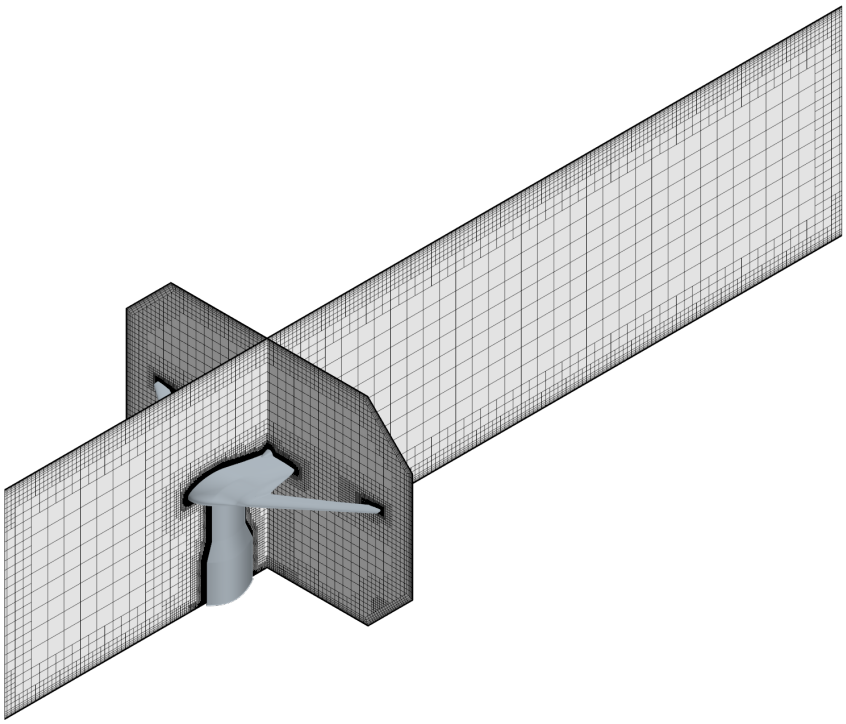

Figure 3.17: Mesh in the wind tunnel domain, before adaptation.

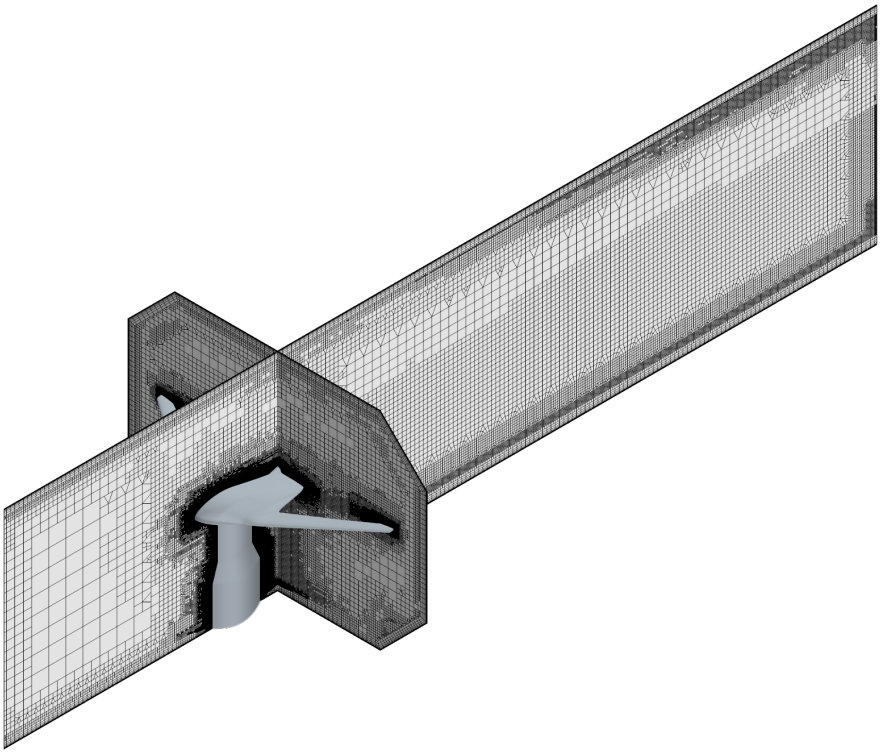

Figure 3.18: Mesh in the wind tunnel domain, after adaptation.

The described meshing strategy provides short turnaround time, while ensuring

numerical accuracy.

3.4 Structural evaluation

A structural evaluation is done in order to get a mass estimation of the hull and perform a sensitivity analysis resulting in a target for wingtip deflection.

3.4.1 Structural concept

A structural concept with an external *Carbon Fibre Reinforced Polymer* (CFRP) shell and internal plastic structure is designed with the goal of ensuring high stiffness over mass. Control surfaces are expected to provide no support for the wing and are thereby excluded from the structural simulation. The payload is designed to carry all electronic components along with a cargo bay that fits the heart defibrillator, the payload is bolted to the rest of the structure so that all electronic components can be assembled in the payload and then easily mounted into the wing.

3.4.2 ANSYS 2021R1 setup

ANSYS ACP-pre is used to setup a baseline layup of a 0.16 mm thick CFRP outer shell consisting of 2 layers 80 *Gram per Square Metre* (GSM) Textreme, one layer at 0 degrees towards spanwise direction and one at 45 degrees resulting in almost quasi-isotropic laminate material properties. A surface mesh is generated with a base size of 8 mm and standard refinement. ANSYS mechanical model is used to setup the internal structure of the 3D printed *polylactide* (PLA) plastic, that is meshed with a base size of 5 mm and standard refinements. The outer shell along with the internal structure are imported to ANSYS static structural and bonded together. Surface pressures are exported from Star-CCM+ at 1 AoA and 35 m/s and imported as load and the aircraft is fix supported in the vertical center plane.

3.5 Wind tunnel testing

The CFD model is validated by testing two full-scale models, one 3D-printed in plastic and one carbon fibre reinforced, at Chalmers' wind tunnel facility. The test results do not represent the final performance due to interference and blockage arising from the mountings and the tunnel physical boundaries. The tests are instead compared to a CFD model including blockage, as described above.

3.5.1 Test rig design

The first step is to decide upon what quantities to collect for validation and what parameters to have adjustable. Lift-, drag-force, pitch moment and flow feature visualisation were the main quantities gathered for validation. The forces and moments are gathered from two different load cells, one mounted below the floor of the wind tunnel measuring 3D forces and 3D moments, another load cell mounted close

to the CoG of the aircraft measuring lift, pitch- and roll-moments in the aircraft coordinate system. The data is then gathered while sweeping angle of attack, velocity and elevon angles. The measured quantities, visual observations and adjustable parameters are listed as:

Measured quantities
Lift force
Drag force
Pitch moment Roll moment

Visual observations
Flow feature visualisation
Deformations

Adjustable parameters
Pitch angle
Velocity
Elevon angles

Table 3.9: The measured quantities, visual observations and adjustable parameters utilized during wind tunnel testing.

The goal is to isolate and measure forces on the aircraft alone, the main issue is that the load cell mounted in the aircraft measures all quantities except the drag force. Therefore the drag force is measured using the load cell mounted below the floor of the wind tunnel, the drag from the mounting should be minimized for the forces measured to be isolated to the aircraft and not influenced by mountings.

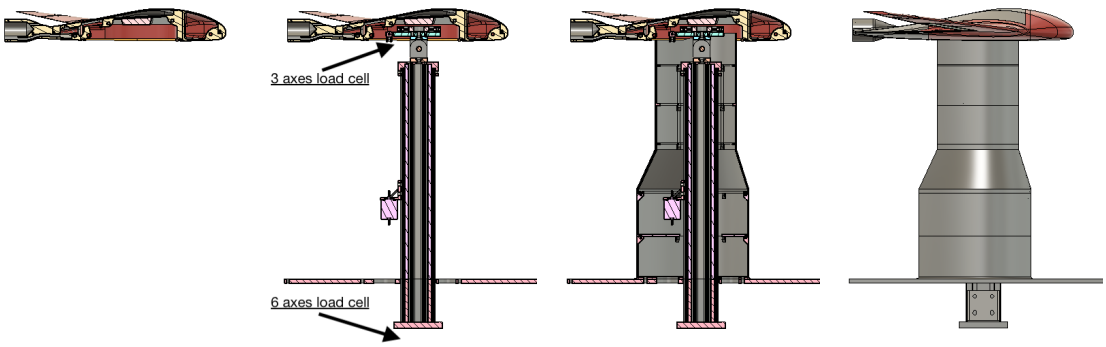

(a) Test object **(b)** Stand **(c)** Cover **(d)** Assembled

Figure 3.19: Wind tunnel rig assembled by the test object mounted on to the stand that is shielded from drag by a cover.

The rig, as displayed in figure 3.19 is divided into multiple parts where the test object (aircraft) is mounted onto the 3 axes load cell that sits on a remotely controlled pitch stage. An aluminum strut stand then connects the pitch stage to the 6 axes load cell mounted below the tunnel. A standalone cover is used to block the airflow on the stand and protrudes through the bottom hatch of the aircraft without touching either the stand nor the aircraft to ensure that no forces are absorbed by the cover.

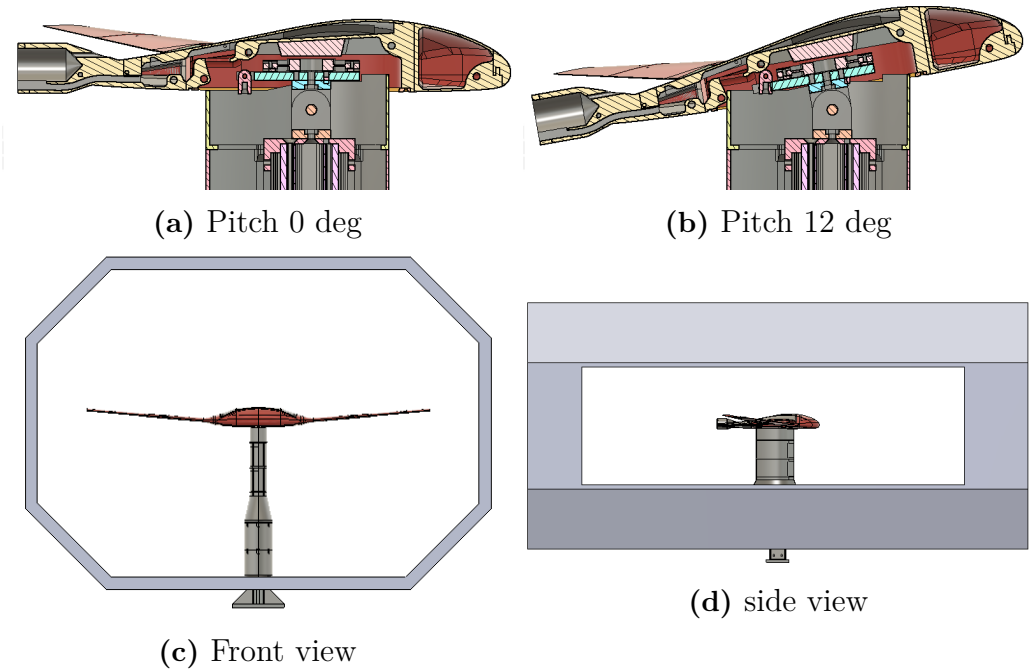

(a) Pitch 0 deg

(b) Pitch 12 deg

(c) Front view

(d) side view

Figure 3.20: Pitch movement and mounting of the rig in the wind tunnel.

3.5.2 Setup and calibration

The aircraft is mounted and adjusted to a position where it is free to pitch from -2 to 12 degrees without any contact with the cover, the designed adjustability is ±5 mm in all directions and the end error margin in positioning is ±10 mm. The absolute pitch angle is measured using a protractor with 0.05 deg resolution that is calibrated to zero on a rigid section of the wind tunnel floor, the same protractor is used to ensure that the pitch rate is correct by measuring at multiple angles and also to ensure repeatability. Roll and yaw angles are measured with an estimated max error is ± 0.2 deg. The lower load cell samples at a rate of 1 kHz and every extracted value is an average of 3000 samples (3 seconds) while the upper load cell samples at 25 a rate of kHz and is averaged over 75000 samples (3 seconds), 7 samples are gathered for every measurement point. The upper load cell has a maximum load of 200N/4Nm/4Nm ($F_z/M_x/M_y$) with an error of ±0.1/0.065/0.05% ($F_z/M_x/M_y$) while the lower has maximum load of 90N/200N/30Nm/60Nm ($F_{xy}/F_z/M_{xz}/M_y$) a error of ±0.2%. The setup is tested after mounting by placing known weights at known leverage arms to validate that load cells give correct readings.

3.5.3 Testing and post-processing

Tests are performed by setting one pitch angle and sweeping velocity from 0 to an upper limit depending on the pitch angle and then back to 0. The static case is always included since pitching the aircraft changes the CoG position, relative to the scale, and thereby the static forces and moments which are then subtracted from all other measurements at that pitch angle. The velocity sweep ends with another

static case to ensure no measured quantities has changed over time or due to other faults.

Another set of test cases are done with cameras mounted above and behind the aircraft to capture images of deformations and flow features. An oil mixture with white pigments is applied on the aircraft and recorded to get a visualisation of skin friction and surface flow paths.

All results are then post processed in matlab where the measured quantities for every test case is evaluated to find max, min and mean of the 7 measurements, mean values will be considered unless any outliers are found. The data is interpolated to find pitch angle for zero lift and shifted to match CFD where it is assumed that the test object corresponds well to CFD simulations, small errors in pitch angle are adjusted for since it's assumed to be caused by mounting faults.

3.5.4 Initial conclusions

The first plastic model tested deformed significantly at the wing tips. The deformation was estimated using camera footage to be 10 mm and CFD simulations of a similarly deformed aircraft showed a loss of lift of around 5% at 1 deg angle of attack and 35 m/s. Another model was then printed with a higher number of solid walls that deformed 6 mm instead. This reduced the performance loss at high loads but deformations were further noted, since they were even smaller for the carbon plane which could lead to a difference in test results.

First tests using flow visualisation oil showed a big disturbance around the elevon mounting. Sealing the gap from underneath increased lift noticeably and all tests on the plastic model were conducted with the gap sealed, on the carbon fibre model this gap was taken into consideration and designed to be smaller and allow for less leakage.

4

Results

This chapter begins with a comparison of the CFD results including blockage to experimental test results. Then it highlights the effects from blockage by comparing results from the CFD simulations with and without blockage. Finally it presents the final geometry and its aerodynamic and structural predictions.

4.1 Wind tunnel validation

The present section presents the results of the validation study done for numerical methods by gathering experimental data in wind tunnel. First, forces and moments are compared, then flow features are compared.

4.1.1 Forces and moments

CFD simulations including blockage are compared to wind tunnel experimental data obtained for a 3D printed plastic and the carbon fibre model. Two sequences are compared, first a angle of attack variation at 20 m/s and then a velocity variation at angle of attack 1.

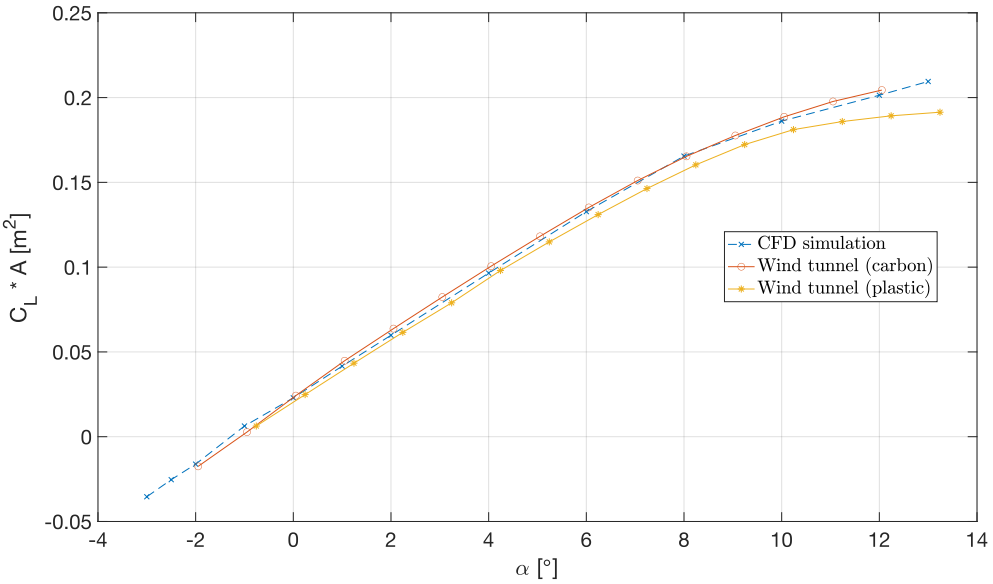

Figure 4.1: $C_L \cdot A$ variation with angle of attack at 20 m/s

Figure 4.1 displays a variation of $C_L \cdot A$ with angle of attack at 20 m/s. The comparison with experimental results show a constant offset for low angles of attack and increasing error for the plastic model at high angles of attack.

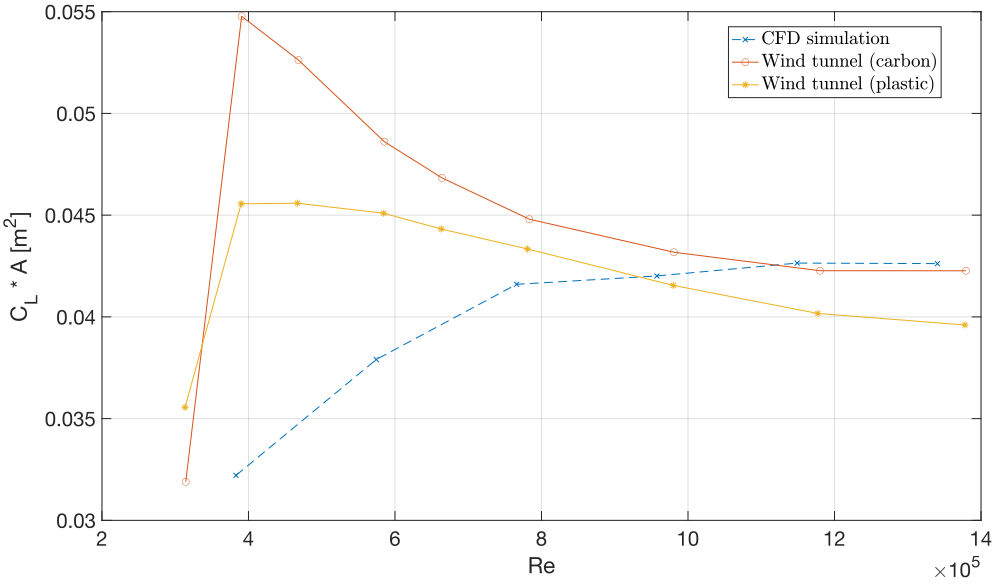

Figure 4.2: $C_L \cdot A$ variation with Reynolds number at an AoA of 1 deg

Figure 4.2 display the variation of $C_L \cdot A$ with Reynolds number for an AoA of 1 deg and shows that values start out different but converge to similar values.

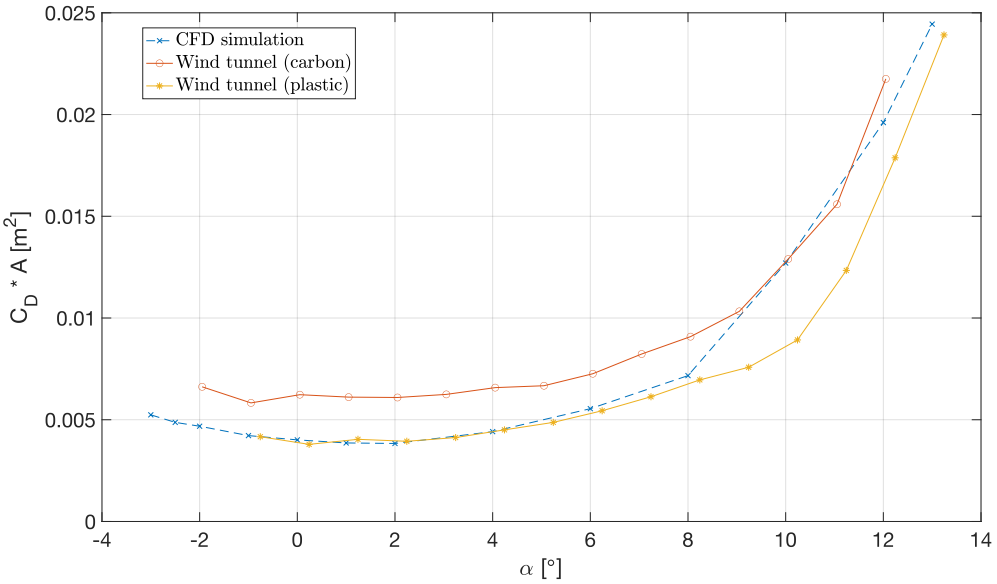

Figure 4.3: $C_D \cdot A$ variation with angle of attack at 20 m/s

Figure 4.3 shows the variation of $C_D \cdot A$ with angle of attack at 20 m/s. The numerical results follow the trend of experiments at low angles of attack and the drag offset is higher for the carbon fibre aircraft.

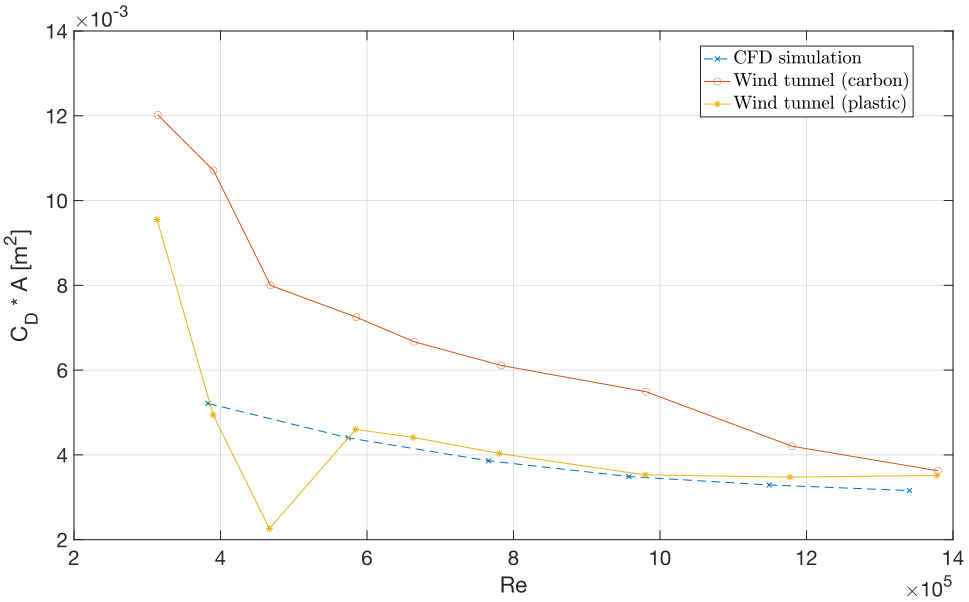

Figure 4.4: $C_D \cdot A$ variation with Reynolds number at an AoA of 1 deg

Figure 4.4 shows the variation of $C_D \cdot A$ with Reynolds number at an AoA of 1 deg. The $C_D \cdot A$ values converge at higher velocity and that the carbon fibre aircraft is subject to higher drag.

Note that drag was not a primary target to measure and that results have lower resolution then lift and moments

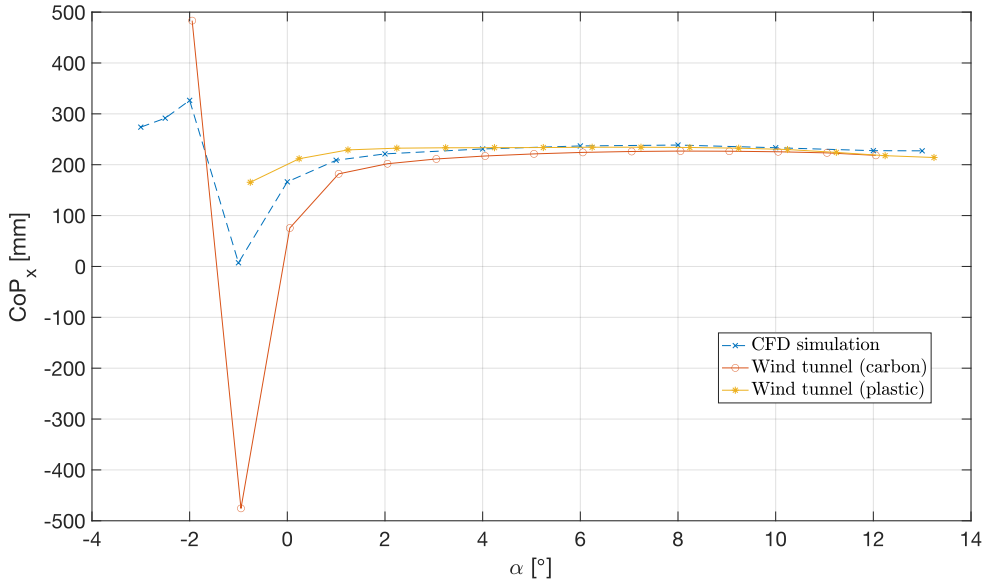

Figure 4.5: CoP_x variation with angle of attack at 20 m/s

Figure 4.5 shows the variation of CoP_x with angle of attack at 20 m/s. The numerical models predicts trends well but values match better at high angles of attack.

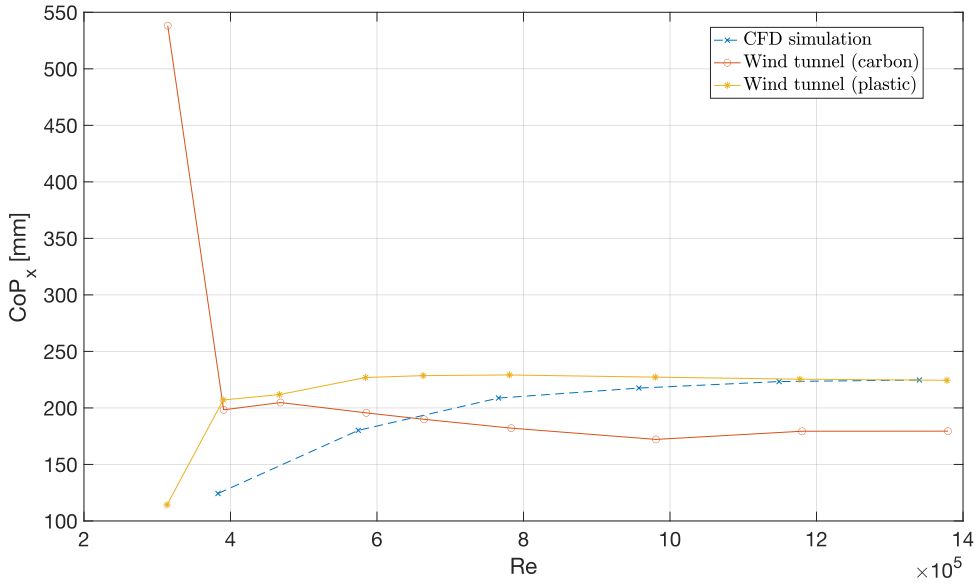

Figure 4.6: CoP_x variation with Reynolds number at an AoA of 1 deg

Figure 4.6 shows the variation of CoP_x with Reynolds number at an AoA of 1

deg. Predicted values differ at low velocity and match experimental results, at high velocities, better for the plastic model then the results from the carbon fibre model.

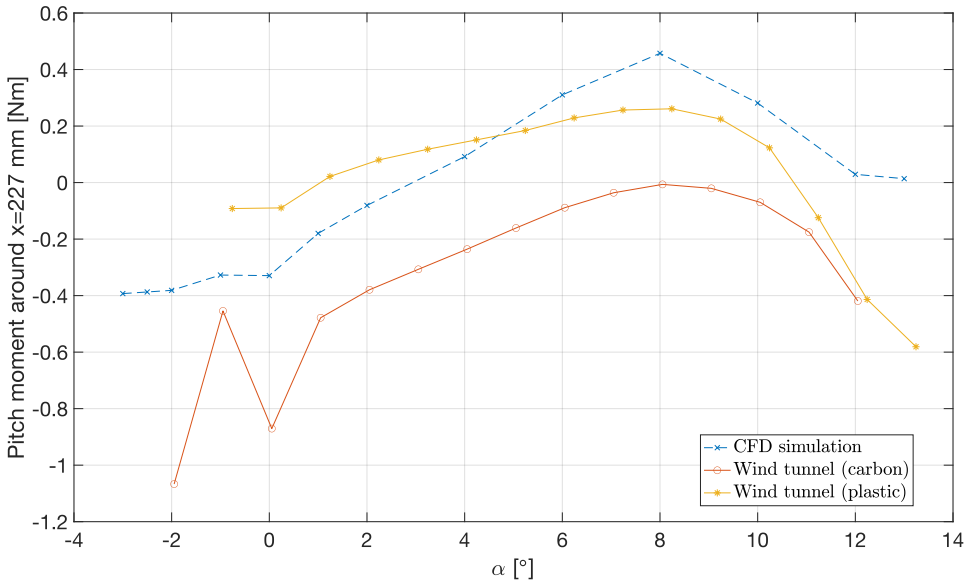

Figure 4.7: M_p variation around x=227 mm, with angle of attack at 20 m/s

Figure 4.7 shows the variation of pitch moment, around center of gravity, with angle of attack at 20 m/s. Predicted pitch moment magnitudes differ compared to experimental results but all seems reach a maximum value at an AoA of 8 deg.

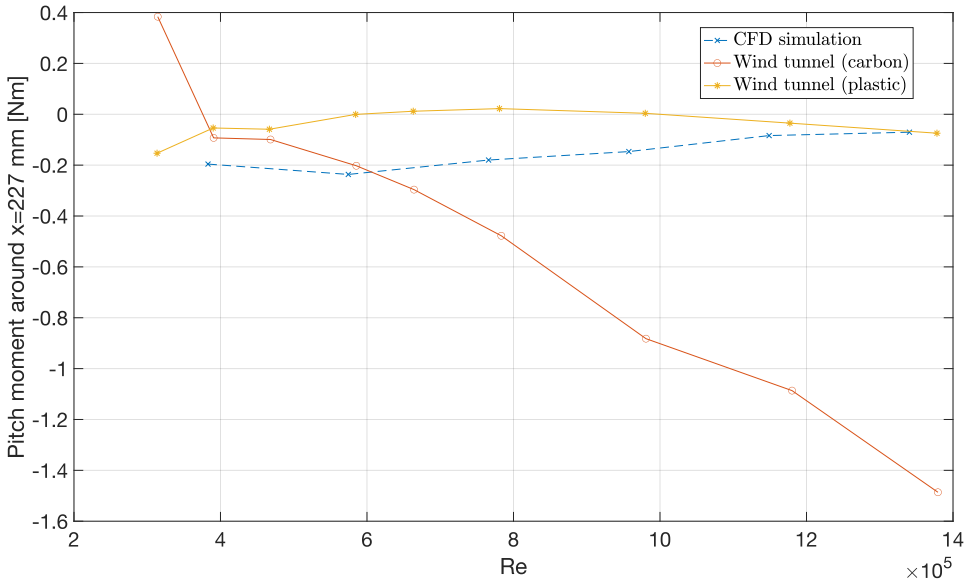

Figure 4.8: M_p variation around x=227 mm, with Reynolds number at an AoA of 1 deg

Figure 4.8 shows variations of pitch moment, around center of gravity, with Reynolds number at an AoA of 1 deg. the difference in CoP_x has a greater impact at higher velocities.

4.1.2 Flow visualisation

Wall-shear stress was visualised using an emulsion of white titanium dioxide particles and a kerosene–SAE 10W-40 mix which is moved by the airflow until a steady-state is reached. One sweep of AoA is done at a fixed speed of 20 m/s and a sweep of Reynolds number was performed at $AoA = 1°$. Regions where the flow visualization solution accumulates indicates low wall-shear stress.

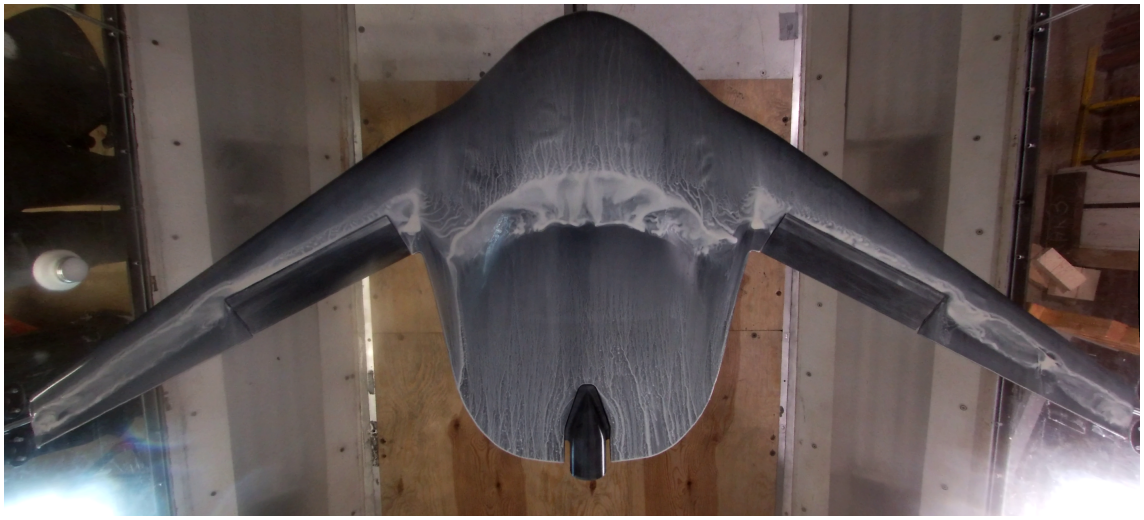

Figure 4.9: Flow visualization, $AoA = 1°$, $v = 20m/s$

It is observed in Figure 4.9 that a distinct region has formed from the wing-tip to the wing root, which then stretches across the body in the spanwise direction.

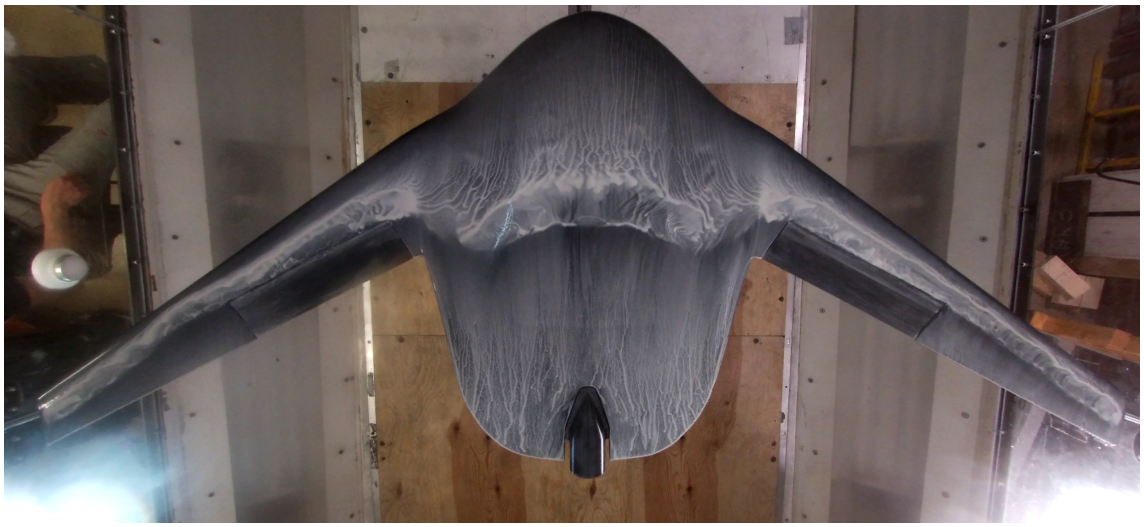

Figure 4.10: Flow visualization, $AoA = 4°$, $v = 20m/s$

Compared to Figure 4.9, Figure 4.10 shows that the white region has moved upstream in the chordwise direction, both in the wings and in the body.

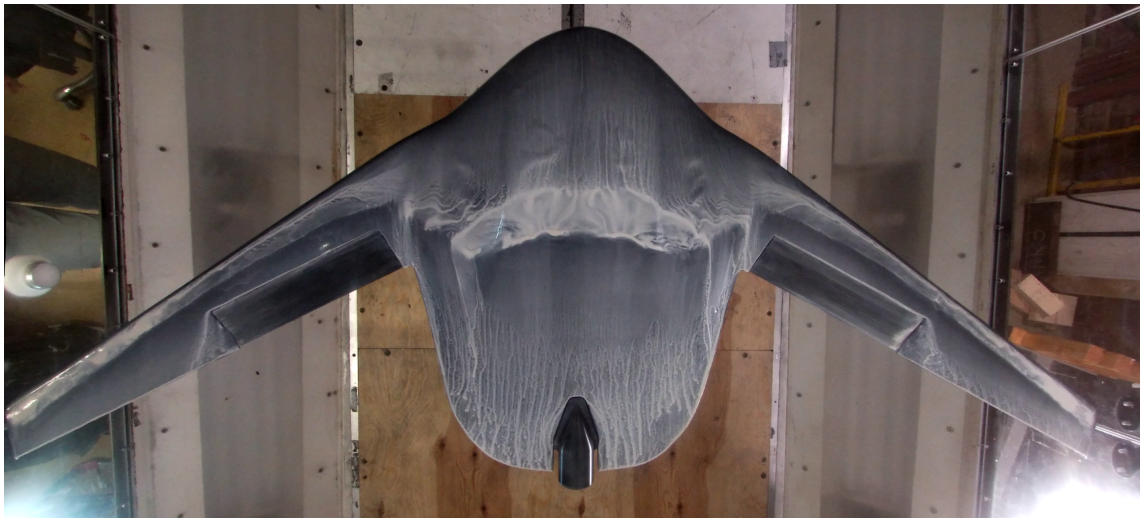

Figure 4.11: Flow visualization, $AoA = 6°$, $v = 20m/s$

In Figure 4.11, the region of accumulated emulsion has further moved upstream, and a new pattern has emerged on the wing which eminates from the elevon leading edge's most outboard portion.

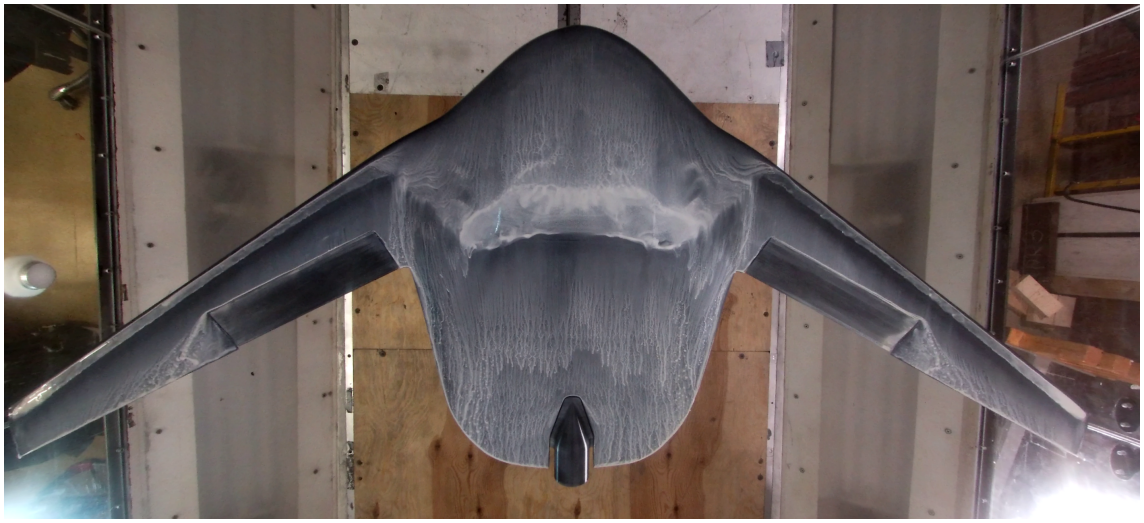

Figure 4.12: Flow visualization, $AoA = 8°$, $v = 20m/s$

In Figure 4.12 the region of accumulated liquid has further moved upstream. The part of it present on the wings has contracted in the chordwise direction.

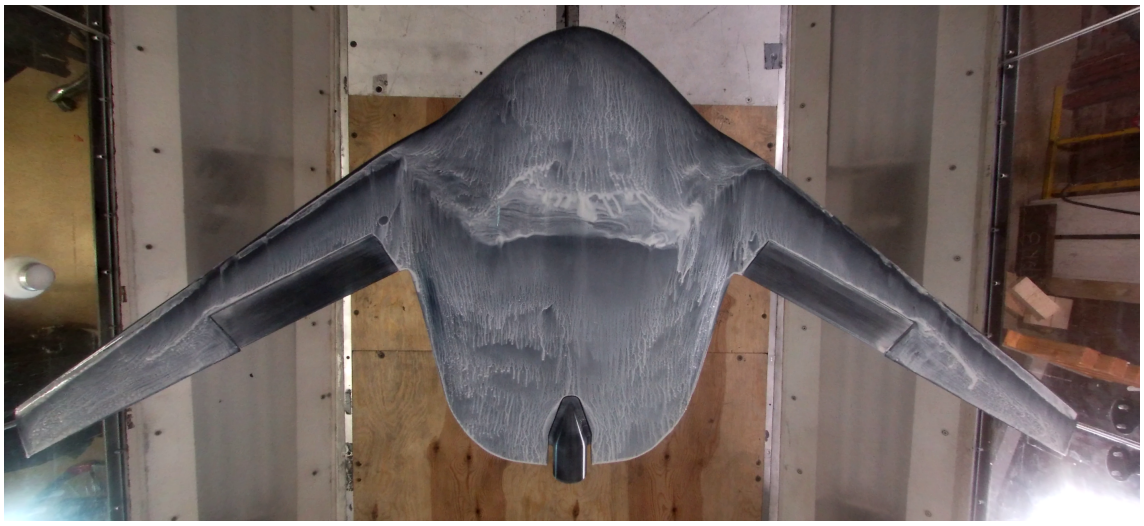

Figure 4.13: Flow visualization, $AoA = 10°$, $v = 20m/s$

The region of accumulated liquid continues to move upstream in Figure 4.13, and the the part of it present on the wings is observed to experience a breakup and is therefore no longer continuous in the spanwise direction.

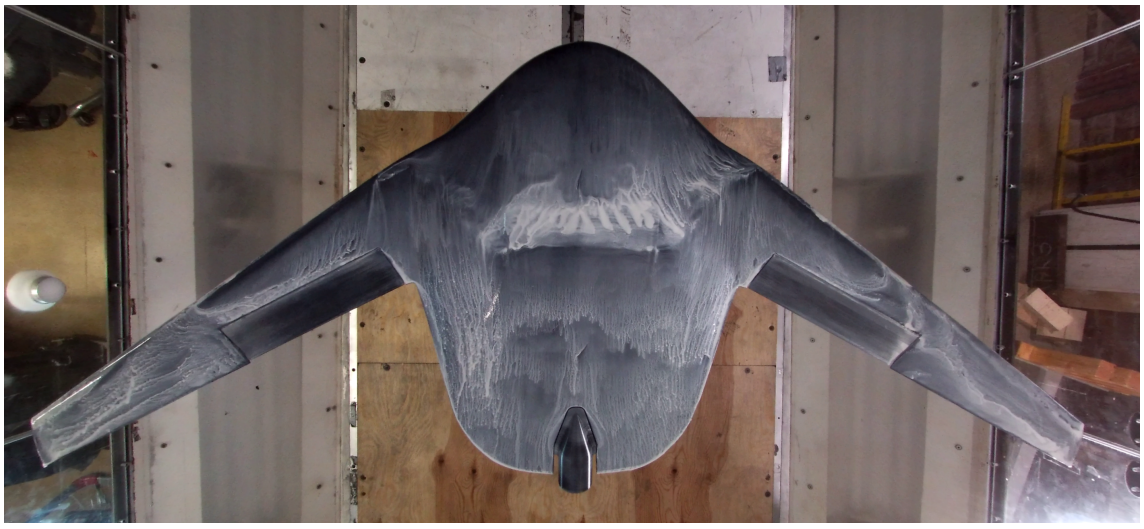

Figure 4.14: Flow visualization, $AoA = 12°$, $v = 20m/s$

Figure 4.14 exhibits a more chaotic flow pattern, with a region of accumulated flow visualization solution at the body, and the absence of a clear distinct white streak on the wing in the spanwise direction. Outboard of the elevon, the wing is completely white, which indicates minuscule or a complete lack of skin friction.

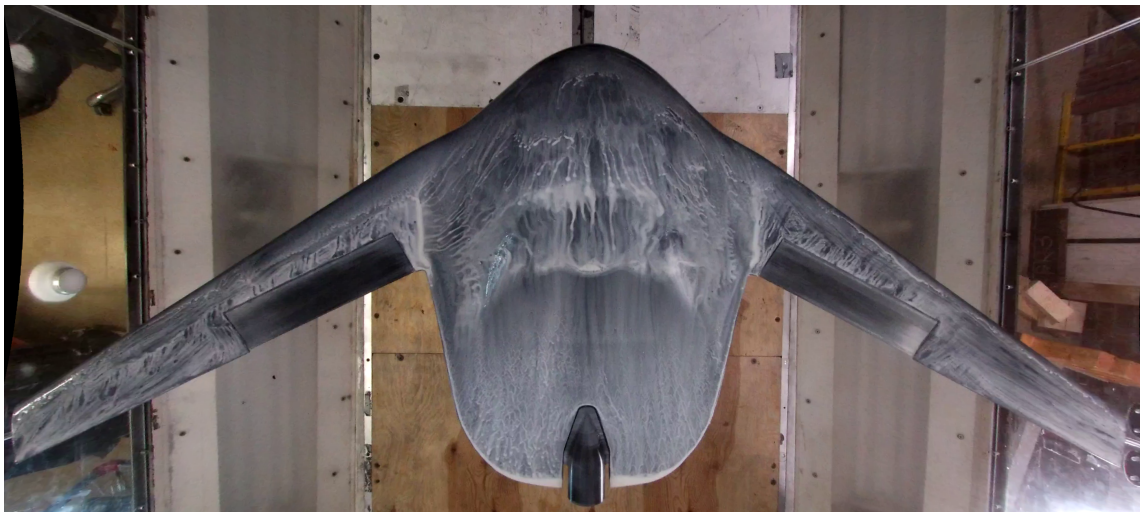

Figure 4.15: Flow visualization, $AoA = 1°$, $v = 8m/s$

Figure 4.15 shows a pattern of vague flow visualization feature lines. An area of accumulation is seen in the body as in the previous section, although wider in the chordwise direction, as well as in the wing inboard of the outboard portion of the elevon. Outboard of the elevon, no distict pattern is observed.

In Figures 4.16, 4.9 and 4.17, it is observed that the pattern gets more distinct as the flow speed is increased. The chordwise length of the body accumulation contracts significantly, which is also evident on the wings. The region outboard of the elevon forms an observable pattern at $v = 20m/s$.

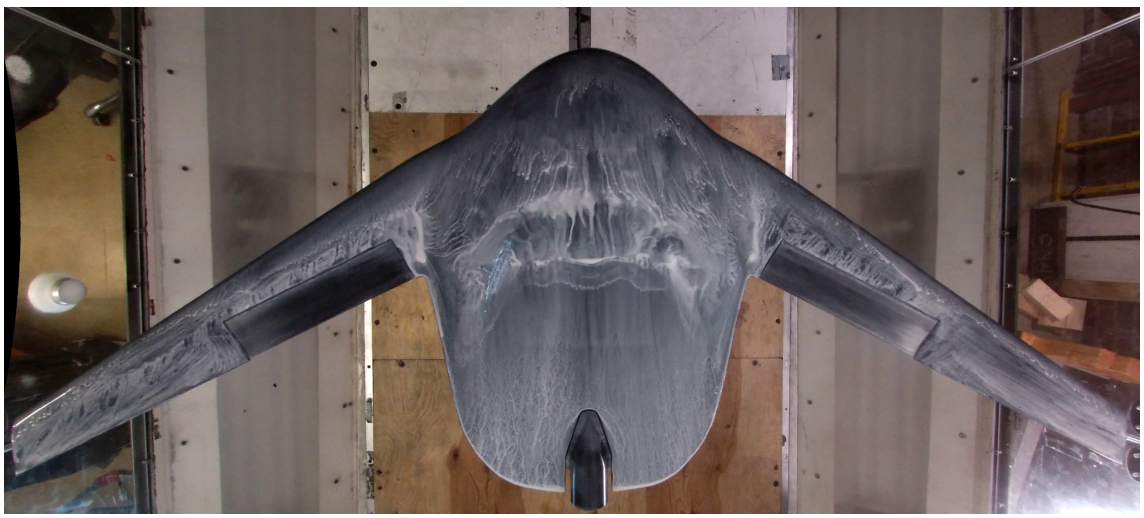

Figure 4.16: Flow visualization, $AoA = 1°$, $v = 10m/s$

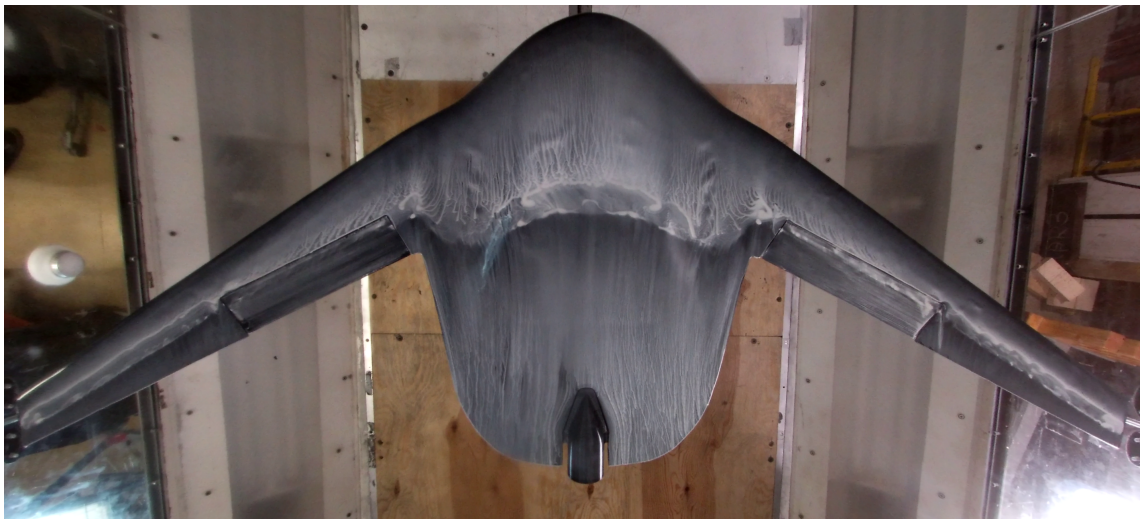

Figure 4.17: Flow visualization, $AoA = 1°$, $v = 35m/s$

Images comparing the flow visualization to skin friction contours from simulations for a handful of cases are seen below in Figures 4.18, 4.19 and 4.20. Due factors such as lens perspective and distortion it is difficult to perfectly align the real-life images with the CFD contour plots. The results below are therefore only to be judged qualitatively.

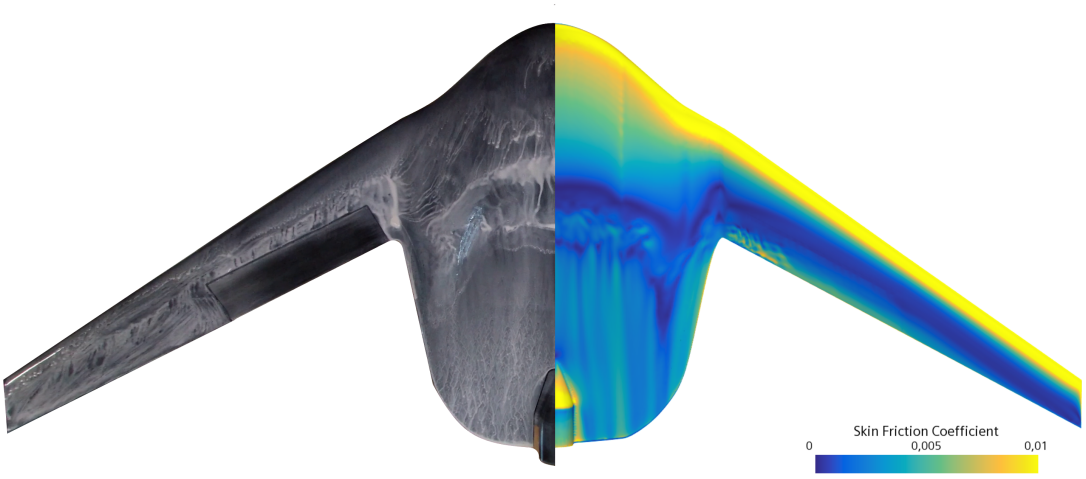

Figure 4.18: Flow visualization compared with skin friction contours, $AoA = 1°$, $v = 10m/s$

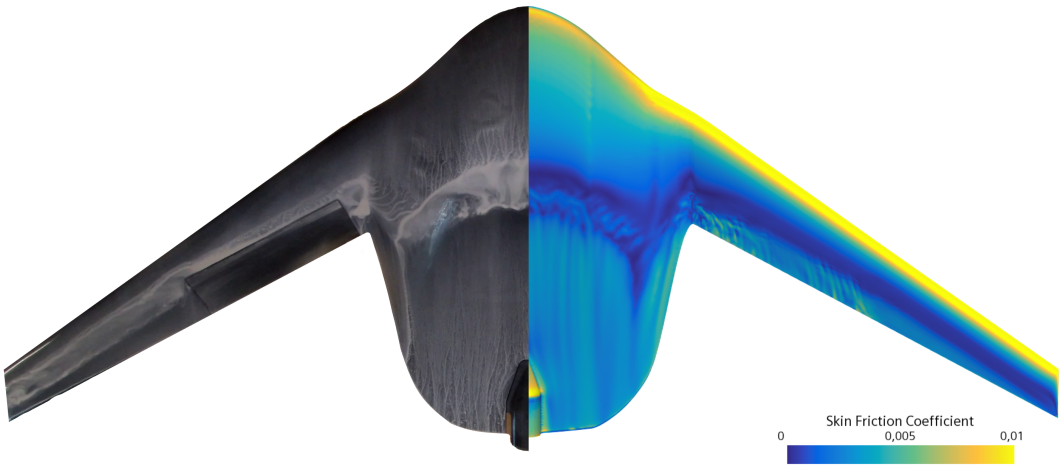

Figure 4.19: Flow visualization compared with skin friction contours, $AoA = 1°$, $v = 20m/s$

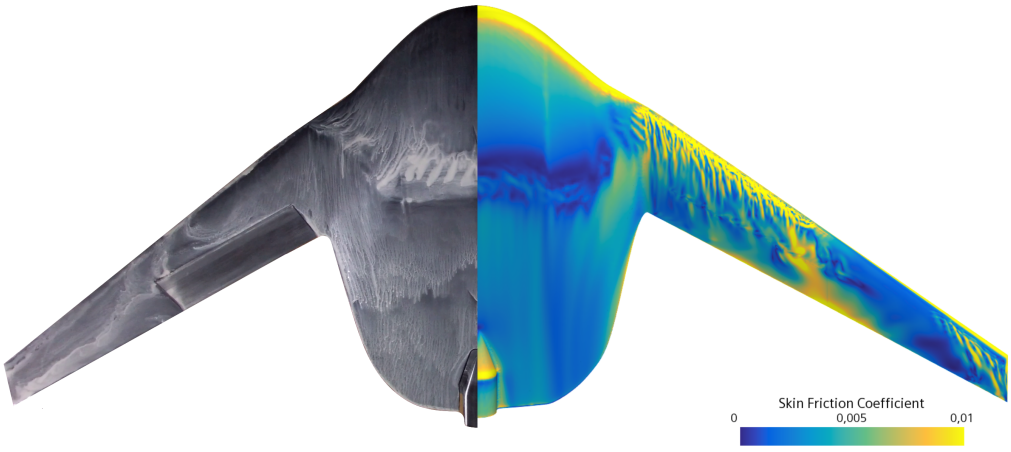

Figure 4.20: Flow visualization compared with skin friction contours, $AoA = 12°$, $v = 20m/s$

4.2 Blockage effect

A comparison between the aircraft simulated performance with and without blockage from the wind tunnel and mounting is presented in the present section.

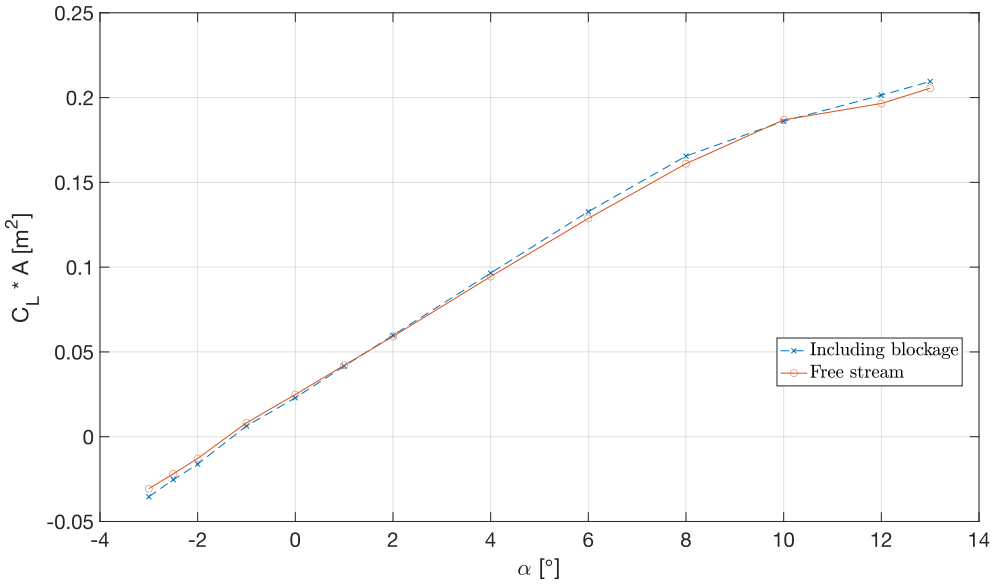

Figure 4.21: $C_L \cdot A$ variation with angle of attack at 20 m/s

Figure 4.21 shows the variation of $C_L \cdot A$ with angle of attack at 20 m/s. The numerical model with blockage has higher lift at high angles of attack and higher negative lift at low angles.

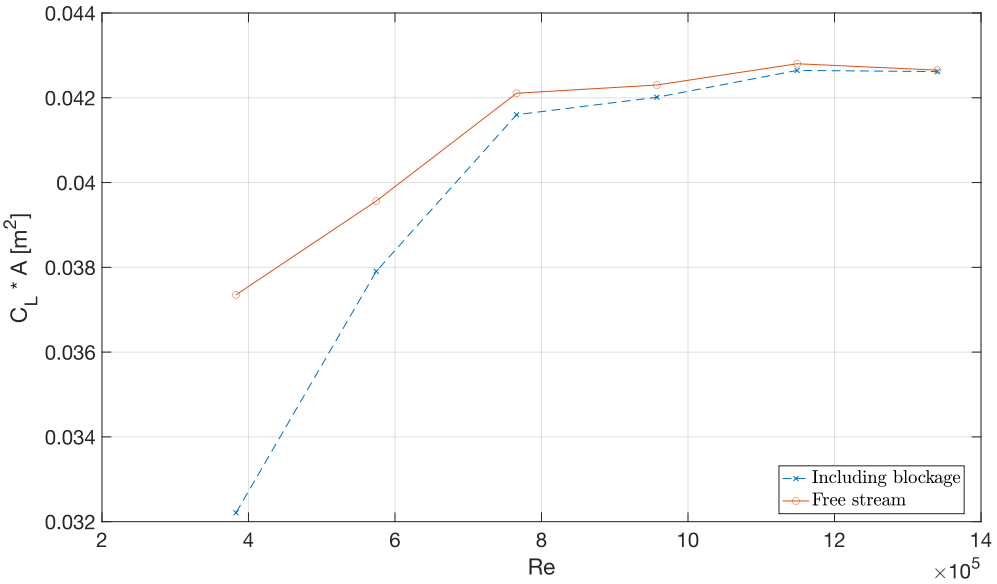

Figure 4.22: $C_L \cdot A$ variation with Reynolds number at an AoA of 1 deg

Figure 4.22 shows the variation of $C_L \cdot A$ with Reynolds number at an AoA of 1 deg. The numerical models predict a big difference at low velocities and smaller difference at higher velocities.

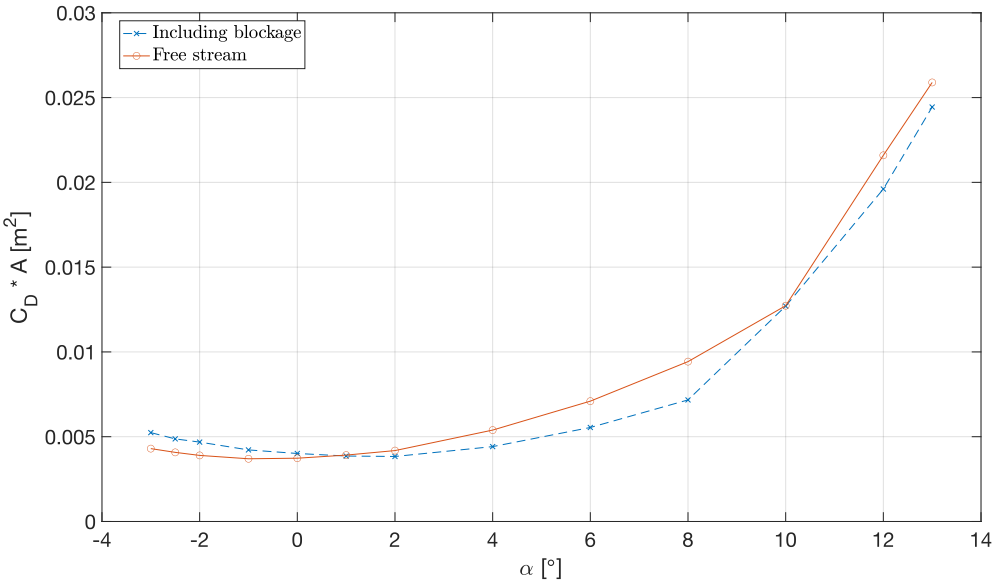

Figure 4.23: $C_D \cdot A$ variation with angle of attack at 20 m/s

Figure 4.23 shows the variation of $C_D \cdot A$ with angle of attack at 20 m/s. The numerical model including blockage predict higher drag until an AoA of 1 deg and then come very close again at an AoA of 10 deg.

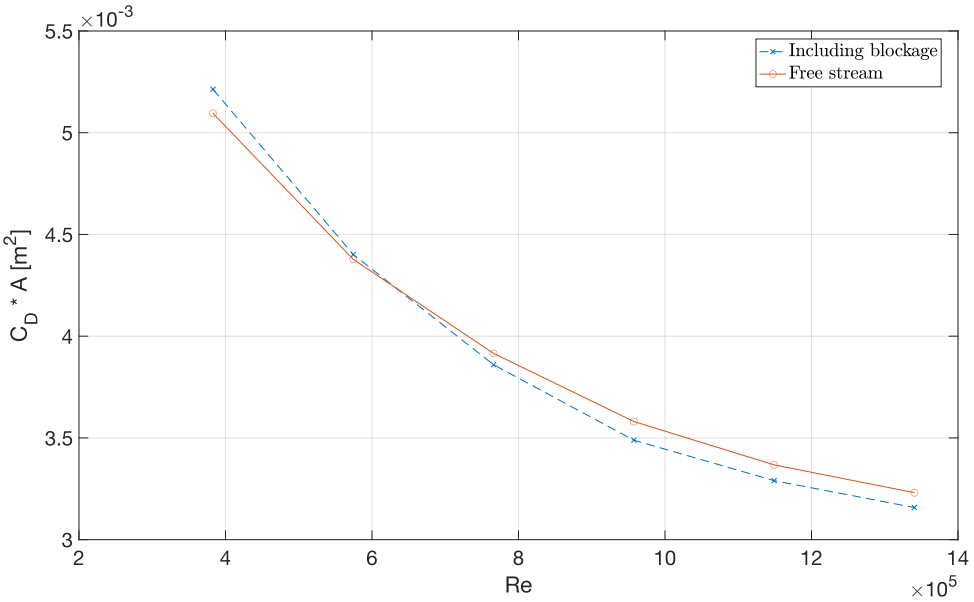

Figure 4.24: $C_D \cdot A$ variation with Reynolds number at an AoA of 1 deg

Figure 4.24 shows the variation of $C_D \cdot A$ with Reynolds number at an AoA of 1 deg. Numerical model including blockage predicts higher drag at low velocities and then lower at higher velocities.

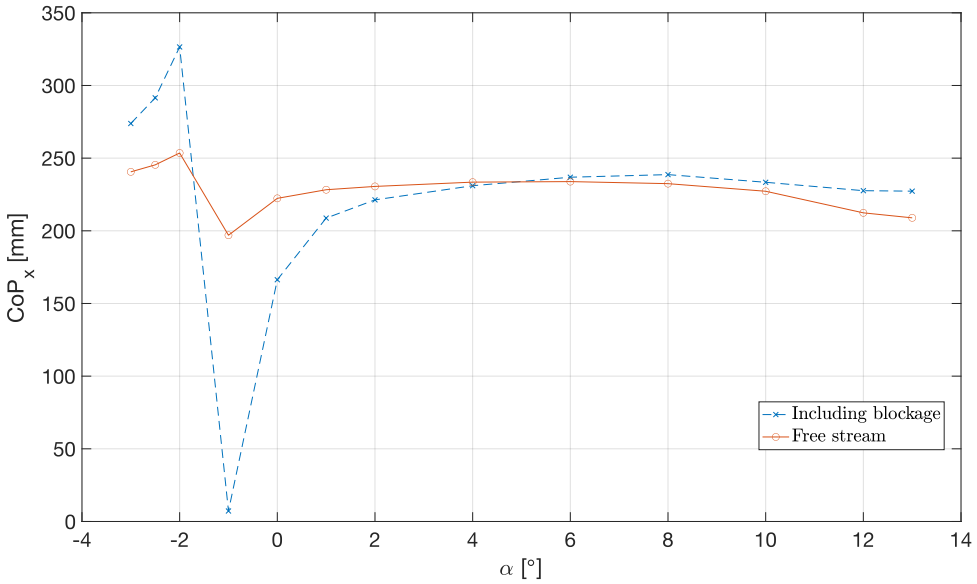

Figure 4.25: CoP_x variation with angle of attack at 20 m/s

Figure 4.25 shows the variation of CoP_x with angle of attack at 20 m/s. The numerical models predicts that blockage has a high influence on center of pressure, especially around angle of attack -1 where the aircraft transitions from producing downforce to lift.

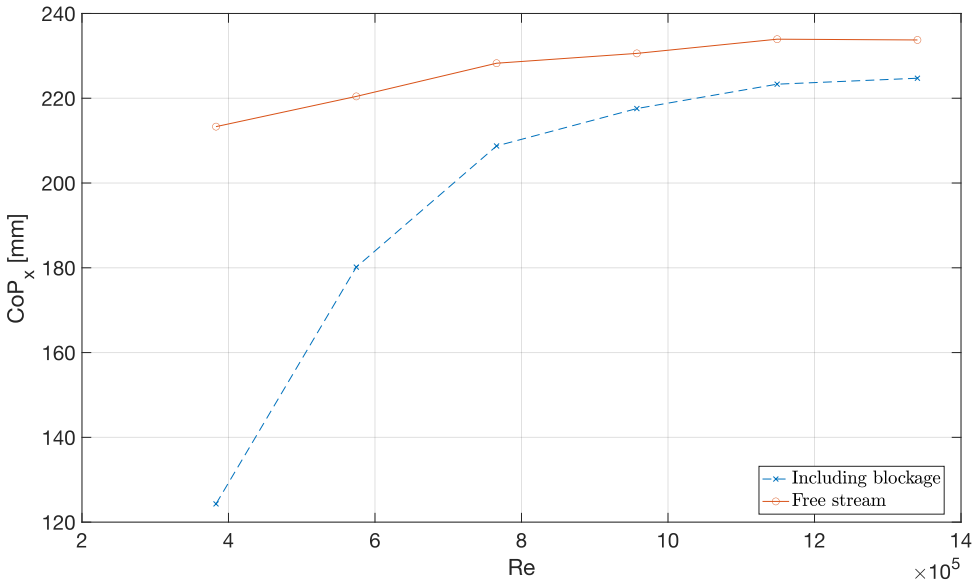

Figure 4.26: CoP_x variation with Reynolds number at an AoA of 1 deg

Figure 4.26 shows the variation of CoP_x with Reynolds number at an AoA of 1 deg. The numerical model including blockage has its center of pressure further forwards

and the center of pressure moves more for the model including blockage.

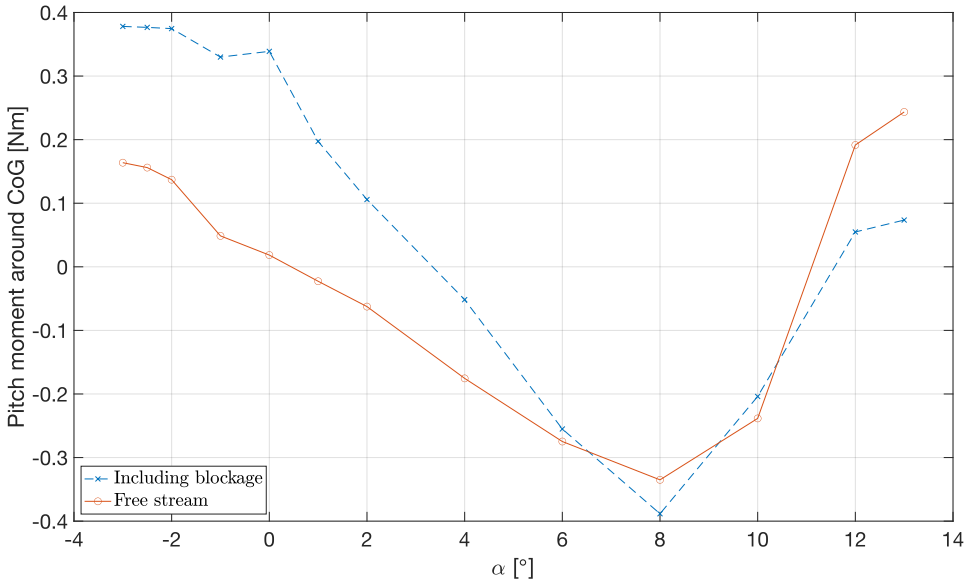

Figure 4.27: M_p variation around x=227 mm, with angle of attack at 20 m/s

Figure 4.27 shows the variation of pitch moment, around center of gravity, with angle of attack 1 at 20 m/s. The results from the numerical models are highly influenced by blockage and differ quite a lot, but both models reach their respective minimum point at the same angle of attack.

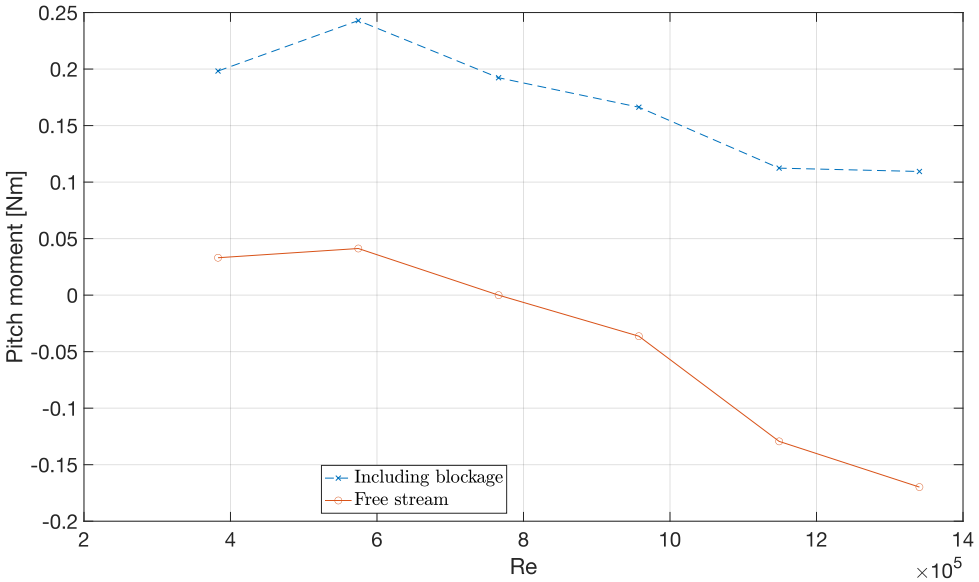

Figure 4.28: M_p variation around x=227 mm, with Reynolds number at an AoA of 1 deg

Figure 4.28 shows the variation of pitch moment, around center of gravity, with Reynolds number at an AoA of 1 deg. Results from the numerical models have a rather constant difference and move in a similar pattern.

The blockage effect of the wind tunnel walls is easily seen in CFD if Figures 4.29 and 4.30 are observed, where pressure coefficient contours are shown in the $y = 0$ m cross-section for $AoA = 1°$ and $AoA = 10°$ at $v = 20$ m/s.

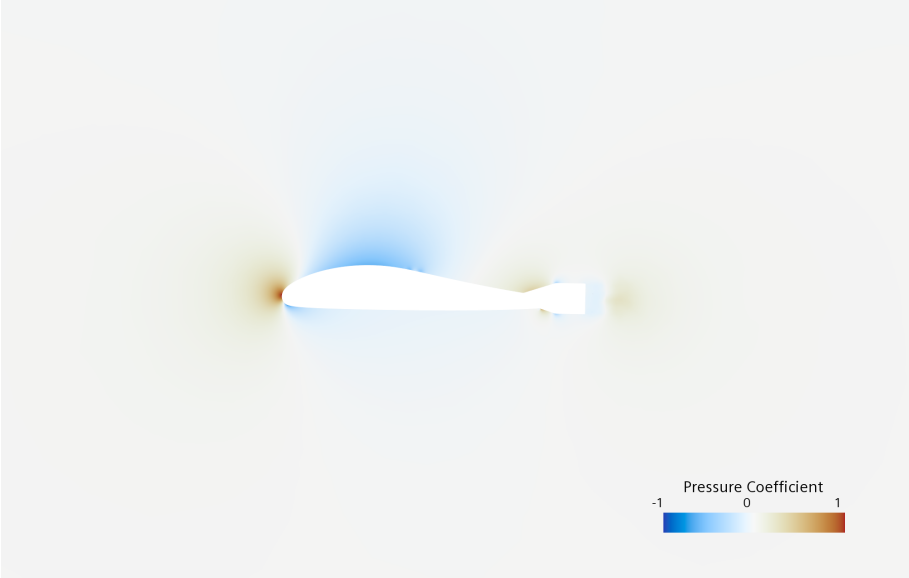

(a) Freestream domain (cropped height and length).

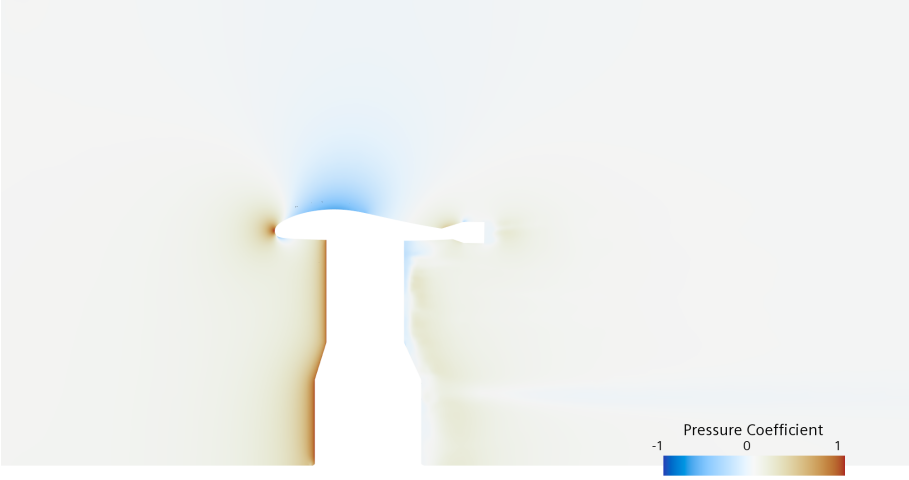

(b) Wind tunnel domain (cropped length).

Figure 4.29: Pressure coefficient contours at $y = 0$ m, $AoA = 1°$, $v = 20$ m/s

At a low AoA, the suction side interacts with the wind tunnel roof. The airfoil shaped cover for the stand is also seen interacting with the aircraft.

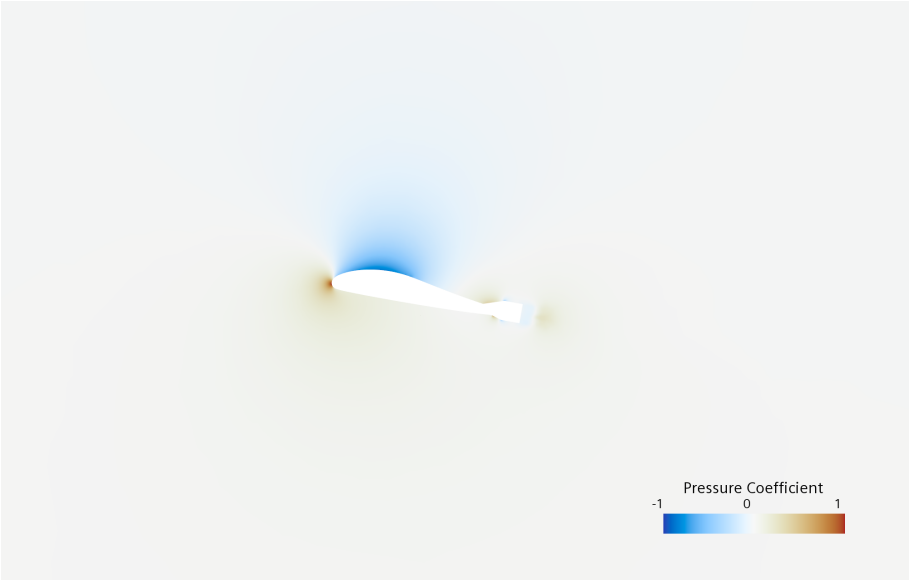

(a) Freestream domain (cropped height and length).

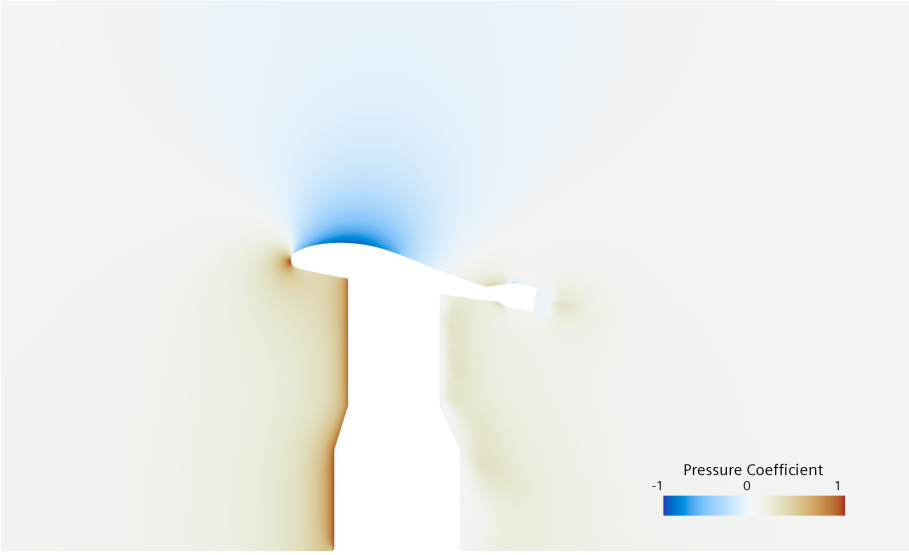

(b) Wind tunnel domain (cropped length).

Figure 4.30: Pressure coefficient contours at $y = 0$ m, $AoA = 10°$, $v = 20$ m/s

At a high AoA, the wall-interaction on the suction side is increased, as expected.

4.3 Final product

The final design iteration is closely related to the low-fidelity design presented in Section 3.2.4, but was tweaked to achieve pitch trim and to recover the lift lost in doing so.

4.3.1 Aircraft design

The overall specifications of the aircraft design is presented below in Table 4.1.

Table 4.1: Aircraft specifications for the final design.

Span	1.400 m
Body Airfoil	LA2573A
Body Mean Chord	0.510 m
Wing Airfoil	MH60
Wing Mean Chord	0.115 m
Projected Planform Area	0.320 m^2
Average Wing Sweep	32 °
Maximum twist	-6 °
Wing dihedral	5 °

The updated planform design is seen below in Figure 4.31.

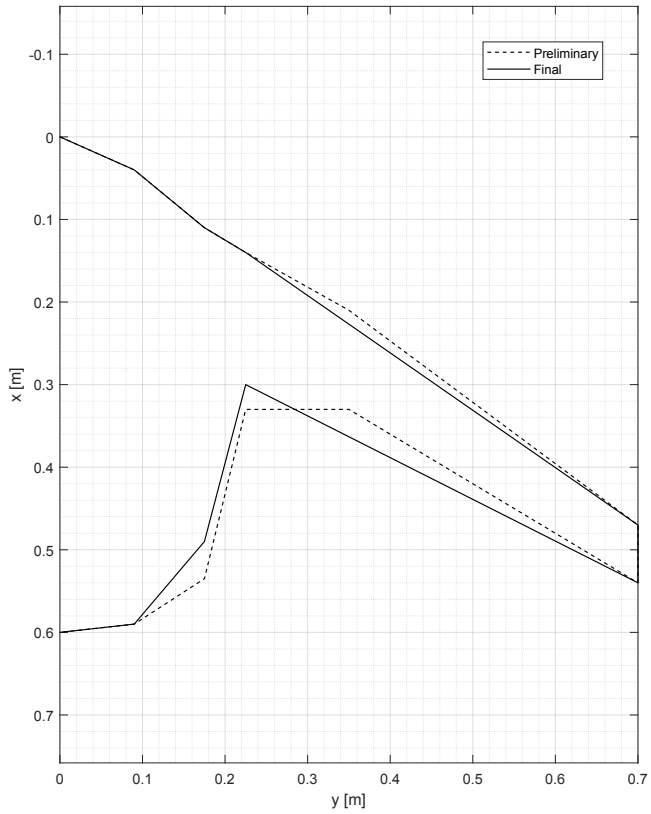

Figure 4.31: Planform of the final design together with the preliminary design from Section 3.2.4.

The body of the aircraft has stayed virtually the same in terms of airfoil, chord and span, with only a slight reduction of chord in the outboard portion. Significant

changes are seen in the wing section, where the twist was increased to move the CoP further rearwards. To compensate for the loss of lift associated with reducing the effective AoA for half of the wing (twisted portion, $y = 0.460m$ to $y = 0.700m$), the area of the wing was increased by a longer wing root chord. It was also decided cut out a larger portion of the wing for the elevon, which removed the use of the horizontal trailing edge seen in the preliminary design.

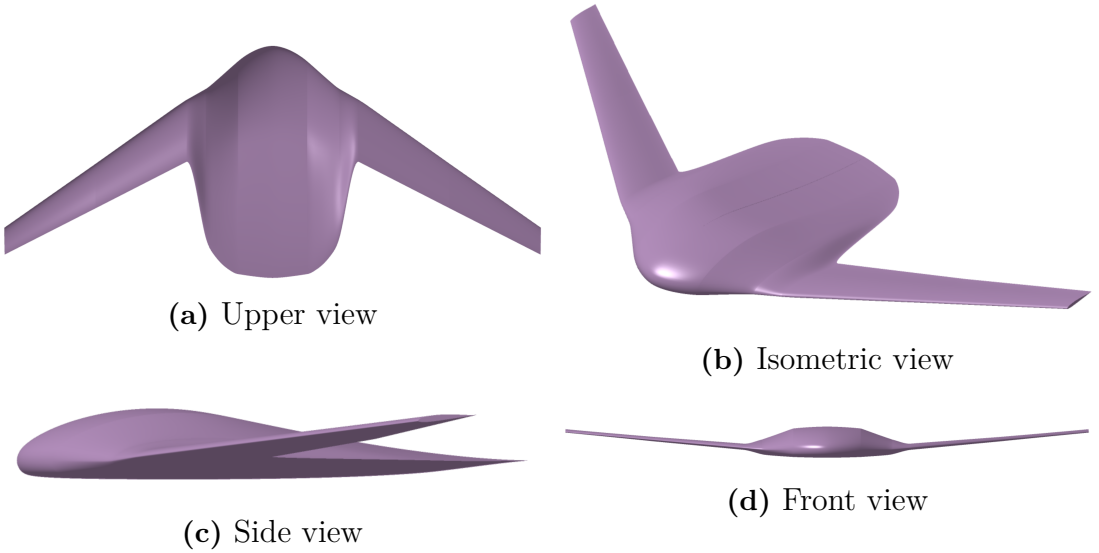

(a) Upper view

(b) Isometric view

(c) Side view

(d) Front view

Figure 4.32: Final aircraft geometry viewed in CATIA V5.

4.3.2 Structural results

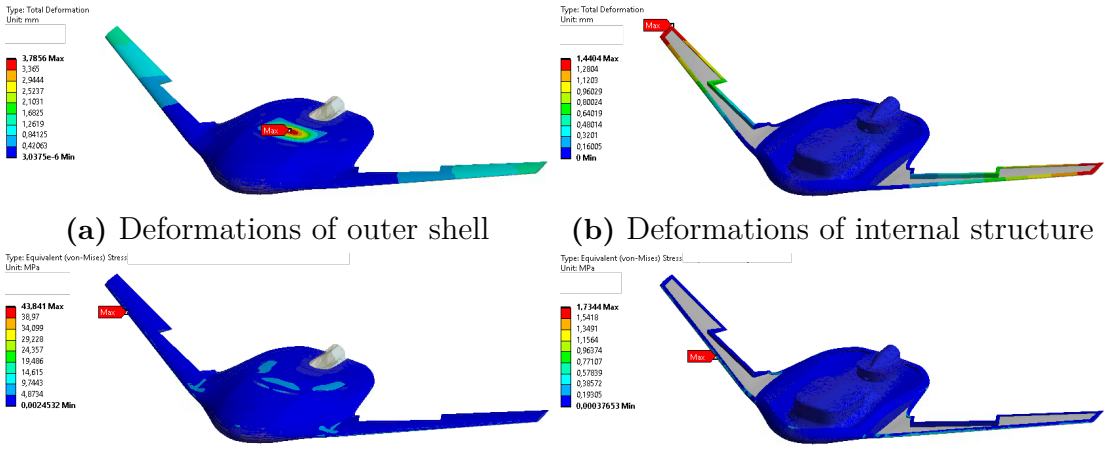

(a) Deformations of outer shell

(b) Deformations of internal structure

(c) Stress of outer shell

(d) Stress

Figure 4.33: Deformations and stresses of the structural concept

Figure 4.33 shows the FEM simulation results. The conclusion is that wingtip deflections of 1.4 mm are acceptable and the stresses predicted do not indicate any risk of failure. Figure 4.33a indicates that the suction side of the body should be

reinforced further to reduce deformations and that wings might be collapsible and hard to handle for larger unsupported areas of only two layers of CFRP.

4.3.3 Expected performance

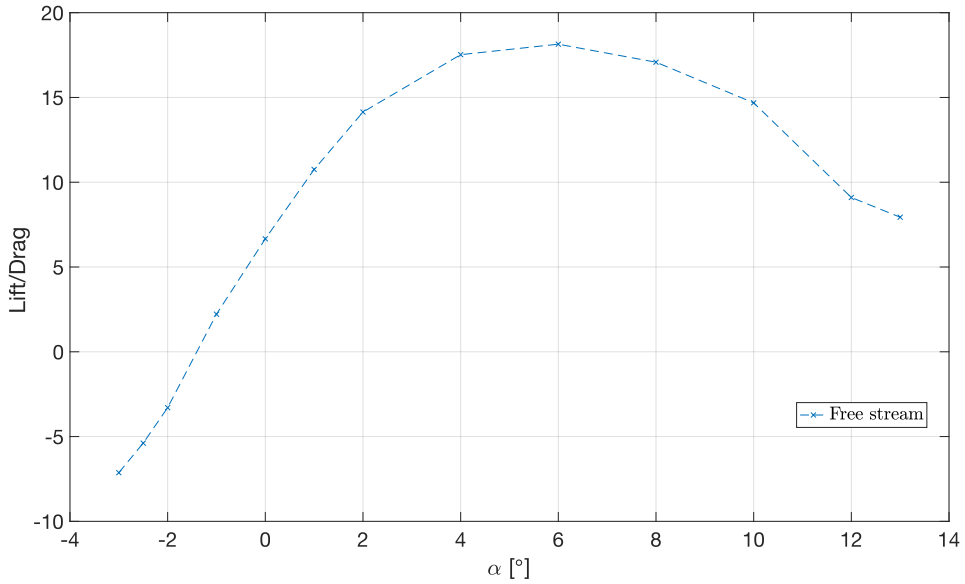

Figure 4.34: $Lift/Drag$ over angle of attack at 20 m/s

Figure 4.34 shows lift divided by drag for varying angle of attack at 20 m/s. $Lift/Drag$ peaks at an AoA of 6 deg on a value of 18.1. During sprint conditions at an AoA of 1 deg the value is 10.8 and during loiter conditions .

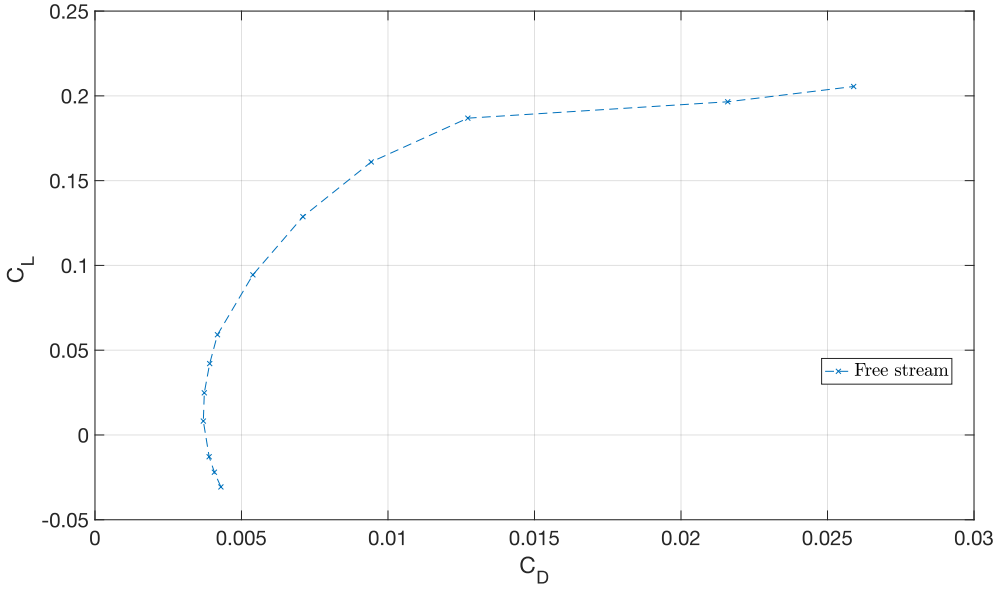

Figure 4.35: C_L over C_D at 20 m/s

Figure 4.35 shows lift over drag polar at 20 m/s.

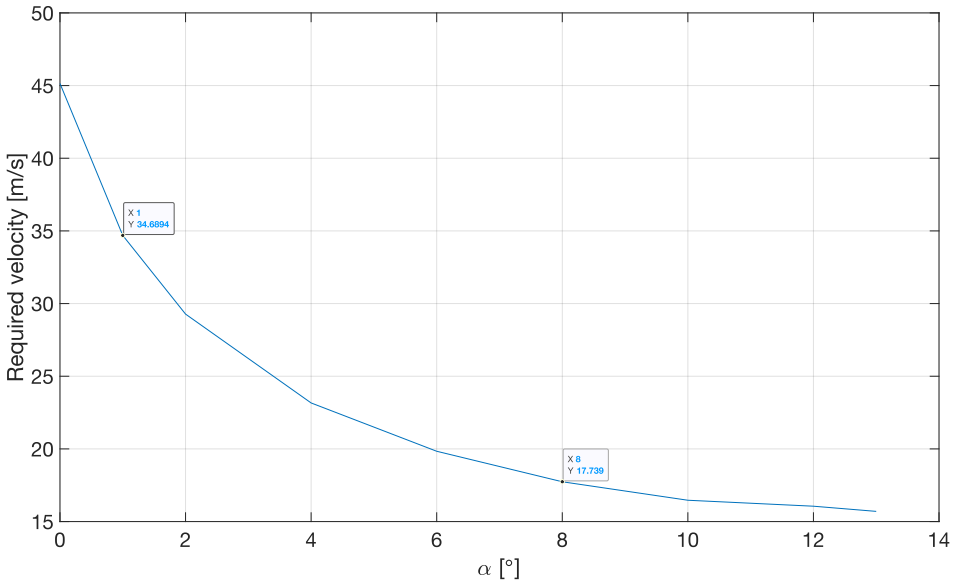

Figure 4.36: Required velocity, to sustain flight, over angle of attack

Figure 4.36 shows the required velocity to produce 30 N of lift at different angles of attack. Labeled are the sprint and loiter conditions.

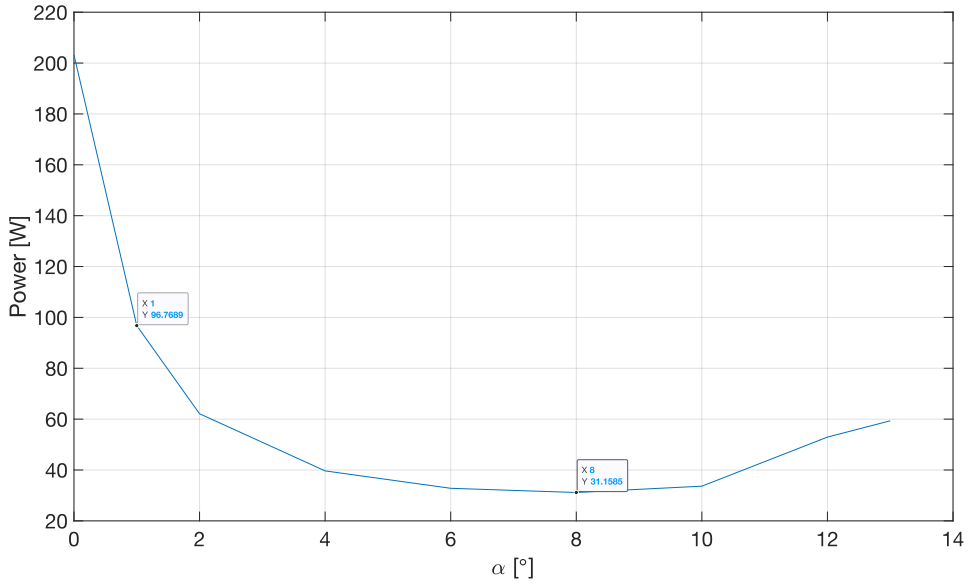

Figure 4.37: Power consumption, at sustained flight, over angle of attack

Figure 4.37 shows the consumed power at different angles of attack. It is calculated by multiplying the drag force by the required velocity from figure 4.36. Labeled are

the power consumption at sprint and loiter conditions where loiter operating angle of attack is set at the minimum power consumption.

The energy required for sprint and loiter would then be

$$96.7689 \cdot 1/3 + 31.15 \cdot 2/3 = 53Wh. \tag{4.1}$$

4.3.4 Aerodynamics

The aircraft is designed to fly in a wide range of flight conditions without the use of high-lift devices such as retractable flaps or leading edge slats. This results in a wing configuration that is a compromise between take-off and cruise. As seen in Figure 4.38, the spanwise lift distribution in cruise displays low wing loading and a significant amount of the lift generation in the aircraft body. There is a decrease in the lift slope near the mid spanwise position, which is where the linearly varying wing twist begins.

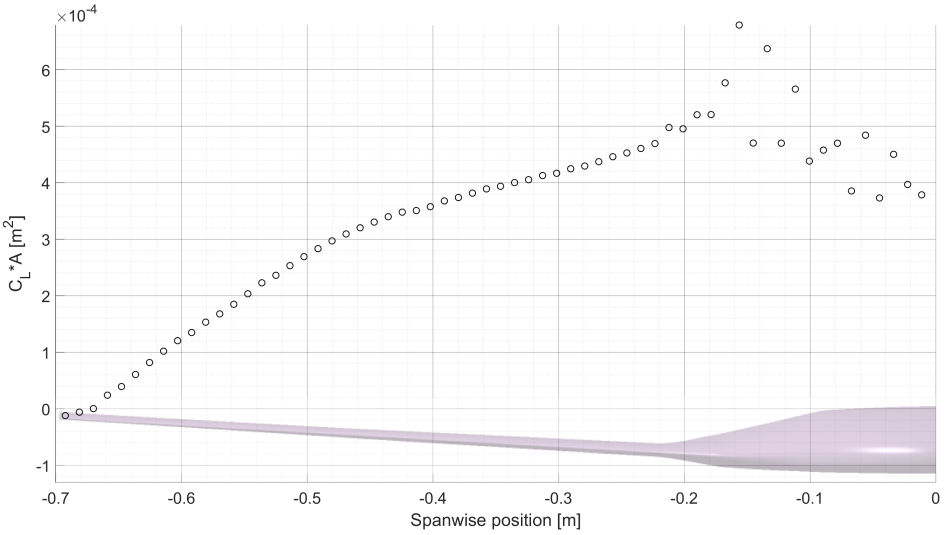

Figure 4.38: Spanwise lift distribution at cruise condition.

The body's lift is at its lowest in the middle, which possesses the largest chord, and is due to the blockage from the electrical motor assembly. In Figure 4.39 the pressure coefficient distribution at $y = 0$ m is seen (the curve with the large initial dip is the suction side). It is observed that full (or near optimal) pressure recovery is not obtained at the trailing edge, and instead a high pressure zone is present. This high static pressure propagates upstream and results in a suction peak with significantly higher static pressure.

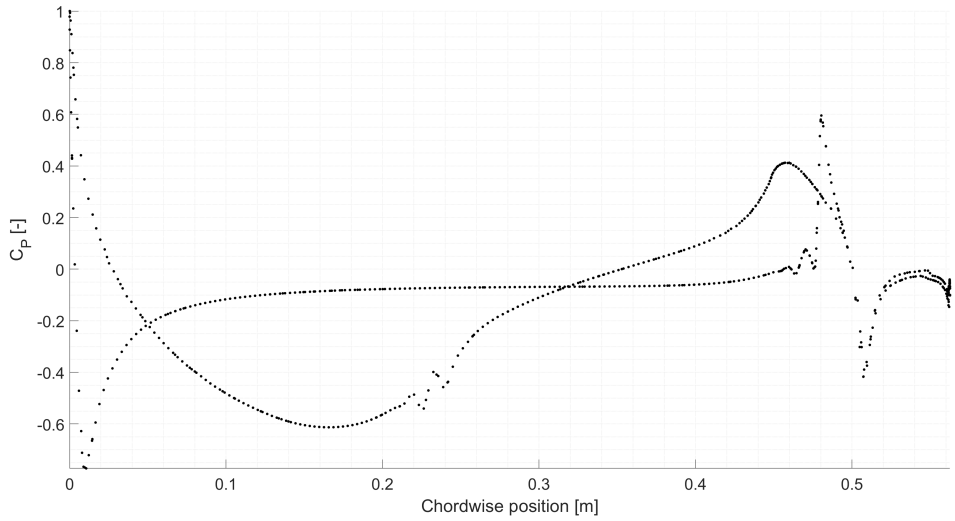

Figure 4.39: Chordwise pressure coefficient distribution at cruise condition, $y = 0$ m.

In Figure 4.40 the pressure coefficient distribution is instead viewed at a spanwise position of around $y = -0.15$ m (highest observed lift in the body from Figure 4.38), more optimal pressure recovery is seen. Notice that static pressure is recovered slightly beyond ambient ($C_P = 0$), which is due to the reflexed aft section of the body.

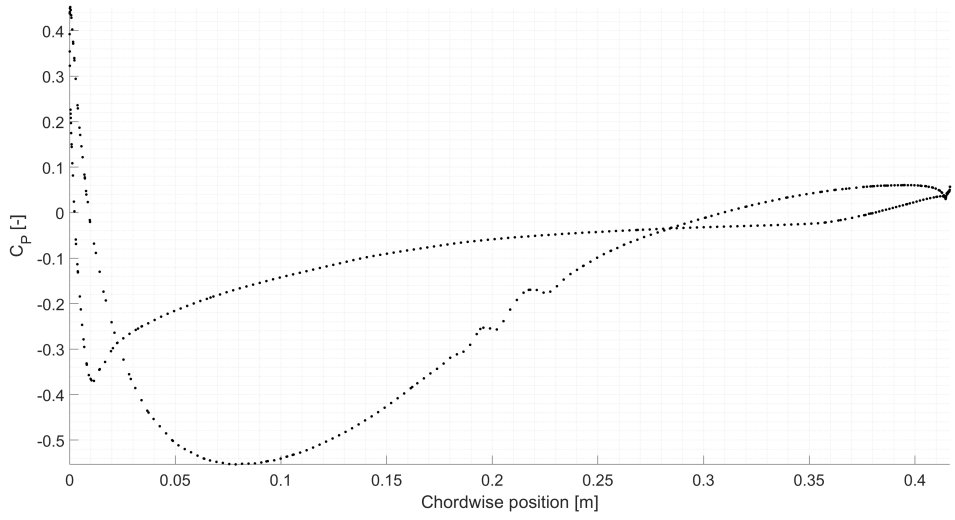

Figure 4.40: Chordwise pressure coefficient distribution at cruise condition, $y = -0.15$ m.

Figure 4.41 displays the pressure distribution at the inboard wing section $y = -0.30$ m. The discontinuity in the curve at chordwise location $x = 0.09$ m is the laminar to

turbulent transition location. This is clearly seen in Figure 4.42 where in the same chordwise location a jump in skin friction is detected (turbulent reattachment).

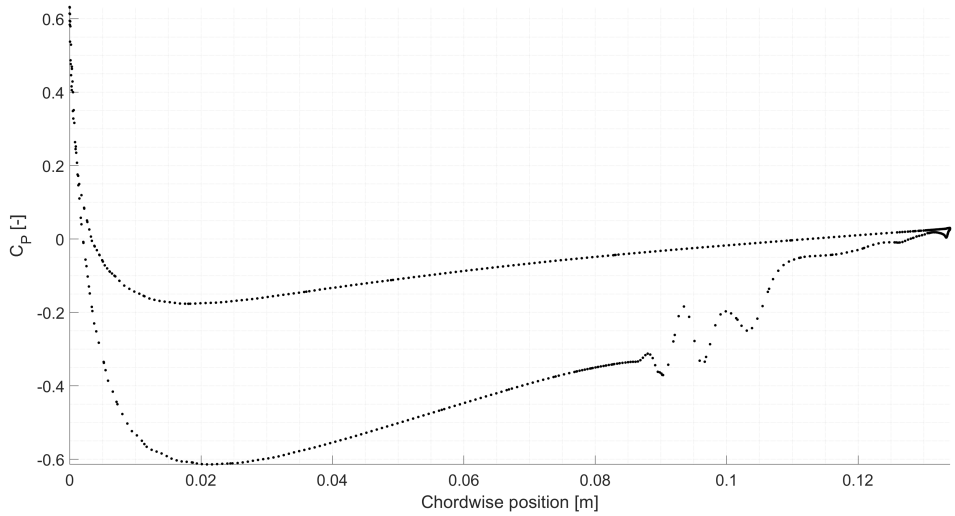

Figure 4.41: Chordwise pressure coefficient distribution at cruise condition, $y = -0.30$ m.

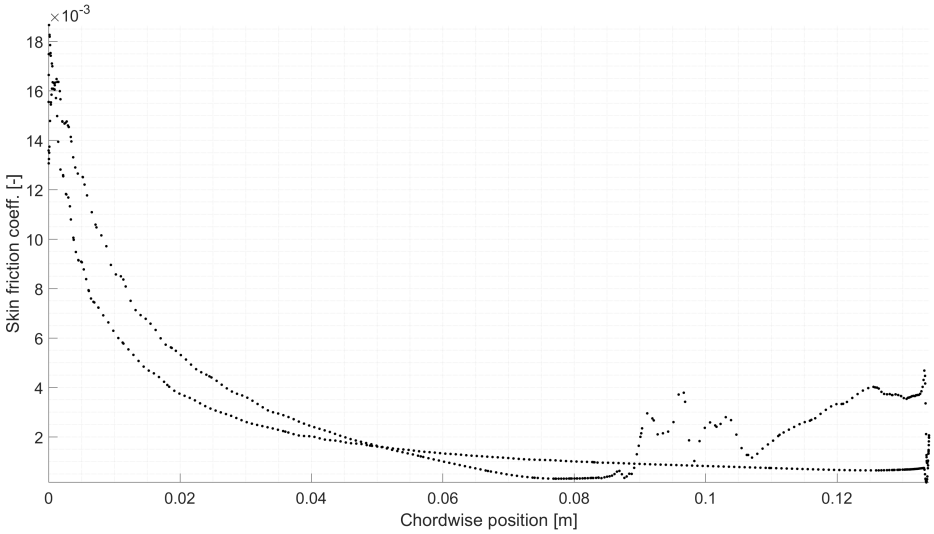

Figure 4.42: Chordwise skin friction coefficient distribution at cruise condition, $y = -0.30$ m.

To visualize the variation in pitch moment contribution across the aircraft surface, a scalar function was written to calculate the pitch moment contribution of each wall-adjacent cell, taking both lift and drag forces into account. In Figures 4.43a and 4.43b, areas marked red equal a pitch up contribution, while blue areas constitute a pitch down contribution. Pitch neutral areas are marked in white.

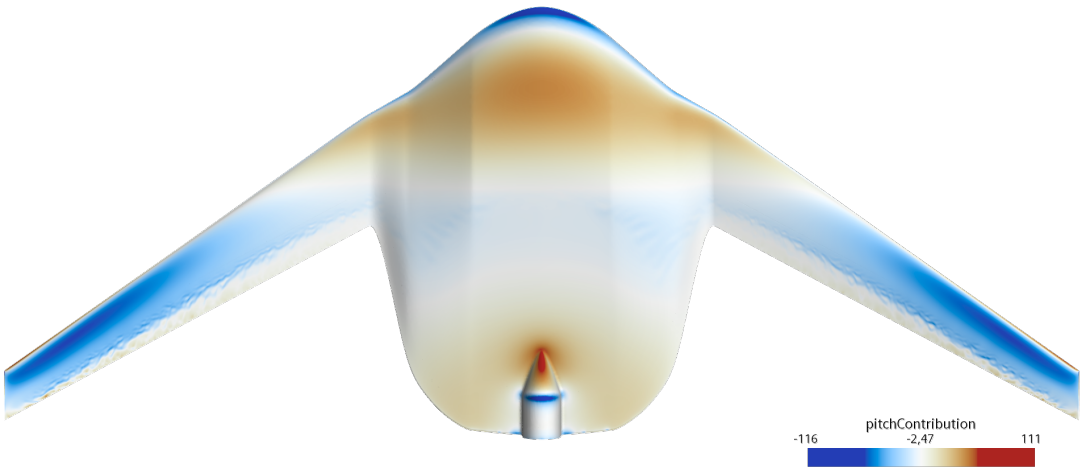

(a) Upper surface pitch moment contribution.

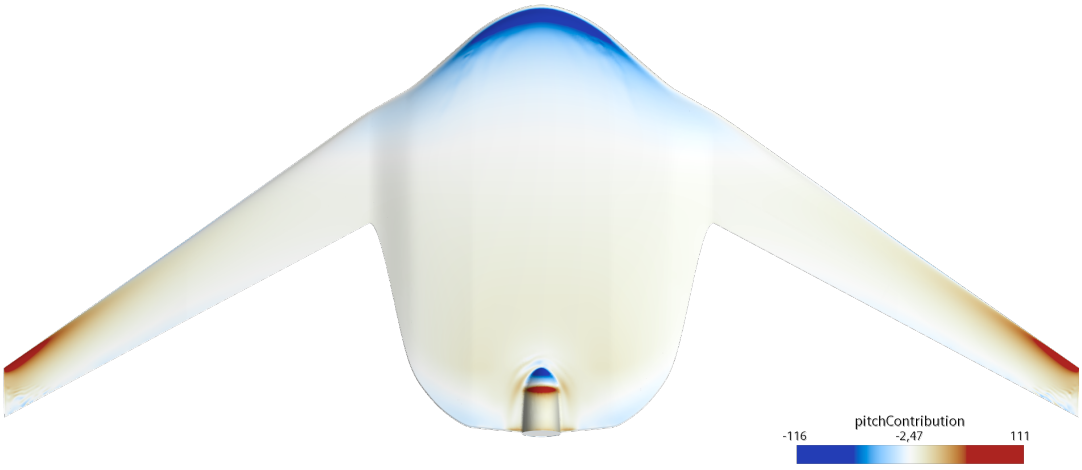

(b) Lower surface pitch moment contribution.

Figure 4.43: Contours of contribution to pitch moment at $AoA = 1°$. Areas marked red contribute to pitch up, blue to pitch down

As mentioned previously in the text, the reflexed aft section of the body helps in moving the CoP downstream (produces a pitch up moment), while the wing twist pitches the aircraft down. The aircraft is pitch neutral while in cruise condition, and it is therefore difficult to judge the pitch stability design in the figures above. If a non-trimmed condition is viewed instead, such as $AoA = 8°$ in Figures 4.44a and 4.44b, the counter pitch moment produced by the aircraft design is clearly seen.

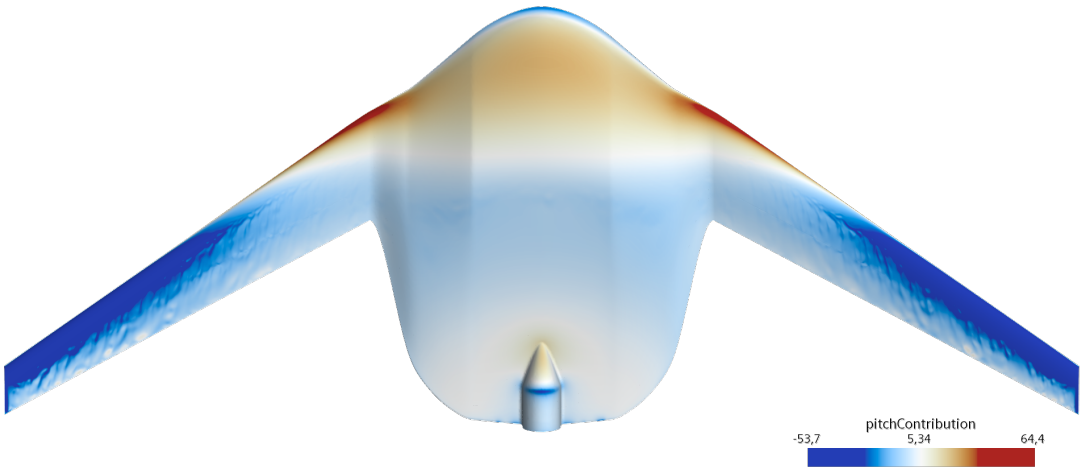

(a) Upper surface pitch moment contribution.

(b) Lower surface pitch moment contribution.

Figure 4.44: Contours of contribution to pitch moment at $AoA = 8°$. Areas marked red contribute to pitch up, and blue to pitch down.

By comparing the pitch contribution contours for the cruise condition with the higher AoA case, it is clearly seen in the latter case that the blue areas on the twisted wing portion has increased in size. This displays the aircraft's ability to naturally return to the trimmed condition when pitched up.

5

Discussion

The present chapter will discuss the method and the results and serve as a foundation for the conclusions.

5.1 Wind tunnel validation

A wind tunnel validation of the CFD model was done in order to evaluate the accuracy of virtual development methods.

5.1.1 Mounting and post processing

The test section is simplified for CFD and doesn't include neither contraction, breather slots, outlets nor re-circulation path. Most of these features have reduced impact due to over pressure in the wind tunnel compared to surroundings and lead to net flow out of the tunnel. In the end, the increased computational cost was deemed unnecessary due to low impact on results, based on recommendations.

Mounting the rig and test specimen was done as accurate as deemed necessary, roll and yaw were measured and reduced until misalignment was small and considered to have very low impact. Pitch has the biggest impact and was taken most into consideration during mounting. The pitch angle is measured on the mounted sensor and also measured on the aircraft itself, then matched towards the predicted AoA for zero-lift at 20 m/s. For the plastic aircraft this was necessary since an adaptor was glued in and the pitch angle was adjusted by 1.2 degrees to match zero-lift, this adjustment was also enforced by measurements on the aircraft after mounting that showed a misalignment on the same scale but varied depending on where it was measured. For the carbon aircraft the zero-lift match showed a zero-lift error of 0.05 degrees which showed a high accuracy in mounting.

Velocities in the wind tunnel were set to match CFD simulations, but the measured velocity was off due to the feedback loop being purposely turned off. Having it turned on results in oscillating fan power and a long time to converge to a steady state. Having it steady with a maximum difference of 0.65 m/s at 35 m/s is not an issue since most data is visualised as linearly interpolated graphs.

When necessary to compare results at the same data points, as when talking about

exact differences at specific data points, the measured data was interpolated using scatteredInterpolant in Matlab with the Natural Neighbor interpolation method [28] and linear extrapolation. The interpolated data was used to correct for mounting errors in pitch angle and differences in velocity when comparing the test results to CFD results.

The data was gathered as 7 averages over 1 second at 25 kHz with 2 seconds spacing between sampling, these 7 averages were very consistent and the end result was an average of these 7 samplings. Tests could be sped up by reducing the amounts of repeated samples at every sampling point.

5.1.2 Accuracy of virtual development methods

Lift is the primary result investigated and figures 4.21-4.22 shows a good prediction by CFD simulations for a range of angles of attack, the difference at low angles of attack could be due to small misalignment in pitch. At higher angles of attack it is clear that the plastic model loses lift compared to simulations and the carbon model, this is most likely a result of the larger wingtip deflections of the plastic model at high wing loading. At low Reynolds numbers it is clear that simulations differ from tests but likely is a combination of the low loads measured and the CFD model having a hard time to predict low velocity transition and separation. As velocity increases the values converge and the resulting $C_L \cdot A$ seems to reach a region of Reynolds independence that would be beneficial to reach earlier.

Drag was known to be a measurement with high risk of contamination due to the amount of factors that could impact the readings since they were done far from the aircraft and in a range far below the forces measured in lift. The main impact would be due to the stand and aerodynamic cover coming in contact that would result in the cover absorbing a portion of the force instead of allowing the stand to translate all of it down to the load cell mounted below the wind tunnel. Other sources of contamination could be caused by pressure differences building inside the cover due to the fact that a gap between the aircraft and cover was necessary in order for it not to absorb any load. Figures 4.23-4.24 show a good prediction on the plastic aircraft but a rather constant offset to higher values in drag for the carbon fibre aircraft, this was unexpected and could most likely be an artifact of mounting.

Pitch moment is another quantity measured by the upper load cell, the CoP_x is then calculated by dividing moment by lift. Figures 4.27-4.28 show that neither the plastic or carbon fibre models match the predicted pitch moment by CFD simulations. The pitch moment could be influenced by the mounting adjustability allowing the aircraft to slide ± 5 mm in the horizontal plane before tightening it to the load cell.

5.1.3 Flow visualization

The use of flow visualization was an inexpensive method to get a picture of the wall-shear stress and was an useful tool for qualitative comparisons between results from the high-fidelity method and reality. The transition behaviour of the boundary layer

was easily identified. A clear laminar region could be observed, that then locally separated and produced a laminar separation bubble, which finally transitioned to a turbulent flow that reattached to the surface. The result was a textbook example of how most wings behave in the Reynolds regime that the aircraft was tested in.

It was generally difficult to visualize the wall-shear stress pattern at low speeds in the Reynolds sweep. This could have been improved by running the wind tunnel for longer before taking the picture, but might not have produced a more clear result. Instead, the viscosity of the flow visualization emulsion could have been experimented more to find a emulsion that works better at lower Reynolds numbers, where the inertial forces might have been too weak to move the paint. But the results were useful in any case, and distinct regions where the air had separated were observable.

The flow visualization pictures are a good qualitative match with the skin friction coefficient contours from the wind tunnel CFD simulations. The chordwise location of the separation bubble's leading edge matches well, as does its size in the chordwise direction. The gradual decrease in wall-shear stress upstream of the separation bubble can also matches closely.

5.2 Blockage effects

The results presented in Section 4.2 exhibit a significant effect from the walls and wind tunnel stand cover on the static pressure field acting on the aircraft. Due to this, the current setup with a full-scale model is unsuitable for real-life predictions, and should therefore only be used for comparisons with CFD, where the real-life conditions are replicated.

5.3 Aircraft performance

The aircraft design fulfills the lift and stability requirements. Drag is surprisingly low, and because of this either battery capacity can be reduced to complete the set mission or the scenario time can be extended.

To increase lifting efficiency even further, a high-lift system using retractable flaps could be implemented. This would add complexity, but would essentially enable the aircraft to clear take-off conditions and be optimized for cruise.

It should also be investigated whether or not the swept-back wing with wing twist is the most efficient solution for pitch stability. The sweep decreases the lifting efficiency of the wing and either requires higher airspeed or increased wing area, with the latter being the solution for this design.

The energy consumed during sprint and loiter is lower then what was estimated and could be reduced reduced further. As estimated during the initial sizing, a high power consumption is observed at sprint which could be reduced by either

lowering the sprint velocity or downsizing the aircraft and sprinting at an AoA of higher lift/drag. Reducing the sprint velocity would have a high impact since power is proportional to velocity cubed, but this is not desired since it would oppose the main mission of reaching the accident site early. Downsizing the aircraft and sprinting at a higher angle of attack would be feasible but requires a higher launch velocity at take-off.

6

Conclusions

The task of designing and manufacturing an operational tailless BWB aircraft was considered achieved. The most difficult aspect was to achieve static stability due to the packaging requiring a center of gravity at the far front of the aircraft and the challenges that arise when having to produce moment without the increased leverage that a tail would allow for. A complete set of validated simulation models together with a modular test specimen and rig for wind tunnel tests are handed over that would allow for further development of the aircraft concept that is believed to have a potential for great success.

During test flight it was concluded that mapping complete flight characteristics is a hard task that would require a big set of simulations. Therefor flight testing and input from experienced professionals is a fast method for achieving good results that should be utilized as soon as possible once a promising design has been developed for static cases.

6.1 Future development

It is believed that future development of stability features should be pursued, either by refining the aircraft body, further evaluating the position and size of the control surfaces, adding elements such as fins or winglets, or the addition of an electric control system that ensures that the aircraft stays in a stable flight mode. Preferably a combination of multiple enhancements.

Apart from stability it is believed that projects for optimising efficiency could lead to a better performing aircraft that could reach the accident site earlier and loiter for longer.

Bibliography

[1] Leeham News. (2018), [Online]. Available: https://leehamnews.com/2018/04/03/dont-look-for-commercial-bwb-airplane-any-time-soon-says-boeings-future-airplanes-head/.

[2] NASA. (2008). "NASA Blended Wing Body – A potential new aircraft design", [Online]. Available: https://www.nasa.gov/centers/langley/news/factsheets/FS-2003-11-81-LaRC.html.

[3] Zipline. (), [Online]. Available: https://flyzipline.com/.

[4] KI. (). "Dronare levererade hjärtstartare vid misstänkta hjärtstopp i unikt pilotprojekt", [Online]. Available: https://nyheter.ki.se/dronare-levererade-hjartstartare-vid-misstankta-hjartstopp-i-unikt-pilotprojekt.

[5] Swedish Sea Rescue Society. (), [Online]. Available: https://www.sjoraddning.se/.

[6] Sjöräddningssällskapet. (2020). "Swedish Sea Rescue Society yearly meeting protocol", [Online]. Available: https://www.sjoraddning.se/sites/default/files/ssrs_arsredovisning_2021.pdf.

[7] J. D. Anderson, *Modern compressible flow: with historical perspective*. McGraw Hill Education, 2021, ISBN: 9781260570823.

[8] F. M. White, *Fluid Mechanics*. McGraw Hill, 2011, ISBN: 9780073529349.

[9] D. P. Raymer, *Aircraft Design: A Conceptual Approach (Sixth Edition)*. American Institute of Aeronautics and Astronautics (AIAA), 2018, ISBN: 9781624104909.

[10] Z. Yang, H. Igarashi, M. Martin, and H. Hu, "An Experimental Investigation on Aerodynamic Hysteresis of a Low-Reynolds Number Airfoil", *46th AIAA Aerospace Sciences Meeting and Exhibit*, Jan. 2008. DOI: 10.2514/6.2008-315.

[11] Martin Hepperle. (2018). "Laminar Separation Bubbles", [Online]. Available: https://www.mh-aerotools.de/airfoils/bubbles.htm.

[12] J. Katz, *Race Car Aerodynamics: Designing for Speed*. Robert Bentley Inc., 1995, ISBN: 9780837601427.

[13] Martin Hepperle. (2018). "Basic Design of Flying Wing Models", [Online]. Available: https://www.mh-aerotools.de/airfoils/flywing1.htm.

[14] XFLR5, *Documentation, theoretical background*, XFLR5 lecture notes. [Online]. Available: http://www.xflr5.tech/xflr5.htm.

[15] ——, *Analysis of foils and wings operating at low Reynolds numbers*, XFLR5 software documentation. [Online]. Available: http://www.xflr5.tech/xflr5.htm.

[16] Lars Davidson, *Fluid mechanics, turbulent flow and turbulence modeling*, Course material for TME226 Mechanics of Fluids and MTF271 Turbulence Modeling at Chalmers University of Technology. [Online]. Available: http://www.tfd.chalmers.se/~lada/postscript_files/solids-and-fluids_turbulent-flow_turbulence-modelling.pdf.

[17] CFD Online. (2011). "SST k-omega model", [Online]. Available: https://www.cfd-online.com/Wiki/SST_k-omega_model.

[18] Menter, F.R., Smirnov, P.E., Liu, T. et al., "A One-Equation Local Correlation-Based Transition Model", *Flow ,Turbulence and Combustion*, vol. 95, pp. 583–619, 2015. DOI: https://doi.org/10.1007/s10494-015-9622-4.

[19] Siemens, *Star-CCM+ documentation (release 16.02.008)*.

[20] airfoiltools. (). "mh60", [Online]. Available: http://airfoiltools.com/airfoil/details?airfoil=mh60-il.

[21] ——, (). "la2573a", [Online]. Available: http://airfoiltools.com/airfoil/details?airfoil=la2573a-il.

[22] P. Panagiotou, S. Fotiadis-Karras, and K. Yakinthos, "Conceptual design of a Blended Wing Body MALE UAV", *Aerospace Science and Technology*, vol. 73, pp. 32–47, 2018, ISSN: 1270-9638. DOI: https://doi.org/10.1016/j.ast.2017.11.032. [Online]. Available: https://www.sciencedirect.com/science/article/pii/S1270963817315870.

[23] Martin Hepperle. (2018). "MH60", [Online]. Available: https://www.mh-aerotools.de/airfoils/mh60koo.htm.

[24] (2022). "OpenVSP", [Online]. Available: http://openvsp.org/.

[25] F. Götten, D. Finger, M. Marino, C. Bil, M. Havermann, and C. Braun, "A review of guidelines and best practices for subsonic aerodynamic simulations using RANS CFD", Dec. 2019.

[26] Landström, C. and Löfdahl, L., *The L2 Wind Tunnel at Chalmers University of Technology*.

[27] S. Busch and I. Jonsson, "Wind Tunnel Test of a Double Blade Swept Propeller and Analysis of Real Geometry Effects", M.S. thesis, Chalmers University of Technology, Gothenburg, Sweden, Jun. 2015.

[28] MathWorks. (2022). "Interpolating Scattered Data", [Online]. Available: https://se.mathworks.com/help/matlab/math/interpolating-scattered-data.html.

DEPARTMENT OF MECHANICS and MARITIME SCIENCES
CHALMERS UNIVERSITY OF TECHNOLOGY
Gothenburg, Sweden
www.chalmers.se

CHALMERS
UNIVERSITY OF TECHNOLOGY